Photoinduced Crystallisation of CaF_2 from a $Na_2O/K_2O/CaO/CaF_2/Al_2O_3/ZnO/SiO_2$ Glass

Dissertation

(kumulativ)

zur Erlangung des akademischen Grades doctor rerum naturalium

(Dr. rer. nat.)

vorgelegt dem Rat der Chemisch-Geowissenschaftlichen Fakultät

der Friedrich-Schiller-Universität Jena

von Dipl.-Chem. Martina Stoica

geboren am 21.12.1983 in Naumburg/ Saale

Gutachter:

1. Prof. Dr. Christian Rüssel
   Otto-Schott-Institut für Materialforschung, Friedrich-Schiller-Universität Jena

2. Prof. Dr. Dörte Stachel
   Otto-Schott-Institut für Materialforschung, Friedrich-Schiller-Universität Jena

Tag der öffentlichen Verteidigung: 24.11.2017

dedicated to my beloved grandmother

Erna Emilie

Die experimentelle Arbeit für diese Promotion wurde im Zeitraum zwischen Januar 2012 und April 2017 am Otto-Schott-Institut für Materialforschung der Friedrich-Schiller-Universität Jena unter der Betreuung von Prof. Dr. rer. nat. Dr.-Ing. habil. Dr. h.c. Christian Rüssel durchgeführt.

Einverständniserklärung des Betreuers

Ich bin mit der Abfassung der Dissertation als publikationsbasiert, d.h. kumulativ, einverstanden und bestätige die vorstehenden Angaben. Eine entsprechend begründete Befürwortung mit Angabe des wissenschaftlichen Anteils des Doktoranden/der Doktorandin an den verwendeten Publikationen werde ich parallel an den Rat der Fakultät der Chemisch-Geowissenschaftlichen Fakultät richten.

Prof. Dr. Christian Rüssel		
Name des Betreuers	Ort, Datum	Unterschrift

Table of contents

List of abbreviations

Abbreviation	
EBSD	Electron backscatter diffraction analysis
EDXS	Electron dispersive X-ray spectroscopy
HAADF	High angle annular dark field
HOE	Holographic optical element
PTR	Photo-thermo-refractive
SEM	Scanning electron microscopy
SPR	Surface plasmon resonance
STEM	Scanning transmission electron microscopy
TEM	Transmission electron microscopy
VBG	Volume Bragg grating
XRD	X-ray diffraction
XRF	X-ray fluorescence

1. Motivation

Diode laser systems are indispensable in modern laser-based manufacturing. The increasing demands in our everyday life have driven the development of diode laser technology enormously in the past 20 years [1]. Already established direct applications of diode laser systems in material processing include hardening, cutting, drilling, soldering and welding of car body panels in series production.

The production of a multi kilowatt power diode laser system is realized by geometrical stacking of diode bars. The stacking of multiple emitter very close to each other generates high power and allows a compact design but is accompanied by a loss in beam quality and hence brightness in comparison to a single emitter laser diode. Improvement of the beam quality, beam density and the brightness of the laser source is possible by wavelength stabilization while placing Volume Bragg Gratings (VBGs) in the combined beam of all diodes. A part of the emitted light with exactly the desired wavelength is reflected back into the diode [2]. This is attributed to the grating structure caused by a periodic arrangement of alternating layers of high and low refractive indices. A hologram writing technique enables the production of these VBGs from photo-thermo-refractive (PTR) glass [3-5]. Irradiation with two beams of light which show interference and subsequent heat treatment causes a permanent refractive index change [6, 7]. Requirements to the material are insensitivity to radiation and temperature, variable processing of the material, adjustable spectral properties with a small angular sensitivity. The main prerequisite for VBGs in the high-power laser technology is a comparatively small absorption as well as a large change in the refractive index at the Bragg wavelength for optimum in diffraction efficiency. The material must withstand high intensities of laser radiation ($I < 2 \cdot 10^5$ W cm^{-2}). Furthermore, long-term temperature stability at $T < 100$ °C, a continuous structure without striae and inclusions inside the aperture is required for the application in high-power laser systems [8]. While Bragg gratings are easy to produce in optical fibers of simple germanium oxide-doped glasses [9], this technique cannot be applied to bulk glasses of this composition since it has too much absorption in the wavelength range of the light used for structurization. Refractive index changes in glasses based on a fluorophosphate glass system are the subject of current studies. In fluorozircoaluminate glasses, refractive index modulations are up to $\Delta n = 1.75 \cdot 10^{-4}$, but the modulation depth in the volume is limited to regions < 100 µm from the surface [10]. In borosilicate glasses, in which a silver ion exchange was previously carried out due to the recording of waveguides, VBGs were additionally recorded in the waveguides with ultra-short pulse laser radition ($\Delta n = 1 \cdot 10^{-3}$). At temperatures above 120 °C, the decomposition of the grating or waveguide has been observed [11]. The refractive index modification in high-purity, not photosensitive glasses, was demonstrated by the writing of waveguides as well as of VBGs by ultra-short pulse laser radiation using a phase mask technique [12]. The refractive index change is affected by local melting of the glass. Any change in the period of the VBG requires the production of an individual phase mask.

The economic and technological potential of diode laser systems, based on VBGs, is comparatively large. Actually, PTR glass allows the production of different types of optical elements: reflecting Bragg gratings [13, 14], transmitting Bragg gratings [15, 16], chirped Bragg gratings [17] and phase plates [18]. These elements enable a wide field of applications in laser system technology. Reflecting Bragg gratings find application as angularly and spectrally selective elements in high energy lasers to achieve spectral or coherent beam combining [19, 20], and as external couplers for longitudinal mode selection in laser systems [21]. Transmitting Bragg gratings are used for the phase locking of multimode lasers [22]. Chirped Bragg gratings are efficient optical materials for stretching and compression of ultra-short pulse lasers [23].

Therefore, the objective of this work is the development of a new type of PTR glass. Appropriate for photonic applications are transparent nano glass ceramics due to their low scattering and absorption effects [24]. The absorption can be refined using optical grade raw materials with small impurities to avoid increased absorption in the UV and IR range. Scattering effects can be avoided by a small difference in the refractive indices between the glass matrix and the crystallized phase [25]. It is also crucial that the particles are homogeneously distributed and that they have a narrow size distribution [24]. An oxyfluoride glass containing CaF_2 was chosen due to preliminary investigations which showed the ability to precipitate nanocrystals with a narrow crystallite size distribution during thermal treatment [26]. Since the refractive index differences of CaF_2 (1.43) and the glass matrix (1.52) are smaller in comparison to NaF (1.32), less undesirable scattering effects are expected. Furthermore, higher differences in the refractive indices are possible since a higher amount of CaF_2 is soluble in the glass.

Hence, the main goal of this study was to prepare a new type of PTR glass by adaption of the photo-thermal process on the $Na_2O/K_2O/CaO/CaF_2/Al_2O_3/ZnO/SiO_2$ glass system. The first aim was to find a suitable glass composition and to clarify the technological aspects of glass melting and processing. In a second step, suitable parameters for successful photoinduced crystallisation need to be found. To control the heterogeneous crystallization due to light and thermal development, the details of the proposed mechanism need to be verified also with respect to the particular production. The understanding and optimization should lead to the ability to tailor a material with respect to the required optical properties.

2. Introduction

2.1 Oxyfluoride glass ceramics

A glass is an undercooled liquid. It exists in unstable and metastable state at temperatures below and above the glass transition temperature, T_g. Under certain thermal conditions, it can transform to a stable state [27]. This means crystallization occurs and in a first step, nuclei are formed. The subsequent step is crystal growth. Both processes depend on the temperature and on the chemical composition of the glass. The nuclei are thermodynamically stable if their radius is larger than the so called critical radius. The latter decreases with decreasing temperature. The nucleation rate reaches a maximum slightly above the glass transition temperature T_g. A small number of large crystallites is obtained if the crystal growth velocity is high and the number of nuclei formed per time unit is low. By contrast, if the nucleation rate is high and the crystal growth velocity is low, numerous small crystallites are obtained [28, 29]. The nucleation rate might depend on time and at temperatures near T_g, an induction time might be observed [30, 31]. The above description is valid in the case of isochemical systems where the composition of the crystalline phase is equal to that of the glass matrix and hence the crystal growth velocity does not change with time [32, 33].

Since the 1950s, the way for the abundant use of a type of materials was opened by the findings of the high mechanical strength of these so-called glass ceramics. Stookey made this accidental discovery by overheating one of his glass samples which resulted in the formation of polycrystalline phases [34]. Glasses containing crystals with sizes less than half of the wavelength of visible light might be transparent [35]. Transparency is the most important required property of these materials especially with respect to applications in optics and photonics [24, 36]. The focus was to intensify the development of these transparent glass ceramics with crystallites in the nanometer scale since the 1980`s [37]. Furthermore, oxyfluoride glass ceramics may combine the advantages of aluminosilicate matrices and the optical features of low phonon fluoride crystals which can be activated by the incorporation of rare earth ions [38-40]. This results in materials with a narrow phonon spectrum, high luminescence quantum yield and long lifetime of the excited state, i.e. fluorescence lifetime [41]. The type of incorporation, e.g. the coordination number and the phonon energy affect the fluorescence lifetimes. If the atoms are tightly bounded in a crystalline environment, lower phonon energies are expected. Hence, the fluorescence lifetime of the excited state is increased [42]. In pure fluoride glasses with fluorine as the only anionic species, the phonon energy is low [43] but several disadvantages make them unattractive: poor mechanical and chemical stability, the high tendency towards crystallization and the high expenditure necessary to produce these materials. By contrast, the oxyfluoride glass ceramics are considerably easier to produce. Good mechanical and chemical properties are governed by the surrounding glass matrix [44]. The oxide matrix hinders nanoparticle agglomeration and protects the nanoparticles surface against inactivation, e.g. by the adsorption of water. The inertness of the glass phase results in lowered toxicity in comparison to crystalline fluorides. The incorporation of rare earth dopants primarily allocated in the crystalline phase leads to spectroscopic properties similar the properties of fluoride single crystals [39]. These materials offer a large field of possible applications [45].

2.1.1 Preparation

The glass ceramic preparation must be carried out under quite specific conditions to achieve the aimed properties in the material. In most cases, the glass phase is an aluminosilicate glass which is modified by the addition of assorted fluorides and oxides of alkali, alkali earth and/or rare earth metals, zinc, anhydrides of boric and phosphoric acids [45]. It is worth mentioning that oxyfluoride glass matrices may not only contain fluoride nanoparticles after crystallization; the formation of an oxidic crystalline phase is also possible [46, 47]. Hence, (i) the composition must be figured out in which the only crystallising phase is the desired one, (ii) the composition must be chosen within the area of glass formation in the corresponding matrix system. The suitable method to prepare transparent glass ceramics is conventional melting and subsequent thermal treatment considering the respective temperatures of nucleation and crystal growth [48, 49]. This includes the temperature range where the nucleation takes place, the temperature for maximum nucleation rate, the crystal growth velocity, its temperature dependence and the attributed activation energy. Nucleation can also be controlled by the addition of nucleating agents [50, 51] or inhibitors [52-54]. Glasses can be prepared by the sol-gel technique where a chemical solution (sol) is thermally treated and aged to produce the fine particles in a network (gel) [55]. Further heat treatment of the gel lead to the glass ceramics [56-58].

The classical crystallisation theories are restricted to isochemical systems where the chemical composition of the crystallised phase is the same as the glassy phase. The main challenge is to control the change in the chemical composition of the glass matrix and the nucleation and crystal phases due to the goal of controlling crystal size, crystal volume fraction and size distribution; the latter must always be as narrow as possible. These high standards can only be achieved in multicomponent systems, e.g. non-isochemical systems [59].

2.2 Crystallisation in non-isochemical systems - interface controlled crystallisation

The glass compositions of oxyfluoride glasses are usually quite complex. The specific number of 5-7 components corresponds to the highest possible stability of the glasses [60, 61]. The main prerequisite for glasses and glass ceramics for optical and photonic applications is the optical homogeneity. This requires isotropy of the crystalline phases in glass ceramics. This means, the formed crystallites should have lattices with higher, preferably cubic symmetry. If the crystal lattices have lower symmetry or the crystallite sizes exceed half the wavelength of the light than they loose transparency due to the anisotropy of the refractive indices as well as light scattering [62]. Hence, difluorides MF_2 with the space group Fm3m are frequently chosen for the respective crystalline phase [45]. Moreover, light scattering, in particular Rayleigh scattering needs to be avoided. Scattering occurs if the microstructure shows inhomogeneities with sizes larger than half the wavelength of the light. For this purpose, it was aimed that the size of the nanocrystals is restricted to 30 nm and the difference between the refractive indices of the crystalline and glass phase should not exceed 0.3 [63].

The formation of different crystalline phases of various compositions in the glass matrix through thermal treatment is conceivable but in most cases, a fluoride phase appears in early crystallisation stages [45]. This can be explained by a change in the composition during the crystallisation process. It is known, that an increase in the viscosity of the residual glassy matrix phase during the course of the crystallisation process is a prerequisite for the formation of nano-sized crystals. Experimental evidence was provided for many systems which are characterized by a self-organized crystallisation process, i.e. for oxides (Fe_3O_x [64-66], quartz or spodumen [67-72]) and fluorides (CaF_2 [26, 73, 74], BaF_2 [75-78], SrF_2 [79, 80], LaF_3 [81-83], $NaREF_4$ [84-86]). In these systems, the formation of a diffusion layer with increased viscosity is observed which hinders crystal growth as well as coarsening (Ostwald ripening) [77]. Two different ways can be distinguished when such a layer is formed [59]. The first one is illustrated in Figure 1. In homogeneous glasses, nucleation occurs with subsequent crystal growth if the nuclei reach the critical radius. The glass phase at the interface to the crystal is depleted in those components which form the crystal, i.e. alkali or alkaline earth fluorides and enriched in network formers, e.g. SiO_2. Hence, the viscosity around the crystals is increased. This results in a drastic and non-linear increase of diffusion coefficients near the crystal; a diffusion barrier is formed. The crystallisation process proceeds until the whole residual glassy phase has a viscosity of 10^{13} dPa. At this point the crystal growth is frozen in [87].

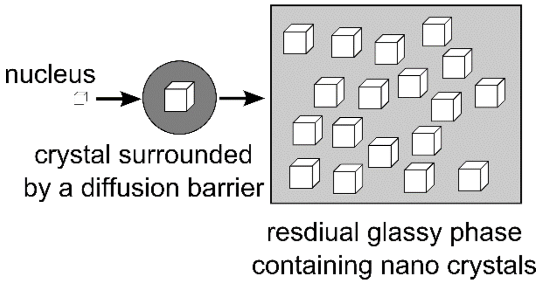

Figure 1 *Scheme from Ref. [59] of the nanocrystallisation mechanism in homogeneous glasses with homogeneous nucleation*

The second way is illustrated in Figure 2. In this case, a proceeding phase separation occurs during the nucleation and crystallisation process. A droplet phase is formed, enriched in network formers and those components that are going to crystallise [88]. This is observed in glass systems in which an Al_2O_3 and TiO_2 rich droplet phase is formed and a ZrO_2 phase is precipitated inside the droplets [67, 71, 89]. The initial phase separation also occurs in the $Na_2O/Al_2O_3/SiO_2/B_2O_3/FeO_x$ system in which multicore magnetic particles in a B_2O_3 and FeO_x rich droplet phase precipitate [65, 90, 91]. An initial droplet phase separation is observed in the $Na_2O/K_2O/Al_2O_3/SiO_2/SrF_2$ and $Na_2O/K_2O/Al_2O_3/SiO_2/LaF_3$ systems. In these systems, Al_2O_3 and SrF_2 or LaF_3 are enriched inside the droplets. The respective crystalline fluoride phases precipitate inside the droplets, while the Al_2O_3 does not form the crystalline phase and is shoved away and forms a layer around the multicore particle [81, 82, 92, 93].

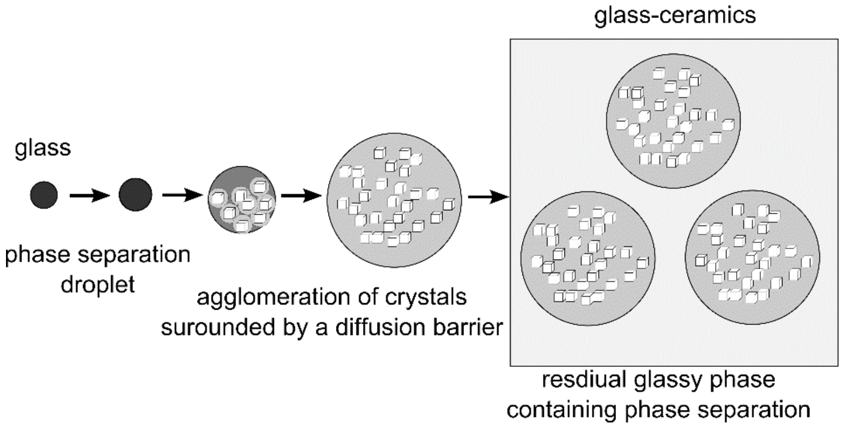

Figure 2 *Scheme from Ref. [59] of the nanocrystallisation mechanism in phase separated systems*

Since these are diffusion controlled processes, heat treatment time and temperature have a minor effect. The volume concentration of the crystalline phase increases with thermal treatment temperature and time until a constant value is approached. The mean crystallite size remains constant with a narrow crystal size distribution [26, 76, 79]. In the reversal, control of the formation of the viscous barrier allows the control of the nanometric size of the particles.

Furthermore, stresses around the crystals, the structure of the melt during cooling and the percolation model must be considered. Percolation theory describes the glass structure as a randomly formed network with rigid and floppy regions. A network becomes rigid, if the mean number of covalent bonds per network forming unit $<n>$ (SiO_2, P_2O_5, B_2O_3, Al_2O_3, TiO_2) exceeds the critical value of $n_{cr} = 2.4$; tiny non-rigid regions still remain in the network [94, 95]. The size of a floppy region can be calculated from the glass composition [96]. According to the classical nucleation theory, where nucleation occurs if the crystallisation enthalpy is equal to the surface energy of the nucleus, the size of the floppy region must be larger than the critical size of the nucleus at the respective temperature [96, 97]. In a floppy region, the diffusivity is obviously large and homogeneous nucleation takes place at $T > T_g$ [73]. The network connectivity increases during crystal growth. The excess of network modifiers which were necessary to achieve $n = 2.4$ are shoved away from the crystal into the liquid phase around the nucleus. Since an excess of network formers is present in non-isochemical systems, these will also be shoved away into the liquid phase. Hence, enrichment of network formers will increase the rigidity and the crystal growth is notably decelerated [96].

2.3 Photorefractive materials

The purposeful introduction of refractive index changes is the basis for volume phase hologram recording. Accurate recording of an optical interference pattern with high optical quality is determined first and foremost by the refractive index homogeneity within the medium. Moreover, a material that comes into consideration must be sensitive to a specific wavelength, for quite short exposure times and should remain physically and chemically stable concerning time and environment [98].

A variety of materials exist that show photosensitivity [99], i.e. photographic emulsions [100], photopolymers [101], photochromics [102-104] and photorefractives [105, 106]. The properties of these materials differ in the mechanism of image formation; a latent image after exposure requires an additional step to be developed [107, 108] or the image is developed instantaneously [109]. Further, the persistence of the image is either permanent [110] or reversible due to a decay with further exposure or thermal relaxation [111]. An example for latent image formation are silver halide photographic emulsions. These emulsions consist of a dispersion of microscopic grains of silver halide (AgBr) in a thin gelatin layer (5-15 µm) [112]. An electron from a surface localised halide ion is released by photon absorption and moves through the crystal lattice to a surface silver ion, forming silver atoms (Ag^0) with a restricted lifetime. Further absorption of photons is required to provide Ag species stable at room temperature (Ag_2^0). At least, a cluster of four atoms (Ag_4^0) is needed for a developable latent image. The photosensitivity of silver halide emulsions is high and is in agreement with the generally used laser wavelengths. The optical properties of the recording medium are not affected throughout the process, which makes it possible to use different wavelengths and record numerous holograms. The wet processing and subsequent drying is rather disadvantageous [107]. Instantaneous image development is shown by photopolymers which consist of a film-forming polymer, an initiator and one or more types of monomer. The absorption of light triggers the formation of cations or radicals from the initiator which results in a chain reaction polymerization. The refractive index modulation is increased by the diffusion of monomer into the zones of polymerization. The termination of the process hinders degradation by further exposure. The nature of the material as a film does only offer the possibility for surface hologram recording [113]. By contrast, very selective spatial and spectral gratings can be recorded in the volume of photochromic materials, which are characterised by reversible colour changes due to light exposure at the respective wavelengths but they show correspondingly low sensitivity [99].

The photorefractive effect was discovered as an undesirable optical damage [114] in $LiNbO_3$ crystals which are up to now, one of the most extensively investigated material in terms of this effect [115, 116]. Theoretically, every system which combines photoconductivity and nonlinear optical response can feature the photorefractive effect [106]. Exposure to light with a spatially periodic intensity pattern leads to the release of electrons which diffuse through the crystal lattice. Due to the photovoltaic effect, the diffusion is governed by the applied electric field and the electron charges tend to accumulate in the darker regions of the crystal. A strong electric field is created by the charge density which distorts the crystal lattice to create a periodic refractive index modulation due to the electro-optic effect [117]. The addition of Fe impurities serving as traps resulted in great improvement of the material [118]. This photorefractive effect is reversible, which means that readout leads to degradation of the image, since the same wavelength is used as for recording [119]. Controlled heating makes the refractive index modulation permanent [110]. The main drawback is the low photosensitivity of $LiNbO_3$ which requires exposure intensities about 10^4 J/ m^2 [99].

2.4 Photosensitive glass

In the second half of the last century, Corning Inc. proved to be a pioneer in the development of photosensitive glass by listing many patents issued to the company. It was first demonstrated by D. Stookey [120] that photosensitive glass based on a silicate glass has the practicability as photographic and recording medium [121]. At that time, in the 1950s, photosensitive glass was developed to record a translucent image in glass due to light scattering. First, the focus has been directed to the development of artistic coloured glass plates based on photoinduced crystallisation of Ag, Au and Cu in a two-step irradiation and heat treatment process [50]. Metal colloids and crystalline phases were obtained, which are small enough to avoid light scattering and provide a huge number of colours associated with the ions present in the glasses. The recording of the images was based on the mismatch between the refractive index of the glass matrix and the precipitated phases [122, 123]. Borate glasses and phosphate glasses were reported to be out of interest as basis for photo-thermo-refractive glass systems, as the development process was reported to start already spontaneously during the cooling phase [121], or the oxide compounds of polyvalent ions can be reduced to the metallic state and form colloids.

2.5 Photo-thermo-refractive glass

Based on the original photosensitive glass composition developed by D. Stookey in 1949 [121] a photorefractive material with outstanding prospects for the volume hologram recording is receiving increasing attention and importance for the application as holographic optical elements (HOEs) since the 1990s [5, 13, 19, 23, 124, 125]. The PTR glass is a $Na_2O/ZnO/Al_2O_3/SiO_2$ glass doped with silver, cerium, tin, antimony, fluorine and bromine [4]. It is a homogeneous, optically transparent, multicomponent glass which undergoes permanent refractive index changes after UV exposure and two-step heat treatment, making it suitable for volume phase hologram recording [3, 4]. The large permanent refractive index changes, low optical losses, good performance and high stability is the reason for the high interest in this material. The glass composition of the NaF PTR glass is listed in Table 1.

Table 1 Typical PTR glass composition from Ref. [123]

glass component	mol %	function
SiO_2	72.3	glass matrix
Na_2O	13.6	
ZnO	5.2	
Al_2O_3	2.3	
NaF	3.7	nanocrystal constituents
AlF_3	1.3	
Ag_2O	0.01	photosensitive agents, optical sensitizer
CeO_2	1.5	
KBr	0.01	
Sb_2O_3	0.03	thermal sensitizers, redox agents, refining agents
SnO_2	0.02	

The exact determination of the concentrations of the elements after melting is important for reproducible properties. A method which is used to compare relative concentrations in the PTR glass batches especially for F and Br is secondary ion mass spectroscopy (SIMS) [126, 127]. Qualitative and quantitative analyses of the polyvalent elements is performed by spectroscopic methods. Luminescence spectroscopy [128-130], UV-vis spectroscopic studies [131-133] and

EPR spectroscopy [134] were performed for the investigation of cerium, tin and antimony valence states and the influence of bromine and impurities on the optical absorption spectra [135]. Since the quality of the VBGs remains with the optical homogeneity of the glass, a new interferometry method was used by Lumeau et al. to map the optical heterogeneity over the sample [136]. Crystallisation homogeneity was studied intensively in detail by non-isothermal scanning calorimetry (DSC) and optical microscopy [137-140].

Up to now, the production of VBGs from NaF PTR glass lead to an intense increase of the performance of laser systems. VBGs in PTR glass show diffraction efficiencies up to 99.9 % and a very low shift of the Bragg wavelength by thermal variations ($dn/dT = 5 \times 10^{-8}$ 1/K). The holograms are stable under any type of radiation, since the refractive index change is due to the precipitation of the crystalline NaF phase. The silicate matrix provides superior mechanical and environmental stability and the hologram cannot be damaged by heating up to 400 °C [141].

2.6 Photoinduced crystallisation

The photo-thermal-refractive process proceeds in three steps and many studies on the function of the individual components of the PTR glass have been carried out [134, 142-147]. Nevertheless, the refractive index change mechanism in this 13-component glass (see Tab. 1) is far from being fully understood [148]. The optimisation of the photo-thermal-refractive process took several years and is still in progress. The major role in the process have the polyvalent (Ag, Ce, Sn, Sb) and highly volatile (F, Br) elements. The photoinduced crystallisation mechanism can be described as follows in a simplified way [148]:

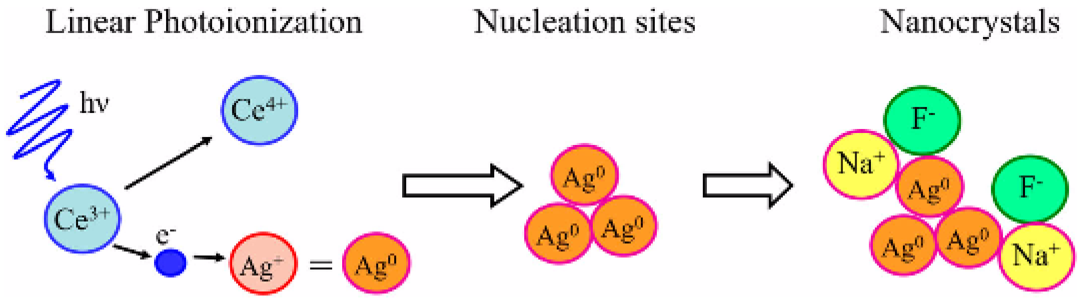

Figure 3 Schematic representation from Ref. [148] of the classical mechanism that has been extensively used to explain the photo-induced structural transformations in PTR glass.

1) UV exposure in the absorption range of Ce^{3+} causes photoionization to Ce^{4+} and an electron is released, which reduces an Ag^+ ion to a neutral Ag^0 atom.
2) The UV exposed sample is heat treated to a temperature slightly above T_g. Silver cluster, consisting of Ag^0 and possibly AgBr are formed as potential nucleation centres.

3) A subsequent heat treatment at a higher temperature leads to the crystallisation of NaF on the Ag nuclei. At least, cooling of the glass ceramic to room temperature induces local nanoscopic stresses due to the difference in the coefficients of thermal expansion (CTE) of crystals and glass matrix.

2.6.1 Photo-ionization, photo-reduction

Cerium is the most important photosensitizer due to the electron donation ability by electronic excitation from the 4f to the 5d shell. Linear photosensitivity is provided by the introduction of cerium into the PTR glass matrix, which has a band gap at 212 nm (5.8 eV). Cerium exists in the Ce^{3+} and Ce^{4+} valence states in the glass matrix, which is shown by characteristic absorption bands in the UV-vis absorption spectra [149]. The ratio of the two valencies is dependent of melting conditions, e.g. furnace atmosphere and the addition of reducing or oxidizing agents [150], the temperature of melting [151] and the concentration of polyvalent ions in the glass [152]. The absorption spectra of the 4f-5d transitions for the Ce^{3+} and charge transfer transitions (CT) for the Ce^{4+} are host sensitive and strongly depend on the type of glass [153-160]. Glass compositions with a low polarizability and comparatively low optical basicity favour the shift of redox equilibria to the reduced state [161-163]. In phosphate and borate glasses [154, 156, 164], silicate glasses and crystals [150, 160], the Ce^{3+} absorption is an envelope of five spectral components, attributed to the $^2F_{5/2} \rightarrow$ 5d transitions. The detailed analyses by absorption band separation in NaF PTR glass showed for Ce^{3+} an envelope of at least 2-3 components [132, 133]. Regular PTR glass samples were exposed with usual treatment conditions (He-Cd laser at 325 nm, 5 J cm^{-2}). It was reported that UV exposure which leads to the photoionization of Ce^{3+} did not increase the absorption of Ce^{4+} accordingly, rather a new band was induced resulting from a Ce^{3++} species [165]. The wavelength of this band remains independent from dosage and its amplitude increases with increasing dosage. Another study of cerium ionization showed the creation of additional induced absorption bands after UV exposure and the conclusion was drawn that the ionisation of cerium results in very complex redox equilibria between different species (see Eq. 1-3) [148].

$$Ce^{3+} + h\nu \rightarrow Ce^{3++} + e^{-} \qquad (Ce^{3++} \neq Ce^{4+}) \qquad (1)$$

$$Ce^{4+} + 1e^{-} \rightarrow [Ce^{4+}]e^{-} \qquad ([Ce^{4+}]e^{-} \neq Ce^{3+} \qquad (2)$$

$$[Ce^{4+}]e^{-} + h\nu \rightarrow Ce^{4+} + 1e^{-} \qquad (3)$$

It was confirmed that electrons are initially transferred to Sb^{5+} ions at room temperature (Eq. 4). The electrons are transferred to Ag ions as soon as the temperature is increased to a few hundred degrees and a latent image is created by the reduction to metallic Ag (Eq. 5) [134, 166]. Further Sn and Sb ions maintain at a constant level the redox potential of the system and create the optimum relationship between the valencies of Ag and Ce and act as regulators of the photosensitivity of the glass (Eq. 6) [142].

$$Sb^{5+} + e^{-} \rightarrow [Sb^{5+}]^{-} \tag{4}$$

$$Ag^{+} + e^{-} \rightarrow Ag^{0} \tag{5}$$

$$Sn^{2+} + Sb^{5+} \leftrightarrow Sn^{4+} + Sb^{3+} \tag{6}$$

In addition, the photosensitivity in regular PTR glass was triggered in different ways. The effect of non-linear photosensitivity was observed for a Nd:YAG laser at 355 nm when two-photon ionisation was induced [167]. Multi-photon ionisation is possible using a weakly focused femtosecond laser with a central wavelength between 800 and 1500 nm and a peak intensity of 10^{13} W cm^{-2} [168]. A shift of the photosensitivity to longer wavelengths was possible by replacing Ce by Tb ions, which is based on an upconversion-process [169].

2.6.2 Silver agglomeration

After UV exposure of the glass, the heat treatment at a temperature slightly above T_g is performed. This leads to the growth of silver particles by aggregation of silver atoms. Reasonable growth velocities are reached at a certain temperature [170]. The glass receives a characteristic yellow colouration. In the case that the Ag particles are small in comparison to the wavelength of light, the colour of the glass is determined by size, shape and volume fraction of the colloidal metal particles as well as by the dispersion properties of the glass matrix [171, 172]. A strong field is enhanced around metal particles due to collective oscillations of conduction band electrons, the so-called surface plasmons. The changes in the localised surface plasmon resonance for Ag particles are easily accessible by optical absorption spectroscopy because of their position within the range of visible light [173]. It was shown that the broad plasmon resonance absorption band is the sum of the superposition of several elementary bands [174]. In PTR glass, the formation of the nucleation centers is dependent on the dosage of UV exposure and on the heat treatment temperature. The position, intensity and the full width at half maximum (FWHM) of the plasmon resonance absorption bands are affected [175]. A linear increase of the plasmon resonance absorption band position with the irradiation dosage is observed [176-178] and furthermore, an increase of the absorption band amplitude [170, 179]. The bands are associated with the occurrence of hole centers and the formation of Ag/AgBr particles [135, 176]. The plasmon resonance maximum shifts to longer wavelengths with increasing bromide concentration. This is explained by the formation of a AgBr shell with high refractive index around the Ag particles [180]. Using simulations according to Mie theory showed that observations might be explained by the growth of a ~ 0.5 nm AgBr shell [181]. An *in situ* study of the evolution of the Ag plasmon resonance band showed that at a maximum of the amplitude evolution does not occur and the optimum of the nucleation process is associated with the appearance of a new absorption band in the visible range. This band disappears when the crystallisation starts [182]. Moreover, the maximum amplitude is reached, when the crystallisation peak temperature T_c determined by the DSC reaches its minimum. Therefore, it is expected, that the nucleation rate has its maximum [138]. The nucleation kinetics in the NaF PTR glass were fully characterised but the exact mechanism and the physical and chemical nature of the nuclei is still unclear [148].

2.6.3 Nanocrystallisation and refractive index change

The silver cluster act as nucleation center for alkaline (earth) fluoride nanocrystallisation in a second heat treatment step at a higher temperature [3, 4]. The presence of these silver particles is required for the photoinduced crystallisation step. For the NaF crystallisation in traditional PTR glass, it was shown that there is a common behaviour of the glass transition temperature T_g and the crystallisation peak temperature T_c as well as for UV exposed and unexposed PTR glass. Increased nucleation temperature or increased nucleation time does not result in a change of T_g but leads to a decreased T_c with a comparable induction period. Noticeably, the T_c for the UV exposed glass saturates at a level 50 K lower than for the unexposed glass. Hence, the photoinduced crystallisation occurs earlier and can be triggered by the choice of appropriate heat treatment conditions [138]. The growth kinetics in the unexposed PTR glass were studied in detail [183]. The steady-state nucleation rates, nucleation time-lags and crystal growth velocities are analysed on the basis of classical nucleation theory. It is assumed that the NaF solubility determines the saturation level and hence, the thermodynamic driving force for the crystallisation [137]. The NaF solubility is described as a correlation between the equilibrium volume fraction of crystallized NaF and temperature. The crystallisation stops when the crystallised volume is in equilibrium with the dissolved NaF in the residual glass matrix. The equilibrium volume fraction decreases with increasing temperature. Therefore, the thermodynamic driving force is an interaction between the temperature and the evolution of the crystallisation process. Moreover, NaF crystallisation undergoes simultaneously a liquid-liquid phase separation (LLPS) [184] which is influenced by the bromide concentration. It is proposed that the number of free F^- ions is related to the bromide concentration and that the NaF solubility is decreased. Thus, the maximum volume fraction of crystallised NaF increases with increasing bromide concentration. The correlation between T_g and heat treatment time showed a drop of T_g followed by an increase of T_g, which then saturates at a value close to the heat treatment temperature, which is proposed to be an evidence for crystallisation in the glass matrix and not in the droplets because the formation of crystals depletes the glass matrix in Na and F [148]. The observed drop of Tg in the T_g vs. time plot for short heat treatment times decreases by the addition of bromide, probably by changing the solubility of NaF in the glass and hence, the thermodynamic driving force for the crystallisation [139]. NaF nucleation occurs between 430 and 560 °C and the maximum nucleation rate is achieved at approximately 485 °C, which also provides the lowest level of scattering in holographic optical elements recorded in PTR glass [174]. XRD studies showed that crystals do not exceed diameters of 20 nm with increasing heat treatment time but the number of crystals is increasing. The restricted crystal size is proposed to be due to the limited amount of fluorine in the glass [185]. Electron micrographs of hyper-developed samples show different morphologies for unexposed and UV exposed samples [140]. The precipitation of the nanocrystals correlates with the refractive index change in the pre-irradiated regions of the glass but is not strictly proportional to the volume fraction of NaF crystals [185]. Moreover, the refractive index change depends on the thermal treatment and cooling process [186]. Different possible mechanisms are described for the overall negative refractive index change [187, 188]. A small change of the refractive index also occurs in the non-irradiated regions [146]. Solely the refractive index difference Δn (Eq. 7) is of interest since this is a characteristic parameter for the efficiency of a VBG.

$$\Delta n = n^{\text{UV-exposed and thermally treated}} - n^{\text{unexposed}} \qquad (7)$$

It is proposed that the origin of the refractive index change between UV exposed and unexposed areas in the glass are nanoscale stresses which are caused by differences in the CTE between the PTR glass matrix and the cubic NaF crystals [187].

3. Articles

Erklärung zu den Eigenanteilen

Für alle in dieser kumulativen Dissertation verwendeten Manuskripte liegen die notwendigen Genehmigungen der Verlage („Reprint permissions“) für die Zweitpublikation vor.

Für alle in dieser kumulativen Dissertation verwendeten Manuskripte sind sowohl über die Nutzung, als auch über die oben angegebenen Eigenanteile der weiteren Doktoranden/Doktorandinnen als Koautoren an den Publikationen und Zweitpublikationsrechten bei einer kumulativen Dissertation informiert und stimmen dem zu.

Name des Promovenden/der Promovendin	Ort, Datum	Unterschrift

Article 3.1

M. Stoica, G.N.B.M. de Macedo, C. Rüssel

Photo induced crystallization of CaF_2 from a $Na_2O/K_2O/CaO/CaF_2/Al_2O_3/SiO_2$ glass

Optical Materials Express **2014** 4(8):1574-1585

DOI: http://dx.doi.org/10.1364/OME.4.001574

Photo induced crystallization of CaF_2 from a $Na_2O/K_2O/CaO/CaF_2/Al_2O_3/SiO_2$ glass			
Beteiligt an			
	Martina Stoica	Guilherme Nunes Braga Mauricio de Macedo	Prof. Christian Rüssel
Konzeption des Forschungsansatzes	X		X
Planung der Untersuchung	X		
Datenerhebung	X	X	
Datenanalyse und Interpretation	X		
Schreiben des Manuskripts	X		X
Vorschlag Anrechnung Publikationsäquivalente	1,0		

Photo induced crystallization of CaF_2 from a $Na_2O/K_2O/CaO/CaF_2/Al_2O_3/SiO_2$ glass

Martina Stoica, Guilherme Nunes Braga Maurício de Macedo and Christian Rüssel,*

Otto-Schott-Institut, Jena University, Fraunhoferstr. 6, 07743 Jena, Germany
*ccr@uni-jena.de

Abstract: A new photo thermal refractive glass system is introduced. Glasses in the system $Na_2O/K_2O/CaO/CaF_2/Al_2O_3/SiO_2$ were doped with Ag_2O, CeO_2, KBr, SnO_2 and Sb_2O_3. They were irradiated with UV light and subsequently thermally annealed at 530 °C, a temperature just above Tg. This led to a slightly yellow coloration. A second thermal annealing step at a temperature of 560 °C led to the crystallization of cubic CaF_2 as proved by x-ray diffraction. Samples, annealed in a two step process at 530 °C for 1 h and 560 °C for 20 h without previous irradiation did not show crystallization. Furthermore, the effect of irradiation time on crystallization behavior and the role of KBr in the photoinduced crystallization process were also investigated.

OCIS codes: (160.0160) Materials; (160.2750) Glass and other amorphous materials; (160.5320) Photorefractive materials; (160.5335) Photosensitive materials

References and links

1. L. B. Glebov, "Kinetics modeling in photosensitive glass," Opt. Mater. **25**(4), 413–418 (2004).
2. V. A. Borgman, L. B. Glebov, N. V. Nikonorov, G. T. Petrovskii, V. V. Savvin, and A. D. Tsvetkov, "Photothermorefractive effect in silicate-glasses," Dokl. Akad. Nauk SSSR **309**, 336–339 (1989).
3. L. B. Glebov, "Photosensitive holographic glass - new approach to creation of high power lasers," Phys. Chem. Glasses-B **48**, 123–128 (2007).
4. S. D. Stookey, "Photosensitive Glass - a new photographic medium," Ind. Eng. Chem. **41**(4), 856–861 (1949).
5. J. Lumeau, L. Glebova, and L. B. Glebov, "Influence of UV-exposure on the crystallization and optical properties of photo-thermo-refractive glass," J. Non-Cryst. Solids **354**(2-9), 425–430 (2008).
6. L. B. Glebov, N. V. Nikonorov, E. I. Panysheva, G. T. Petrovsky, V. V. Savvin, I. V. Tunimanova, and V. A. Tsekhomsky, "New potentialities of photosensitive glasses for volume phase hologram recording," Opt. Spektrosk. **73**, 404–412 (1992).
7. L. B. Glebov, N. V. Nikonov, G. T. Petrovsky, and M. V. Kharchenko, "Formation of optical-elements by the photothermoinduced crystallization of glasses," Izv. an Sssr. Fiz. **56**, 133–140 (1992).
8. M. Mortier, "Between glass and crystal: glass-ceramics, a new way for optical materials," Philos. Mag. B **82**, 745–753 (2002).
9. K. F. Kelton, "Kinetic model for nucleation in partitioning systems," J. Non-Cryst. Solids **274**(1-3), 147–154 (2000).
10. C. Bocker, C. Rüssel, and I. Avramov, "Transparent nano crystalline glass-ceramics by interface controlled crystallization," Int. J. Appl. Glass Sci. **4**(3), 174–181 (2013).
11. G. P. Souza, V. M. Fokin, E. D. Zanotto, J. Lumeau, L. Glebova, and L. B. Glebov, "Micro and nanostructures in partially crystallised photothermorefractive glass," Phys. Chem. Glasses-B **50**, 311–320 (2009).
12. L. Glebova, J. Lumeau, M. Klimov, E. D. Zanotto, and L. B. Glebov, "Role of bromine on the thermal and optical properties of photo-thermo-refractive glass," J. Non-Cryst. Solids **354**(2-9), 456–461 (2008).
13. L. Glebova, D. Ehrt, and L. Glebov, "Luminescence of dopants in PTR glass," Phys. Chem. Glasses-B **48**, 328–331 (2007).
14. J. Lumeau, A. Sinitskii, L. Glebova, L. B. Glebov, and E. D. Zanotto, "Spontaneous and photo-induced crystallisation of photo-thermo-refractive glass," Phys. Chem. Glasses-B **48**, 281–284 (2007).
15. J. Lumeau, L. Glebova, G. P. Souza, E. D. Zanotto, and L. B. Glebov, "Effect of cooling on the optical properties and crystallization of UV-exposed photo-thermo-refractive glass," J. Non-Cryst. Solids **354**(42-44), 4730–4736 (2008).
16. J. Lumeau and L. B. Glebov, "Modeling of the induced refractive index kinetics in photo-thermo-refractive glass," Opt. Mater. Express **3**(1), 95–104 (2013).
17. J. Fu, J. M. Parker, P. S. Flower, and R. M. Brown, "Eu^{2+} ions and CaF_2-containing transparent glass-ceramics," Mater. Res. Bull. **37**(11), 1843–1849 (2002).

18. S. Tanabe, H. Hayashi, T. Hanada, and N. Onodera, "Fluorescence properties of Er^{3+} ions in glass ceramics containing LaF_3 nanocrystals," Opt. Mater. **19**(3), 343–349 (2002).
19. X. Y. Sun, M. Gu, S. M. Huang, X. J. Jin, X. L. Liu, B. Liu, and C. Ni, "Luminescence behavior of Tb^{3+} ions in transparent glass and glass-ceramics containing CaF_2 nanocrystals," J. Lumin. **129**(8), 773–777 (2009).
20. M. J. Dejneka, "The luminescence and structure of novel transparent oxyfluoride glass-ceramics," J. Non-Cryst. Solids **239**(1-3), 149–155 (1998).
21. Y. H. Wang and J. Ohwaki, "New Transparent Vitroceramics Codoped with Er^{3+} and Yb^{3+} for Efficient Frequency up-Conversion," Appl. Phys. Lett. **63**(24), 3268–3270 (1993).
22. J. S. Kim, M. Müller, and W. Seeber, "Mixed oxide and fluoride glasses containing optically active nanocrystals," Glass Sci. Technol. **75**, 330–333 (2002).
23. C. Rüssel, "Nanocrystallization of CaF_2 from $Na_2O/K_2O/CaO/CaF_2/Al_2O_3/SiO_2$ glasses," Chem. Mater. **17**(23), 5843–5847 (2005).
24. R. P. F. de Almeida, C. Bocker, and C. Rüssel, "Size of CaF_2 crystals precipitated from glasses in the $Na_2O/K_2O/CaO/CaF_2/Al_2O_3/SiO_2$ system and percolation theory," Chem. Mater. **20**(18), 5916–5921 (2008).
25. C. Bocker, J. Wiemert, and C. Rüssel, "The formation of strontium fluoride nano crystals from a phase separated silicate glass," J. Eur. Ceram. Soc. **33**(10), 1737–1745 (2013).
26. C. Bocker and C. Rüssel, "Self-organized nano-crystallisation of BaF_2 from $Na_2O/K_2O/BaF_2/Al_2O_3/SiO_2$ glasses," J. Eur. Ceram. Soc. **29**(7), 1221–1225 (2009).
27. D. Tauch and C. Rüssel, "Glass-ceramics with zero thermal expansion in the system $BaO/Al_2O_3/B_2O_3$," J. Non-Cryst. Solids **351**(27-29), 2294–2298 (2005).
28. S. Bhattacharyya, C. Bocker, T. Heil, J. R. Jinschek, T. Höche, C. Rüssel, and H. Kohl, "Experimental evidence of self-limited growth of nanocrystals in glass," Nano Lett. **9**(6), 2493–2496 (2009).
29. C. Bocker, I. Avramov, and C. Rüssel, "Viscosity and diffusion of barium and fluoride in $Na_2O/K_2O/Al_2O_3/SiO_2/BaF_2$ glasses," Chem. Phys. **369**(2-3), 96–100 (2010).
30. K. Ritter, S. Gerlach, and C. Rüssel, "Photo induced surface near crystallization of a glass in the system $Na_2O/K_2O/CaO/CaF_2/Al_2O_3/SiO_2$," J. Non-Cryst. Solids **356**(52-54), 3090–3094 (2010).
31. H. Ebendorff-Heidepriem and D. Ehrt, "Formation and UV absorption of cerium, europium and terbium ions in different valencies in glasses," Opt. Mater. **15**(1), 7–25 (2000).
32. A. M. Efimov, A. I. Ignat'ev, N. V. Nikonorov, and E. S. Postnikov, "Spectral components that form UV absorption spectrum of Ce^{3+} and Ce^{4+} valence states in matrix of photothermorefractive glasses," Opt. Spectrosc. **111**(3), 426–433 (2011).
33. A. M. Efimov, A. I. Ignatiev, N. V. Nikonorov, and E. S. Postnikov, "Quantitative UV-VIS spectroscopic studies of photo-thermo-refractive glasses. I. Intrinsic, bromine-related, and impurity-related UV absorption in photo-thermo-refractive glass matrices," J. Non-Cryst. Solids **357**(19-20), 3500–3512 (2011).
34. N. V. Nikonorov, A. A. Savin, and V. A. Tsekhomskii, "Influence of ionizing radiation on the spectral properties of photo-thermo-refractive glass containing silver nanoparticles," Glass Phys. Chem. **39**(3), 261–265 (2013).
35. W. Preidel and J. Nolting, "Kinetics of demixing of silver bromide - sodium bromide mixed-crystals. 1. electrical-conductivity measurements," Z Phys Chem Neue Fol **108**, 1–9 (1977).
36. G. P. Souza, V. M. Fokin, C. A. Baptista, E. D. Zanotto, J. Lumeau, L. Glebova, and L. B. Glebov, "Effect of Bromine on NaF Crystallization in Photo-Thermo-Refractive Glass," J. Am. Ceram. Soc. **94**(9), 2906–2911 (2011).
37. S. Bhattacharyya, T. Höche, K. Hahn, and P. A. van Aken, "Various transmission electron microscopic techniques to characterize phase separation - illustrated using a LaF_3 containing aluminosilicate glass," J. Non-Cryst. Solids **355**(6), 393–396 (2009).
38. A. Hoell, Z. Varga, V. S. Raghuwanshi, M. Krumrey, C. Bocker, and C. Rüssel, "ASAXS study of CaF_2 nanoparticles embedded in a silicate glass matrix," J. Appl. Cryst. **47**(1), 60–66 (2014).
39. V. S. Raghuwanshi, A. Hoell, C. Bocker, and C. Rüssel, "Experimental evidence of a diffusion barrier around BaF_2 nanocrystals in a silicate glass system by ASAXS," CrystEngComm **14**(16), 5215–5223 (2012).
40. N. Tsakiris, P. Argyrakis, I. Avramov, C. Bocker, and C. Rüssel, "Crystal growth model with stress development and relaxation," Epl-Europhys. Lett. **89**(1), 18004 (2010).
41. C. Bocker, I. Avramov, and C. Rüssel, "The effect of stresses during crystallization on the crystallite size distributions," J. Eur. Ceram. Soc. **31**(15), 2861–2866 (2011).
42. J. Lumeau, L. Glebova, V. Golubkov, E. D. Zanotto, and L. B. Glebov, "Origin of crystallization-induced refractive index changes in photo-thermo-refractive glass," Opt. Mater. **32**(1), 139–146 (2009).

---

1. Introduction

Glasses which can be structured by light and subsequent thermal annealing are denoted as photo thermo refractive glasses (PTR) [1–4]. They are first irradiated by UV light and subsequently thermally treated at one or two temperatures above the glass transition temperature, T_g. This results in the formation of tiny crystals in those parts of the glass which have been irradiated. In the irradiated region of the glass, the refractive index changes during thermal treatment, while in the not irradiated regions, which do not contain crystals, the refractive index remains approximately the same as before irradiation and subsequent annealing [1–3, 5]. Thus, the refractive index of these glasses can locally be altered and hence a structurization using light of appropriate wavelengths is possible [6, 7]. For photonic applications it is essential to avoid light scattering. Therefore the formed crystals should be smaller than one-half of the wavelength λ of the light which is used [8]. It should also be taken into account, that the formed crystals do not possess a unique size, but exhibit a certain size distribution. Using chemical systems which show an interface controlled nucleation, enables to produce fairly narrow crystal size distributions. In these compositions, the growing crystals form a shell around themselves which acts as a diffusion barrier that hinders further crystal growth, leading to crystallite sizes in the range of a few nm [9, 10]. Nevertheless, the crystal sizes should preferably be smaller than $\lambda/4$. If the particles are not homogeneously distributed, e.g. agglomerated, scattering may occur at far smaller particle sizes. In the literature predominantly, one system is described which shows a photo thermo refractive effect in the volume [11]. It is a silicate glass which contains Ce_2O_3 and Sb_2O_3, fluoride and trace quantities of silver halides. According to the literature, during irradiation of this glass, Ce^{3+} is oxidized ($Ce^{3+} + h\upsilon \rightarrow Ce^{4+} + e^-$) and the electron formed is trapped by a silver ion which is transformed to a silver atom ($Ag^+ + e^- \rightarrow Ag^0$). In a subsequent annealing step at a temperature slightly above T_g, clustering of silver atoms occurs. These clusters act as nuclei during the second annealing step and lead to the crystallization of NaF [5, 12–15].

In order to design a new PTR-glass, numerous crystalline phases which might be precipitated were taken into account. The main prerequisite is that the crystals do not grow to a size which leads to light scattering. Changes in the refractive index should run parallel to any crystallization process [16]. In the past few years, some oxyfluoride glass-ceramics have been described in the literature, which are optically transparent and nevertheless contain notable quantities of halide crystals [17–22], much more than usually present in PTR glasses. From these oxyfluoride glass systems, the crystallization of CaF_2 [17, 19, 23, 24], SrF_2 [10, 25], BaF_2 [26, 27] and LaF_3 [18, 20] as well as that of NaF [12, 13] has been reported. During crystal growth the glass near the crystal is depleted in those components which form the crystal [10, 23, 24, 26, 28]. This means for example, the melt near the crystal is depleted in fluoride and e. g. in Ba^{2+} [26] or Ca^{2+} [23] and hence also enriched in the other components of the glass. This results in the formation of a diffusion profile around the crystal and more important also in a decrease of the diffusion coefficient over several orders of magnitude [29]. These diffusion layers around the growing crystals hinder further crystal growth and lead to crystallite sizes in the range of a few nm.

Crystalline CaF_2 has already been reported to precipitate by simple thermal treatment from melts in the system $Na_2O/K_2O/CaO/CaF_2/Al_2O_3/SiO_2$ [23, 24]. In this case, a wide variation of the annealing temperatures and annealing times did not result in notably different crystallite sizes. It should further be noted that the refractive index of CaF_2 crystals is 1.48. Therefore, calculations show that scattering at 1 micron should be about two orders of magnitude smaller for crystals with the same size as in regular NaF PTR glass. Nevertheless, the used fluoride concentration is much larger than in regular PTR glasses. The chemical composition in this system was varied by reducing the CaF_2 concentration in order to avoid spontaneous precipitation of CaF_2 [30]. The glass described in the present paper was doped with Ag_2O, Ce_2O_3, KBr, SnO_2 and Sb_2O_3. In the following, the effect of irradiation and subsequent thermal treatment on the crystallization process and especially the role of KBr in the glass composition are described.

2. Experimental procedure

Glasses in the system $Na_2O/K_2O/CaO/CaF_2/Al_2O_3/SiO_2$ were melted from analytical grade Na_2CO_3, K_2CO_3, $CaCO_3$, CaF_2, ZnO, $Al(OH)_3$ and SiO_2 in batches of 300 g. The glass was additionally doped with Ag_2O, CeO_2, KBr, SnO_2 and Sb_2O_3. Further a glass without KBr in the batch was melted. The batch compositions are given in Table 1.

Table 1. Chemical composition of the glasses in wt%

Na_2O	K_2O	CaO	Al_2O_3	ZnO	SiO_2	CaF_2	KBr	Sb_2O_3	SnO_2	Ag_2O	CeO_2
8.7	7.8	10.7	5.8	0.9	54.4	9.8	1.8	0.2	0.02	0.04	0.03
8.9	7.9	10.9	5.9	0.9	55.4	10.0	-	0.2	0.02	0.04	0.03

The powdered components were accurately weighed and homogenized for 1 h with a ball mill. The material was melted in a covered platinum crucible using an inductive furnace at a temperature of 1400 °C for 3 h. The unavoidable fluorine loss, as determined by energy-dispersive X-ray (EDX) spectrometry using the scanning electron microscope (SEM) Jeol JSM 7001F FEM, amounted on average to about 39% ± 3%. After homogenizing the melt, it was cast in a preheated steel mould and given to a muffle furnace preheated to 530 °C. Then the furnace was switched off and the sample was allowed to cool. Differential thermal analyses (DTA, powdered sample heated at 10 K/ min) and dilatometer (heated at 5 K/ min, Netzsch 402) measurements were carried out to obtain values for the thermal properties. The glass transition temperature was found to be 520 °C and the onset of crystallisation was found to be 580 °C. Polished glass samples with a size of $1 \times 20 \times 10$ mm^3 were prepared. Irradiation of the samples was carried out using a sun simulator (Xe/Hg high pressure lamp, LOT Oriel) which emits at wavelengths larger than 195 nm. Irradiation power was 100 W/ cm^2. The sample was directly placed below the condenser lens. The samples were thermally treated in a muffle furnace in a one or two step process at a temperature of 530 °C for 1 h and at 560 °C for 20 h with a heating rate of 5 K/ min. Absorption of the samples was measured from 200 to 1200 nm using a double beam spectrophotometer (Shimadzu, 3101PC) by recording absorption of air as reference. Since all samples are of the same thickness, Fresnel reflection were not subtracted and absorption coefficients were not calculated.

From polished samples, X-ray diffraction (XRD) measurements were performed (Siemens D 5000) using a Cu anode ($\lambda_{K\alpha 1}$ = 1.789 Å) with a resolution of $2\theta = 0.05°$. The diffraction patterns were scanned over the 2θ range 10° - 60° with a 0.02° step width.

3. Results

In Table 2 conditions of sample preparation are listed including the time of exposure to radiation and the heat treatment steps. Samples with the additional label “Br0” were prepared from the Br-free glass.

Table 2. Conditions of sample preparation

sample ID	time of exposure to radiation [min]	1st heat treatment 530 °C/ 1 h	2nd heat treatment 560 °C/ 20 h
0	0	-	-
0A	0	x	-
0AB	0	x	x
30	30	-	-
30A	30	x	-
30B	30	-	x
10AB	10	x	x
30AB	30	x	x
60AB	60	x	x
0AB-Br0	0	x	x
30AB-Br0	30	x	x

All glasses and prepared samples were visually transparent. UV-vis absorption spectra were recorded from non irradiated and irradiated samples in order to evaluate structural changes during irradiation and heat treatment.

Figure 1 shows the absorption spectra of glass sample in the UV-vis range before and after irradiation. The spectrum of the non-irradiated sample shows an absorption peak at around 315 nm and an UV-cut off at around 275 nm which was determined with the tangent method. Exposure to radiation causes an increase of absorption in the short wavelength range.

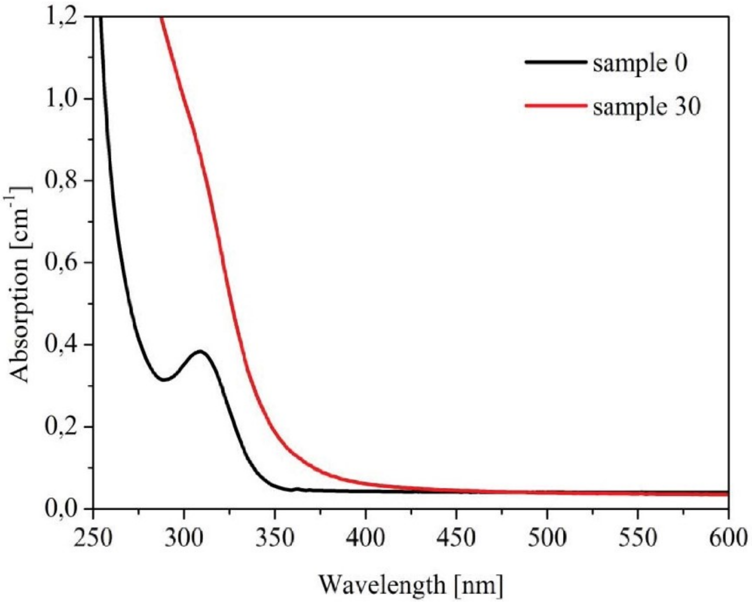

Fig. 1. Absorption spectra recorded of the non-irradiated base glass (sample 0) and after exposure to radiation (30 min, sample 30) using a high pressure Xe/Hg lamp emitting a continuous spectrum in UV region.

In Fig. 2, UV-vis absorption spectra of samples after thermal treatment are shown. The black curve (0AB) is attributed to a sample, which was only annealed at 530 °C for 1 h and at 560 °C for another 20 h without prior irradiation. The red and grey curves show spectra of samples which were irradiated (30 min) before thermal treatment. Irradiation and subsequent annealing at 530 °C give rise to the formation of a broad absorption peak at 425 nm. Irradiation and annealing in two steps, at 530 °C for 1 h and subsequently at 560 °C for another 20 h leads to a shift of the absorption band to larger wavelengths (440 nm) and to increasing intensity. Furthermore, these samples were transparent but show a yellow color. The peak at 440 nm is not observed in the sample which was annealed without prior irradiation. Moreover, heat treatment causes a decrease of absorption in the short wavelength range and the Ce^{3+} absorption band is observed again. While the absorption depends on the ratio of Ce^{3+} / Ce^{4+} higher temperatures prefer the stabilization of the reduced form.

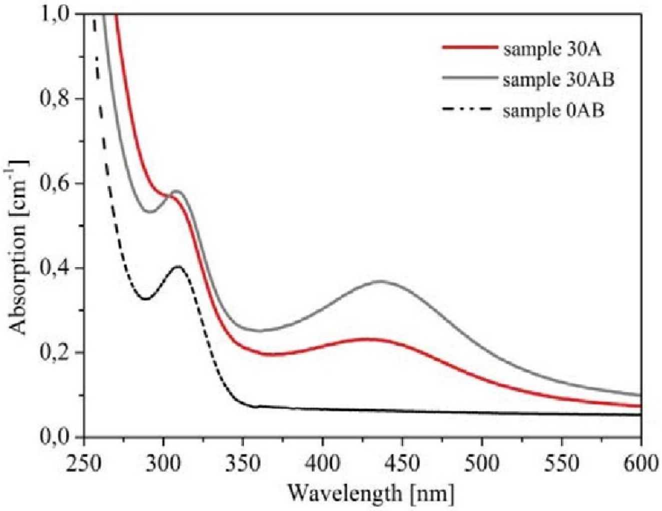

Fig. 2. Absorption spectra of glass samples after thermal treatment: (0AB) non-irradiated, annealed at 530 °C/ 1 h + 560 °C/ 20 h, (30A) irradiated (for 30 min), annealed at 530 °C/1 h, (30AB)) irradiated (for 30 min), annealed at 530 °C/ 1 h + 560 °C/ 20 h

In Fig. 3, XRD-patterns of the base glass and a sample without previous irradiation, just thermally treated at 530 °C for 1 h and finally annealed at 560 °C for another 20 h are shown. The glass sample which was neither irradiated nor thermally annealed was amorphous. The non-irradiated sample after subsequent thermal treatment at 530 °C for 1 h is also amorphous and does not show any hint at a crystalline phase. The pattern attributed to the sample annealed at 530 °C for 1 h and subsequently at 560 °C for another 20 h shows a peak of low intensity centred at 2θ = 28.4 deg which is attributed to cubic CaF_2 (JCPDS file no 35-0816). That means, without pre-irradiation CaF_2 crystals were barely developed.

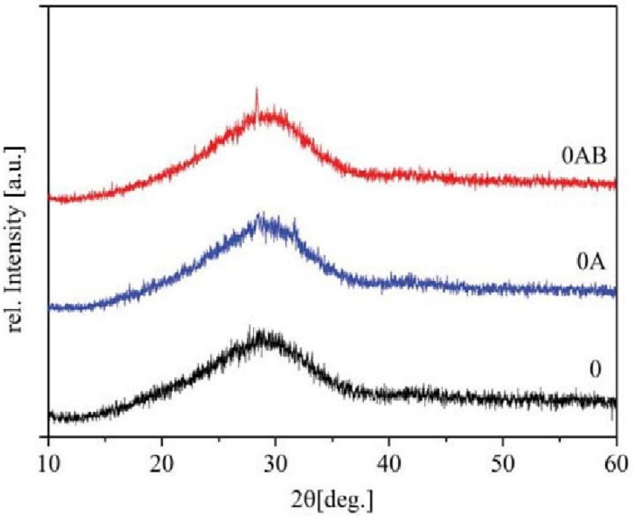

Fig. 3. XRD-patterns of samples after thermal treatment without prior irradiation: (0) base glass, (0A) 530 °C/ 1 h, (0AB) 530 °C/ 1 h + 560 °C/ 20 h.

In Fig. 4, an XRD-pattern of a sample which was first irradiated for 30 min and then annealed at 530 °C for 1 h is shown. The XRD-pattern shows two peaks of low intensity at 2θ = 28.4 deg and 2θ = 31.7 deg. The curve of sample 30B shows an irradiated sample which was subsequently thermally treated at 560 °C for 20 h. It shows a small intensity peak at 2θ = 28.4 deg. As curve of sample 30AB, an XRD-pattern of an irradiated sample later thermally annealed at 530 °C and at 560 °C for another 20 h is shown. This curve shows a high intensity peak at 2θ = 28.4 deg related to a notable volume fraction of CaF_2 crystals in the glass matrix.

In Fig. 5 UV-vis spectra of samples irradiated for different periods of time and subsequent annealed at 530 °C for 1 h and subsequently at 560 °C for 20 h are shown. The black curve shows the absorption spectrum after 10 min exposure to UV light and subsequent annealing. The red and the blue line were recorded after irradiation for 30 and 60 min, respectively; both samples were subsequently annealed. All spectra show a broad absorption band at around 440 nm related to silver clusters. The intensities of the peaks are larger if the samples were irradiated for 30 or 60 min. The curves for the 30 and 60 minutes of irradiation are the same within the limits of error.

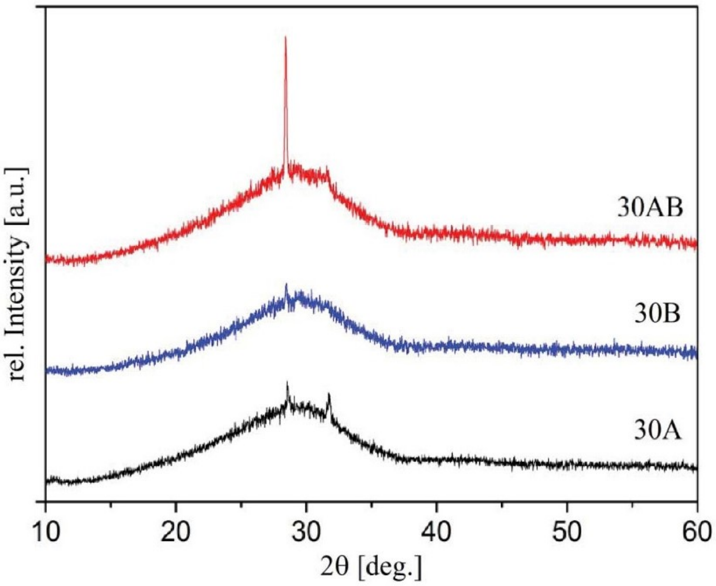

Fig. 4. XRD-patterns of samples after thermal treatment with previous irradiation for 30 min: (30A) irradiated, annealed at 530 °C/ 1 h, (30B) irradiated, annealed at 560 °C/ 20 h, (30AB) irradiated, annealed at 530 °C/ 1 h + 560 °C/ 20 h

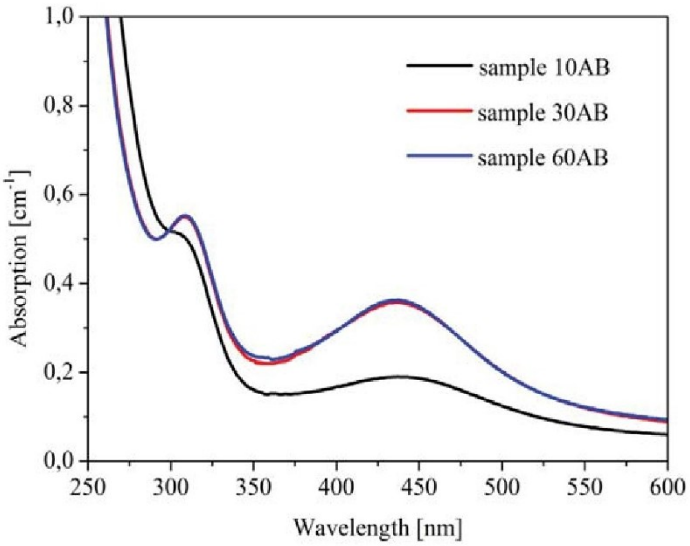

Fig. 5. Absorption spectra recorded after irradiation for different times and subsequent thermal treatment (530 °C/ 1 h + 560 °C/ 20 h): (10AB) 10 min irradiation, (30AB) 30 min irradiation, (60AB) 60 min irradiation.

In Fig. 6, XRD-patterns of samples first irradiated for different periods of time, then annealed at 530 °C for 1 h and finally annealed at 560 °C for another 20 h are shown. Longer irradiation times lead to a notable increase of the peak at $2\theta = 28.4$ deg. A tiny peak at $2\theta = 31.7$ deg is also observed. Furthermore after 60 min irradiation and subsequent heat treatment, peaks at $2\theta = 31.7$ deg and 57 deg occur.

The refractive index of the uncrystallized glass was 1.5485, whereas it was 1.5473 for the irradiated and heat treated sample. This means during the latter procedure the refractive index slightly increases.

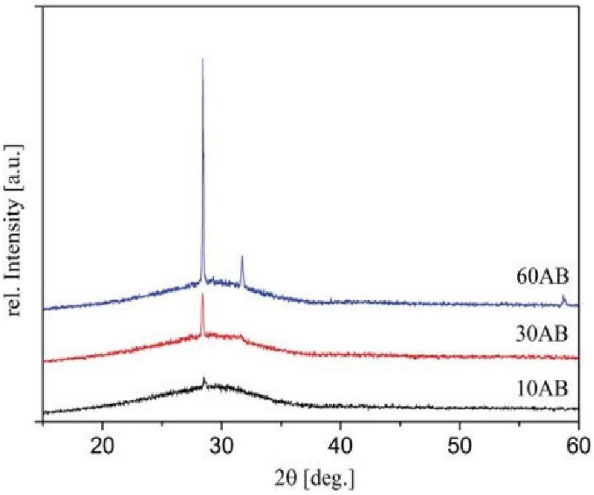

Fig. 6. XRD-patterns of samples first irradiated for different periods of time, then annealed at 530 °C for 1 h and finally annealed at 560 °C for another 20 h: (10AB) 10 min irradiation, (30AB) 30 min irradiation, (60AB) 60 min irradiation.

In Fig. 7, XRD-patterns of samples which were melted without using KBr as raw material are shown. The samples were exposed to radiation for 30 min or were not irradiated but in any case were thermally treated at 530 °C for 1 h and at 560 °C for 20 h. Pre-irradiated samples show a light yellow coloration after heat-treatment. The peak at $2\theta = 28.4$ deg occurs with low intensity both in the irradiated and in the non-irradiated samples. The XRD-patterns of both samples show a distinct peak at $2\theta = 46$ deg. These peaks are attributed to cubic CaF_2.

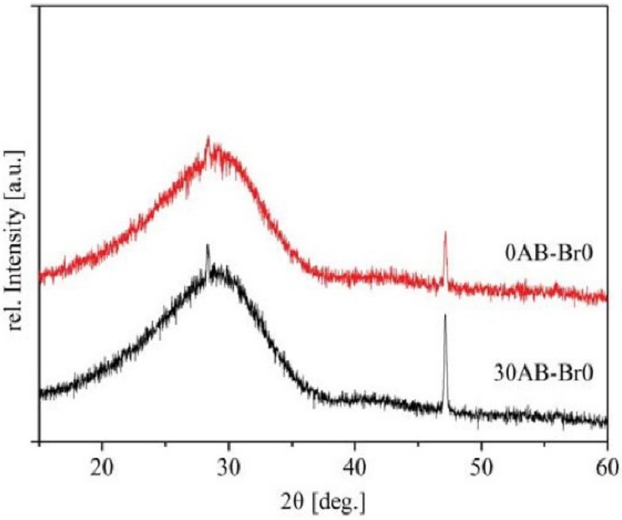

Fig. 7. XRD-patterns of samples without KBr in glass composition: (30AB-Br0) pre-irradiated (30 min) and (0AB-Br0) non-irradiated and thermal treated at 530 °C for 1 h and 560 °C for 20 h:

4. Discussion

The UV-vis absorption spectrum of the transparent and colorless non irradiated sample (see black curve in Fig. 1) shows a peak at around 315 nm. This peak is due to, the presence of Ce^{3+} (4f-5d bands) [31, 32]. During irradiation at a wavelength above 195 nm, the absorbance of the glass increases especially in the UV-range. The absorption at wavelengths $\lambda < 270$ nm is due to the combination of absorption of several components, such as Ce^{4+}, Ag^{+}, Sb^{3+} and Br^{-} [33] which overlap the peak due to Ce^{3+} at 315 nm. The changes in the spectra are caused by the following reactions. The Ce^{3+} of the glass absorbs the UV light and reacts to Ce^{4+} and an electron, Eq. (1).

$$Ce^{3+} + h\nu \rightarrow Ce^{4+} + e^{-} \quad (1)$$

The electron reacts with silver cations incorporated into the glass and forms metallic silver, Eq. (2).

$$Ag^{+} + e^{-} \rightarrow Ag^{0} \quad (2)$$

Ag^{-} as well as Ce^{4+} increases the absorption in the UV range.

Initial thermal treatment for 1 h at 530 °C (a temperature close to T_g) results in the formation of nucleation centers indicated by the yellow color of the sample. These nucleation centers are silver clusters which show characteristic absorption lines with a maximum at 425 nm (see Fig. 2). The absorption band is typical for the colloidal silver particles related to the surface plasmon resonance [34], Eq. (3).

$$nAg^0 \rightarrow Ag_n^0 \qquad (3)$$

The further growth of the colloidal silver particles Ag_n is hindered by the high matrix viscosity because the annealing temperature of the first annealing step is just above T_g (520 °C). Subsequent annealing at 560 °C for 20 h leads to the formation of CaF_2 crystals, furthermore to a shift of the absorption peak to 440 nm and to a further increase in the absorptivity. The change in the maximum position is caused by the size effects according to Mie theory, i.e. to a coarsening of the silver particles. Hence increasing intensity of the absorption band is also a result of scattering effects.. Samples without prior irradiation which nevertheless were thermally treated did not show a plasmonic resonance caused by clusters of elemental silver. Furthermore, the XRD patterns of samples without prior irradiation did not show distinct lines related to cubic CaF_2 as illustrated in Fig. 3. Samples that were thermally treated without previous UV irradiation barely develope CaF_2 crystals. By contrast, XRD patterns of samples which were not irradiated before thermal treatment do not show distinct lines as shown in Fig. 4. After irradiation and thermal treatment at 530 °C for 1 h a peak at $2\theta = 28.4$ deg attributed to cubic CaF_2 (JCPDS file no 35-0816) and a peak at $2\theta = 31.7$ deg appear. After thermal treatment at 530 °C for 1 h and at 560 °C for 20 h, the patterns of the pre-irradiated sample reveals an intense and narrow peak at $2\theta = 28.4$ deg related to CaF_2. This is a significant difference to the non-irradiated sample. Crystallization of CaF_2 was not observable after one step thermal treatment at 560 °C. Prior irradiation and a subsequent two step thermal treatment have a distinct effect on crystallization behavior of CaF_2 in the glass matrix. It should be noted that also the first step of the thermal treatment is quite essential; obviously silver clusters do not form at 560 °C and then also the crystallization of CaF_2 is not triggered.

Further investigations were aimed at the effect of irradiation time on crystal size and size distribution. The samples were irradiated for different periods of time and then the two step thermal treatment was performed. While the intensity of the plasmonic resonance, i.e. the concentration of the silver clusters strongly increased from 10 to 30 min irradiation time, a further extension did not result in an increase of the absorption maximum due to the plasmonic resonance, nor to a shift in the peak position (see Fig. 5). By contrast, the irradiation time has a significant effect on the volume concentration of CaF_2 as shown in the XRD patterns in Fig. 6. Longer irradiation times led to a notable increase of the intensity of the peak at $2\theta = 28.4$ deg attributed to cubic CaF_2. Although, the intensity of the plasmonic resonance peak is not changed, the concentration of crystalline fluoride is higher after thermal treatment. Possibly, silver clusters which are too small to cause plasmonic resonance peaks in the UV-vis absorption spectrum also act as nucleating agents. Furthermore after irradiation for 60 min, an additional peak at $2\theta = 57$ deg occurs which is also related to cubic CaF_2. After 30 min and 60 min irradiation time and subsequent two step heat treatment, also a peak at $2\theta = 31.7$ deg appears. The ratio of the intensity of these two peaks at $2\theta = 28.4$ deg and $2\theta = 31.7$ deg increases by a factor of two after using a twice as long exposure time. A peak at the same 2θ value has already been observed in Fig. 1 for a sample irradiated for 30 min and thermally treated at 530 °C for 1 h. In principle, this peak might be due to occurrence of AgBr which (200)-peak according to the JCPDS file no. 06-0438 fits well. Since the occurrence of silver in the glass is only 0.04%, the concentration seems to be very small for a peak of comparably high intensity. However, NaBr and AgBr form solid solutions at high temperatures, which, however, might decompose during cooling [35]. Nevertheless, NaF and also solid solutions with AgBr have lattice constants which are fairly similar to that of AgBr and more probably should be the reason for the occurrence of the peak at 31.7 deg. This peak appears only in KBr containing PTR glass and at a two step heat treatment (see Fig. 4). The same glass also shows the highest CaF_2 concentrations. The melting temperatures of sodium bromide and silver bromide are 755 °C and 428 °C, respectively. Hence, it can be assumed that the crystals are below their melting points and hence in the solid state.

In order to analyze how the absence of bromide affects the crystallization and the formation of this phase, a glass without KBr was produced and studied with respect to its crystallization behavior by X-ray diffraction. The formation of Ag^0 takes also place as indicated by a light yellow coloration after thermal treatment and pre-irradiation By comparison this CaF_2 containing glass without KBr does not show peaks for silver or sodium bromide in the XRD patterns (Fig. 7) after exposing to UV light and thermal treatment. In addition, a peak at $2\theta = 46$ deg occurs which is also attributable to cubic CaF_2 and the peak at $2\theta = 28.4$ deg has less intensity. This strengthens the assumption that crystal growth follows another mechanism in this case. Especially notable is that XRD pattern of the non-irradiated colorless sample also show peaks of notable intensity which are due to cubic CaF_2. This means that spontaneous crystallization occurs and a photo induced crystallization mechanism is not predominant in the studied composition under the supplied conditions. Recent studies on conventional PTR glasses demonstrated that bromide plays a key role also in the crystallization of NaF [12, 36]. It was shown that decreasing the bromide concentration severly hindered NaF crystallization. Hence, it seems that bromide plays an essential part for both, the precipitation of NaF as well as of CaF_2 in PTR glasses.

It should be noted that in the studied system, it was not possible to prepare samples which could be studied by TEM because the sample was damaged during irradiation with the electron beam [37]. This was also the case if using an aberration corrected TEM with an acceleration voltage of only 80 kV. By comparison in a similar system, enabling the precipitation of BaF_2 [26], TEM studies were possible even using electron energy loss spectroscopy. Since microscopic studies of the nanosized CaF_2 crystals were not successful, small angle X-ray scattering (SAXS) and anomalous small angle X-ray scattering (ASAXS) were used to determine the microstructure [38] as it has previously be reported for BaF_2 [39]. In this base $Na_2O/K_2O/CaO/CaF_2/Al_2O_3/SiO_2$ system [23] which does neither contain silver nor ceria and hence is not photosensitive, it has been shown that around the CaF_2 crystal, a thin layer enriched in SiO_2 exists. This structure has previously been postulated on the basis of the increase of the glass transition temperature during the course of the crystallization of CaF_2. The formation of such a layer and its effect on crystal growth has further been explained by theoretical models and numerical simulations [40, 41]. They assumed that the crystals first grow fast and then the chemical composition changes. Near the crystal, the melt is depleted in components which if added to the glass would lead to a decrease in the viscosity. That means during crystallization of alkali or alkaline earth fluorides, the viscosity increases near the crystals until the attributed T_g is larger than the crystallization temperature, then the system can no longer mechanically relax within the time scale of the experiment performed This all runs parallel to a drastic decrease in the crystal growth velocity [23, 24, 26]. Since in a first approximation, the refractive index should decrease with decreasing density, the photo induced crystallization should run parallel to a decrease in the refractive index [42]. However, as recently reported for a system which chemical composition is somewhat different, the photo refractivity is probably a much more complex effect.

Future work will be focused on the effect of laser irradiation on changes in the refractive index. We expect that due to the larger fluoride concentrations these changes should be larger than in other PTR glasses.

5. Conclusions

A new photo-thermo refractive glass composition is presented. Glasses in the system $Na_2O/K_2O/CaO/CaF_2/Al_2O_3/SiO_2$ were doped with Ag_2O, CeO_2, KBr, SnO_2 and Sb_2O_3. They were irradiated with UV light and subsequently thermally annealed in a two step process at 530 °C and subsequently at 560 °C. The irradiation led to the formation of metallic silver which forms clusters in the first annealing step. During the second annealing step, the crystallization of nano crystalline CaF_2 is observed as proved by X-ray diffraction. Furthermore, not irradiated PTR glass does not show CaF_2 crystallization supplying the same thermal treatment. The longer irradiation time, the higher is the volume density of CaF_2 crystals in the glass matrix. Glass samples from melts without KBr showed the precipitation of CaF_2 during a one or a two step thermal treatment without previous irradiation. This means that spontaneous crystallization predominates and no photoinduced mechanism controls the crystallization process. This strengthens the thesis that KBr plays an important role in the photoinduced crystallization process. Nevertheless, it would not be advantageous to replace Ag_2O and KBr by silver halides like AgBr or AgCl, which are well-known for their photosensitivity because these halides have low melting and boiling points. They might even be evaporated before the raw materials are completely melted. Finally, the new photo-thermo-refractive glass enables a controlled nanoscale crystallization of CaF_2 in limited areas.

Acknowledgment

This work was funded by the Bundesministerium für Forschung und Bildung, Germany (Wachstumskern Brightlas, 03WKCF3E)

Article 3.2

M. Stoica, A. Herrmann, J. Hein, C. Rüssel

UV-vis spectroscopic studies of a CaF_2 Photo-thermal-refractive glass

Optical Materials **2016** 62:424-432

DOI: http://dx.doi.org/10.1016/j.optmat.2016.10.031

UV-vis spectroscopic studies of a CaF_2 Photo-thermal-refractive glass				
Beteiligt an				
	Martina Stoica	Dr. Andreas Herrmann	Dr. Joachim Hein	Prof. Christian Rüssel
Konzeption des Forschungsansatzes	X			X
Planung der Untersuchung	X	X		
Datenerhebung	X		X	
Datenanalyse und Interpretation	X	X		
Schreiben des Manuskripts	X	X		X
Vorschlag Anrechnung Publikationsäquivalente	1,0			

Optical Materials 62 (2016) 424–432

Contents lists available at ScienceDirect

Optical Materials

journal homepage: www.elsevier.com/locate/optmat

UV–vis spectroscopic studies of CaF_2 photo-thermo-refractive glass

Martina Stoica [a,*], Andreas Herrmann [a], Joachim Hein [b], Christian Rüssel [a]

[a] Otto-Schott-Institut for Materials Research (OSIM), Fraunhoferstr. 6, Jena University, 07743 Jena, Germany
[b] Institute for Optics and Quantum Electronics (IOQ), Max Wien Platz 1, Jena University, 07743 Jena, Germany

ARTICLE INFO

Article history:
Received 8 July 2016
Received in revised form
5 October 2016
Accepted 17 October 2016
Available online 23 October 2016

Keywords:
Photosensitive glass
Photo-thermo-refractive glass
Absorption spectroscopy
Spectrum deconvolution
Cerium ions
Oxyfluoride glass

ABSTRACT

A photo-thermo-refractive glass based on the system $Na_2O/K_2O/CaO/CaF_2/Al_2O_3/ZnO/SiO_2$ doped with Ag_2O, CeO_2, SnO_2, Sb_2O_3 and KBr was investigated. This glass undergoes a permanent refractive index change after UV irradiation and subsequent two step heat treatment at temperatures above Tg. This is due to the formation of Ag metal clusters which act as nucleation centers for CaF_2 crystallization. Oxidation of Ce^{3+} by UV light is the initial reaction and acts as photosensitizer in the glass. The UV–vis absorption spectra during this photo-induced crystallization process were measured. The spectral components that form the absorption spectra of cerium were studied in detail by a band separation with Gaussian functions. Deconvolution of the cerium absorption bands shows an envelope of five spectral components for the trivalent cerium due to the 4f-5d transitions and two spectral components for the tetravalent cerium caused by charge transfer transitions. The effect of different dopants and melting conditions on the photo-thermal process were studied to investigate the influence of glass technology on the photoprocess.

1. Introduction

The development of a photo-thermo-induced crystallization process in glass wafers by D. Stookey [1] was the beginning for modern volume phase hologram writing which uses refractive index modulation in a photo-thermo-refractive (PTR) glass [2]. This is a silicate glass doped with Ce, Ag, Sn and Sb. During UV exposure, Ce^{3+} is oxidized ($Ce^{3+} + h\nu \rightarrow Ce^{4+} + e^-$) and the electron released is trapped by a silver ion which hence is reduced to a silver atom ($Ag^+ + e^- \rightarrow Ag^0$). The Ag atoms agglomerate during a subsequent heat treatment slightly above Tg and form metal cluster (MC) which act as nucleation centers for the formation of alkali or alkaline earth fluoride nanocrystals in the irradiated parts of the glass during the second heat treatment step [3]. Here bromine plays an important role [4–7]. The crystallization of nanocrystals leads to a permanent refractive index change in the afore UV-exposed areas [2]. This offers the possibility for structurization by hologram writing and to customize certain devices for photonic applications. From conventional PTR-glasses, after irradiation and two thermal treatment steps, NaF is precipitated. In the present study, a glass composition is used from which after irradiation and during the two thermal steps CaF_2 is crystallized. Light scattering is a general problem in optical materials, if two phases with different refractive indices occur and if the dimensions of theses phases are not very small in comparison to the wavelength of the used light. Light scattering can be avoided, if the refractive indices of the phases are nearly identical at all wavelengths and temperatures or the crystallite size is much smaller than the wavelength of the light used. If appropriate glass compositions are used, the precipitation of nanocrystals with a narrow size distribution can be achieved which avoids light scattering [8,9]. The precipitation of alkaline earth fluorides as CaF_2, BaF_2, SrF_2, LaF_3 and $NaGd(La)F_4$ from a glass matrix by thermal processes has already been described in the literature [10–14] which is accomplished by the occurrence of a diffusion barrier through the crystallization process [15–17]. A wide variation of annealing temperature and annealing time did not result in notably different crystallite sizes. Moreover, the refractive index of 1.43 for CaF_2 and the higher possible fluoride concentration in the glass has the potential for higher refractive index changes than NaF PTR glass. Further studies on this issue are in progress.

The PTR glasses reported in the literature contain a large number of polyvalent ions. In the present study, the main focus is the investigation of the spectral components of the different valencies of cerium. The electron donation ability by electronic excitation from the 4f to the 5d shell of the Ce^{3+} makes it the most important photosensitizer. The 4f-5d transitions of the Ce^{3+} and the CT

---

* Corresponding author.
E-mail address: martina.stoica@uni-jena.de (M. Stoica).

http://dx.doi.org/10.1016/j.optmat.2016.10.031

transitions of the Ce^{4+} are host sensitive [18–20]. Hence, the UV–vis absorption spectra of the Ce^{3+}/Ce^{4+} ions in glasses strongly depend on the type of glass [21–28]. For phosphate and borate glasses an envelope of five spectral components of the Ce^{3+} ion was reported which all were attributed to the $^2F_{5/2} \rightarrow$ 5d transitions. Five spectral components of the Ce^{3+} absorption are also reported for silicate glasses and crystals [21,23,43]. The splitting of the 5 d^1 energy level has a further influence on the spectral positions of the absorption peaks. Stronger splitting results in a shift of the absorption onset to lower energies. The splitting is reported to be mainly dependent on the Ce^{3+} coordination number and the Ce–O bond length but independent on the shift of the 5 d^1 level [29,30]. For borate and phosphate glasses Reisfeld et al. [24] proposed that Ce^{3+} is coordinated by eight oxygen atoms belonging to the corners of the BO_4 or PO_4 tetrahedra. This is in agreement with the incorporation of Ce^{3+} in calcium halide crystals as reported by Loh [26]: Ce^{3+} is coordinated by eight X^- ions ($X = F, Cl, Br$) and is situated inside a distorted cube with fluorine atoms in the corner positions.

In Ref. [31], for silicate based NaF photo-thermo-refractive glass, only two components of the absorption spectra were attributed to the Ce^{3+} ion. Furthermore, it was reported that UV exposure induces a new band resulting from a Ce^{3++} species. The authors state that a Ce^{3+} ion from which a fourth electron has been removed by photoionization is different from a Ce^{4+} ion because the structural relaxation to Ce^{4+} in a coordination shell with bond lengths and angles usually observed in a Ce^{4+} containing silicate glass is kinetically not possible. These conclusions were drawn from the difference in the absorption spectra of photoionized Ce^{3+} and Ce^{4+} [18]. In addition, it is assumed that the components of this spectrum are not allocated to the charge transfer but authors interpret the absorption spectrum of Ce^{4+} valence states as a series of excitonic excitations from orbitals of oxygen atoms that coordinate tetravalent cerium [31]. Afterwards, the deconvolution of the same spectra was processed by dispersion analysis, which was based on the analytical convolution model for the complex dielectric function of glasses. This method was applied to the initial experimental data, rather than to the difference spectra. This resulted in three spectral components in the absorption spectrum for both the trivalent and tetravalent cerium [32]. However, the electron released by Ce^{3+} during irradiation, leads to the formation of atomic Ag^0 which agglomerates during the first thermal treatment step to $Ag^0{}_n$ and allows the targeted CaF_2 crystallization responsible for the permanent refractive index change [5]. Since non-agglomerated Ag^0 does not show a specific absorption, the spectral changes during irradiation are solely due to cerium. By contrast, the formation of $Ag^0{}_n$ metal clusters can be observed in the UV–vis absorption spectra as a typical plasmon resonance peak at around 425 nm. Already in 1949 Stookey [1] proposed, that the silver particles grow by aggregation of silver atoms and hence a certain temperature is necessary to reach a sufficiently large diffusion coefficient for high enough growth velocities. Further investigations on the nucleation and growth kinetics of silver particles in a photo process show the requirement of UV light and that even small amounts of cerium sensitize this process [33]. The nucleation and growth of the silver particles in a photosensitive silica glass is affected by the dosage of exposure and even more by the heat treatment temperature. This was shown for PTR glass where the surface plasmon resonance (SPR) absorption band only occurs in UV exposed samples and increasing dosage of UV exposure results not only in a proportional shift of the SPR band maximum, but also in a change of the band halfwidth. A linear increase of the Ag absorption band with the UV dosage and a shift to higher wavelengths with increasing nucleation temperature up to a saturation level was reported from the NaF PTR glass [34,35]. UV–vis spectroscopic studies of Ag in a NaF PTR glass matrix have demonstrated a deconvolution to four single bands of the Ag related envelope, which are assigned to 4 $d^{10} \rightarrow 4d^9 5s^1$ transitions. Moreover, it was reported that the Br^- ions enter the coordination sphere of the Ag^+ ion [36] which corresponds with observations in X-ray diffraction [5]. The knowledge on the nature of the photo process involving Ce and Ag, and probably Sb and Sn is essential for the optimization of the recording process.

This paper provides a study on a new PTR glass, which in contrast to the conventional PTR glasses is based on the crystallization of CaF_2. The effect of UV-radiation and thermal treatment on the UV–vis spectra is described and discussed in detail.

2. Experimental

2.1. Glass preparation

All glasses were prepared from high purity raw materials (Fe < 10 ppm, other metal contaminations < 0.5 ppm). Glasses of the composition 9.2 Na_2O - 5.4 K_2O - 12.5 CaO - 8.2 CaF_2 - 3.7 Al_2O_3 - 0.7 ZnO - 59.2 SiO_2 (mol%) doped with different concentrations of Ag_2O, CeO_2, KBr, SnO_2 and Sb_2O_3 (see Table 1) were melted in a covered 0.2 l platinum crucible using an inductive furnace at a temperature of 1430 °C for 4 h. Sample C was also prepared while reducing conditions (argon atmosphere) were supplied. After the melt was homogenized with a Pt stirrer, it was cast to a preheated steel mold and given to a muffle furnace which was preheated to 530 °C. The temperature was held for 2 h, then the furnace was switched off and the glass was allowed to cool. Melting in reducing atmosphere and additional bubbling with argon was also performed to maintain reducing melting conditions.

Polished samples with a size of $10 \times 20 \times 1$ mm^3 for refractive index change measurements and $10 \times 20 \times 0.2$ mm^3 for UV–vis spectroscopic investigations were prepared from each batch. The density was measured using a helium pycnometer AccPyc 1330 (Micromeritics, Germany).

2.2. UV-exposure and heat treatment

Irradiation of the samples was carried out through a mask using an Excimer Laser at 308 nm with a constant pulse intensity of 22.5 mJ/cm^2 and 78.6 mJ/cm^2 using a pulse repetition rate of 1 Hz. The samples were nucleated in a muffle furnace at a temperature of 530 °C for 1 h, cooled to room temperature and then crystallized at 560 °C for 20 h. The supplied heating rate was 5 K/min and the furnace cooled with a rate of approximately 1 K/min.

2.3. Refractive index change measurements

Appropriate glass samples were selected by mapping of the striae with the shadow method. Refractive index changes in CaF_2 PTR glass were measured with an interference shearing microscope JENAPOL u. map (total image splitting) from repolished samples

Table 1
Dopant concentration in the respective glass samples (mol%).

sample code	KBr	Sb_2O_3	SnO_2	Ag_2O	CeO_2	melting atmosphere
A	1.0	0.04	0.01	0.01	0.025	non-reducing
B	1.0	0.04	0.01	0.01	0.1	non-reducing
C	1.0	0.04	0.01	0.01	0.025	reducing
D	1.0	0.04	0.01	0.01	–	non-reducing
E	–	–	–	0.01	0.025	non-reducing
F	–	–	–	–	0.025	non-reducing
G	–	–	–	–	0.025	reducing (&Ar-bubbling)
H	–	–	–	–	–	non-reducing

after heat treatment. Residual optical path differences due to striae were less than 5 nm per mm sample thickness.

2.4. UV–vis spectroscopy

Optical absorption spectra were recorded at room temperature in the wavelength range from 190 to 600 nm using a commercial double beam UV–vis–NIR spectrophotometer 3102PC (SHIMADZU, Japan) by recording absorption of air as reference and with an error of about ±1 nm. For these measurements, polished samples with a thickness of 0.2 mm were prepared very accurately. The absorbance was divided through the sample thickness $E/d = \lg(I_0/I)/d$. Although high purity raw materials were used, errors by impurities cannot be entirely ruled out. To separate the optical absorption due to Ce^{3+} and Ce^{4+} ions from the absorption of impurities for the deconvolution procedure, the absorption spectra were obtained by subtracting the spectra of undoped glass samples H from spectra of the doped glasses F and G.

3. Results and discussion

3.1. Refractive index change measurements

The CaF_2 PTR glass sample was exposed through a mask with a gap width of 2 mm to UV light with a constant pulse intensity of 78.6 mJ/cm^2 and different dosages. Hence, the sample is only partially irradiated admitting measurements with a shearing interferometer setup. The results are listed in Table 2. As the values in Table 2 show, permanent refractive index changes in this glass composition can be generated by the precipitation of the CaF_2 nanocrystals. Unfortunately, refractive index change measurements given in Ref. [5] are not identical due to the high error margin of the determination method used in there (conventional Abbe refractometer). Also, the optical homogeneity of the glass samples is of significant importance.

UV–vis spectroscopic studies of this glass are unavoidable to clarify the mechanism of the photoreaction which is initializing the nano crystallization of the CaF_2. However, an optimization of the process is possible.

3.2. UV–vis spectroscopic study of Ce^{3+}/Ce^{4+} absorption bands

The initial reaction of the photo-process is the excitation of the cerium ions by UV light (Eq. (1)).

$$Ce^{3+} + h\nu \rightarrow Ce^{4+} + e^{-} \tag{1}$$

All prepared glasses and samples were visually transparent. In Fig. 1, an absorption spectrum of the native CaF_2 PTR glass A is shown. This glass has shown photosensitivity in previous studies [5] and is suitable for photoinduced nano crystallization. High absorptions at wavelengths < 275 nm with a shoulder at 310 nm are observed.

According to the literature on conventional PTR glasses, the UV absorption edge and the high absorption in the UV range ($\lambda < 275$ nm) is due to the combination of absorption of the components Sb^{3+}, Sn^{2+}, Ag^{+} and Ce^{4+} [37,38]. The absorption band with a maximum at 310 nm is related to the Ce^{3+} absorption peak ($4f^1 \rightarrow 5d^1$). This absorption band sensitizes this glass to ultraviolet light. Furthermore, the higher the fluoride concentration, the more the Ce^{3+} absorption band is shifted to shorter wavelengths. This is caused by the halide effect (optical basicity) [39,40] and hence due to the shift of the $5d^1$ energy levels of Ce^{3+} to higher energies [29]. The high amount of fluoride in the CaF_2 PTR glass causes the low polarizability and comparatively low optical basicity (see Table 2) which leads to a shift of the redox equilibrium (see Eq. (2)) to the reduced state, i.e. to Ce^{3+}.

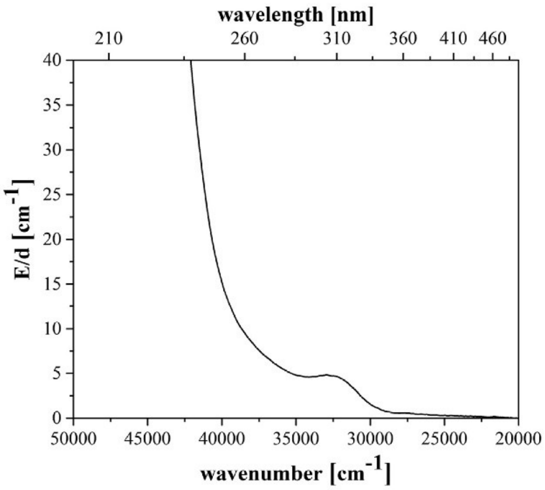

Fig. 1. UV–vis spectrum of CaF_2 PTR glass.

$$4Ce^{4+} + 2O^{2-} \leftrightarrow 4Ce^{3+} + O_2 \tag{2}$$

To understand the effect of cerium in the process, the optical absorption bands caused by Ce^{3+} and Ce^{4+} ions have to be separated. For this purpose, a glass without Ag, Sb, Sn, and Br (glass F, see Table 1) was melted and subsequently, the photoinduced crystallization process was studied with respect to the exposure to UV light and the two-step thermal treatment (see Fig. 2).

This glass F was melted under normal atmosphere. A broad absorption band from 200 nm to 360 nm with two maxima is observed. The maximum in the shorter wavelength range is caused by Ce^{4+} and the maximum located at 310 nm by the Ce^{3+} absorption. The exposed sample shows an increase of the Ce^{4+} absorption band. After the two step heat treatment (530 °C/1 h + 560 °C/20 h), the Ce^{4+} absorption band shows higher intensity while the maximum allocated to Ce^{3+} is decreased. However, from Fig. 2, it is seen that notable concentrations of Ce^{4+} occur if the glass was melted under non-reducing atmosphere, provided by the absorption maximum at higher energies, which is supposed to be mainly

Table 2
Optical path difference/refractive index change (calculated) on dosage of UV exposure in a CaF_2 PTR glass sample after heat treatment (530 °C/1 h + 560 °C/20 h).

Irradiation dosage [J/cm^2]	Optical path difference [nm]	Refractive index change
1.1	–	–
1.5	60	$6.32 \cdot 10^{-5}$
3.0	164	$1.73 \cdot 10^{-4}$

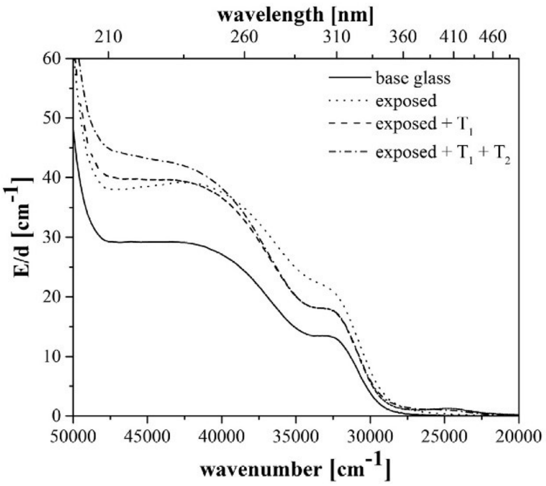

Fig. 2. UV–vis spectra of sample F before and after irradiation and subsequent heat treatment.

due to the CT transition of Ce^{4+}. The increase of this absorption leads to the assumption that the Ce^{3+}/Ce^{4+} ratio is decreased according to Eq. (2). This could also be due to scattering effects. Hence, as the absorption bands of Ce^{3+} and Ce^{4+} overlap each other, it is difficult to decide whether the spectrum represents the absorption of Ce^{4+} or a superposition of transitions of both Ce^{3+} and Ce^{4+} ions in the short wavelength range. In Refs. [21,22,41], it is shown how the Ce^{3+}/Ce^{4+} ratio is affected by the glass composition, the optical basicity and the melting conditions. The Ce^{3+}/Ce^{4+} redox equilibrium is closely related to the basicity of the glass and hence to the polarizability of the material. A decrease in basicity in nearly all cases reported in the literature results in a shift to the lower oxidation state [42]. For that reason, the theoretical optical basicity of the glass was calculated according to Ref. [39]. The averaged experimentally determined or calculated basicity values for the oxides and fluorides of Duffy and Lebouteiller/Courtine given in Refs. [39,43] have been used. The absorption spectra of Ce^{3+} and Ce^{4+} were investigated in detail by a deconvolution of the absorption spectra using Gaussian functions. The deconvoluted bands are characterized by the peak wave number, ν_p, the full width at half maximum, FWHM, and the intensity. From the absorption spectra and the extinction coefficients of Ce$^{3+/4+}$ given in Ref. [21] the concentration of Ce^{3+} and Ce^{4+} could be determined using Eq. (3).

$$N = 10^{-3} N_A \frac{E}{d\varepsilon} \tag{3}$$

Where N_A is the Avogadro number, d the sample thickness, ε the molar extinction coefficient, N the ion density and E is the absorbance or optical density defined from the measured intensity, I, as (Eq. (4))

$$E = \lg\left(\frac{I_0}{I}\right) \tag{4}$$

The calculation gives a Ce^{3+} concentration of $0.97 \cdot 10^{19}$ Ce^{3+}/cm^3. For Ce^{4+} an ion concentration of $0.3 \cdot 10^{18}$ cm^{-3} was determined resulting in an overall cerium concentration of about $1 \cdot 10^{19}$ cm^{-3}, which matches the actual value of about $1 \cdot 10^{19}$ cm^{-3}.

Fig. 3 shows the absorption spectrum and its deconvolution of a cerium doped glass sample (glass G) which was melted under reducing argon atmosphere and argon bubbling. Calculations of the theoretical optical basicity lead to the assumption that the Ce^{3+}/Ce^{4+} redox equilibrium is shifted to the reduced state. Additionally, if the glass is melted under reducing atmosphere with argon bubbling, most cerium is expected to be reduced to Ce^{3+} [22]. According to Refs. [21,22] the spectrum was fitted with seven Gaussian functions.

The five bands in the range from 350 to 200 nm with a constant moderate bandwidth are attributed to the 4f-5d transition of Ce^{3+}. The two broader absorption bands represent the CT transitions of Ce^{4+} ions. The addition of these broad absorptions for the CT transition indicates that a complete shift of the redox equilibrium to the reduced state was not possible.

Additionally, the same deconvolution procedure was applied to the absorption spectrum of the glass melted under non-reducing conditions (glass F, see Fig. 2). For the separation of the spectral components of Ce^{3+}/Ce^{4+}, the bands of Ce^{3+} and Ce^{4+} obtained from the deconvolution of the absorption spectra of the reduced sample (glass G, Fig. 3) have been added at the same spectral positions. The same procedure was applied to all other curves of glass F shown in Fig. 2 under the assumption that the absorption of the photoionized Ce^{3+} (Ce^{3++}) is identical to Ce^{4+} and no intrinsic color centers are generated [18,19]. The results are presented for the native glass F (Fig. 4), glass F after irradiation (Fig. 5), glass F after irradiation and subsequent heat treatment (Fig. 6) and glass F after irradiation and two step heat treatment (Fig. 7). Generally, the CT transitions of Ce^{4+} have higher intensities than the 4f-5d bands of Ce^{3+}. The Ce^{4+} charge transfer transitions are due to an electron transfer from oxygen and fluoride to the cerium ion. The 4f-5d band intensities of the deconvoluted absorption bands in glass F are decreased to about 2/3 of the intensities in glass G. By contrast, the Ce^{4+} CT transition intensities are four times higher than in glass G (see Fig. 4). Using the molar extinction coefficients of Ce$^{3+/4+}$ from Ref. [22] Ce^{3+} and Ce^{4+} concentrations of $0.63 \cdot 10^{19}$ cm^{-3} and $0.12 \cdot 10^{19}$ cm^{-3} were respectively calculated resulting in an overall

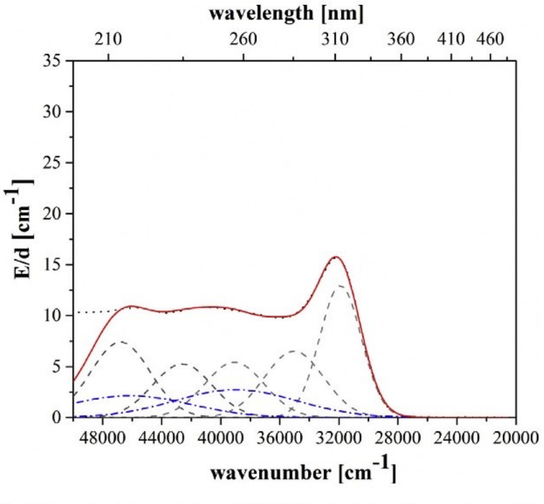

Fig. 3. Example of deconvolution of Ce^{3+}/Ce^{4+} optical absorption spectrum of the cerium doped sample G melted under reducing conditions with argon bubbling. The two dotted-dashed blue curves are attributed to Ce^{4+} and the five long-dashed grey curves represent the Ce^{3+} absorption. (For interpretation of the references to colour in this figure legend, the reader is referred to the web version of this article.)

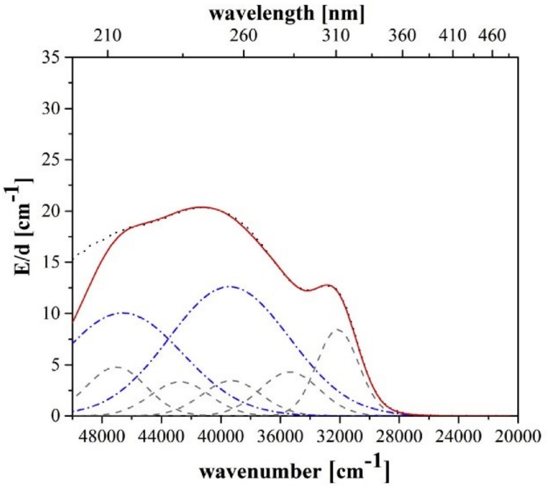

Fig. 4. Example of deconvolution of Ce^{3+}/Ce^{4+} optical absorption spectrum of native cerium doped sample F melted under non-reducing conditions (normal atmosphere). The two dotted-dashed blue curves are attributed to Ce^{4+} and the five long-dashed grey curves represent the Ce^{3+} absorption. (For interpretation of the references to colour in this figure legend, the reader is referred to the web version of this article.)

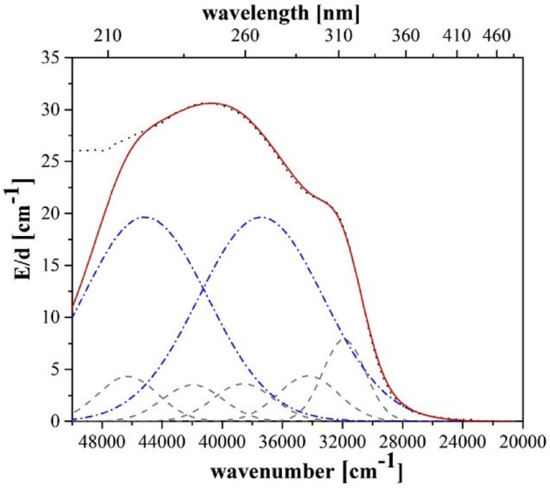

Fig. 5. Example of deconvolution of Ce^{3+}/Ce^{4+} optical absorption spectrum after exposure to UV light. The two dotted-dashed blue curves are attributed to Ce^{4+} and the five long-dashed grey curves represent the Ce^{3+} absorption. (For interpretation of the references to colour in this figure legend, the reader is referred to the web version of this article.)

cerium concentration of $0.75 \cdot 10^{19}$ cm^{-3} (see Table 3). This value is, contrary to the calculation for glass G, too low. However, from the absorption measurements, it is obvious that a noticeable concentration of Ce^{4+} ions occur in the native glass F, melted under non-reducing conditions. The error between the calculated and actual cerium concentrations can be caused by a difference in the absorption coefficients of the glass composition used here and the barium alumino silicate used in Ref. [22] or by an imprecise fitting procedure assuming a too low Ce^{4+} concentration in glass G.

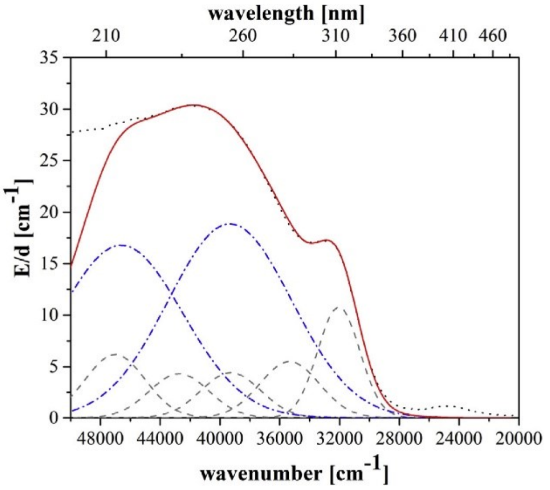

Fig. 6. Example of deconvolution of Ce^{3+}/Ce^{4+} optical absorption spectrum after exposure to UV light and heat treatment. The two dotted-dashed blue curves are attributed to Ce^{4+} and the five long-dashed grey curves represent the Ce^{3+} absorption. (For interpretation of the references to colour in this figure legend, the reader is referred to the web version of this article.)

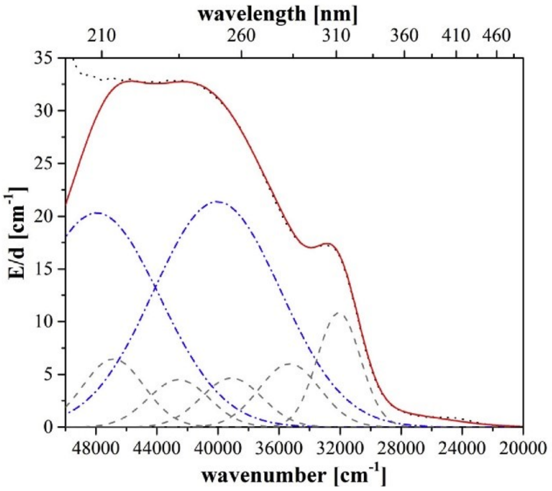

Fig. 7. Example of deconvolution of Ce^{3+}/Ce^{4+} optical absorption spectrum after exposure to UV light and two-step heat treatment. The two dotted-dashed blue curves are attributed to Ce^{4+} and the five long-dashed grey curves represent the Ce^{3+} absorption. (For interpretation of the references to colour in this figure legend, the reader is referred to the web version of this article.)

After exposure to UV light, the intensities of the Ce^{3+} bands are decreased and the Ce^{4+} band intensities are increased (Fig. 5). The deconvolution of the absorption spectrum obtained after exposure to UV light proves the oxidation of Ce^{3+} to Ce^{4+} (see Eq. (1)). A slight shift of the five Ce^{3+} absorption bands to lower wavenumbers is observed. This could be due to the generation of Ce^{3++} color centers which are different from Ce^{4+}. The color centers Ce^{3++} have the same valencies as Ce^{4+}, however, the bond lengths and -angles might be different and similar to those of Ce^{3+}. Therefore, Figs. 6

Table 3
Theoretical optical basicity for the CaF_2 PTR glass matrix and molar extinction coefficients of Ce^{3+}/Ce^{4+} at the respective peak absorption wavelengths.

	Glass G	Glass F
Density [g/cm^3]	2.606	2.608
Calculated cerium ion density [ions/cm^3]	Ce^{3+}: 0.97·10^{19} Ce^{4+}: 0.03·10^{19}	Ce^{3+}: 0.63·10^{19} Ce^{4+}: 0.12·10^{19}
Molar extinction coefficient [l/(cm*mol)] [21],	Ce^{3+}: 807 Ce^{4+}: 4735	Ce^{3+}: 807 Ce^{4+}: 4735
Wavelength [nm]	Ce^{3+}: 310 Ce^{4+}: 220	Ce^{3+}: 310 Ce^{4+}: 220
Theoretical optical basicity Λ_{th}	0.595	0.595

and 7 represent just examples for the deconvolution of the spectra of the thermal treated samples. The first thermal treatment at 530 °C for 1 h leads to an increase of the Ce^{3+} band intensities and a gentle decrease in the Ce^{4+} band intensities (Fig. 6). Also a change in the absorption spectra intensity is visible after the 2nd heat treatment (see Fig. 7). These results could be explained by the shift of the Ce^{3+}/Ce^{4+} redox equilibrium due to the heat treatment.

The obtained band positions of the components from this study and the data from literature for the barium alumino silicate (BaAS) glass [22] and the NaF PTR glass [37] are summarized and given in Table 4. From this data, a shift of the absorption lines to higher energies for the CaF_2-PTR glass can be observed in comparison to the BaAS glass due to its lower optical basicity.

The results of the deconvolution in this study are different from those in Refs. [31,37]. These previous studies wanted to achieve a deconvolution of the spectra by a minimum number of Gaussian functions. For this approach they independently extracted the bands of the Ce^{3+} and Ce^{4+} by using a mathematical combination of various spectra in all spectral regions. However, the results of the study described in the present paper is based on a physical model and confirms the role of the Ce^{3+} as important photosensitizer due to its electron donation ability by electronic excitation from the 4f to the 5d shell [44–46]. Additionally, it should be stated that during the photoionization of the Ce^{3+} intrinsic color centers Ce^{3++} are generated [18,19]. The Ce^{3++} species is different from Ce^{4+} which is confirmed by a change of the spectral position of the absorption maxima after irradiation. The result of deconvolution by a number of 7 Gaussian functions is independent of the generation of these color centers.

3.3. The effect of dopants on the photo-thermal process

The role of antimony and tin in this photoprocess was proved by preparing a glass without doping with tin and antimony. If only cerium and silver were involved in this process, the photoreaction should work without the other dopants. Hence, glass E was melted, which is only doped with cerium and silver, but not with tin, bromide and antimony. Samples of this glass E were also exposed to a dosage of 3.0 J/cm^2 and subsequently heat treated. The recorded UV–vis spectra are shown in Fig. 8.

The results are very similar to glass F (Fig. 2): an increase of the absorption in the UV wavelength region is observed after UV exposure, which can be attributed to the photo oxidation of Ce^{3+} to Ce^{4+}. After the heat treatment, the absorbance above 250 nm is further increased and the intensity of the absorption maximum at 310 nm is decreased. However, a closer examination of Figs. 2 and 8 reveals an additional absorption peak at around 220 nm, which is not visible in Fig. 2. This peak can be assigned to the d-s absorption of Ag^+ [47,48].

Additionally, the effect of the cerium concentration and UV

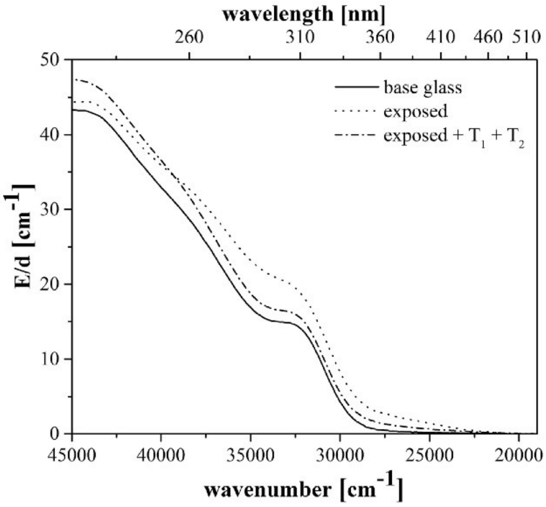

Fig. 8. UV–vis spectra of glass E before and after irradiation and subsequent heat treatment.

Table 4
Spectral components of Ce^{3+}/Ce^{4+} ions in the UV absorption spectra of CaF_2-PTR glass (this study), BaAS glass [22] and NaF-PTR glass [37].

Valence state	Spectral component	wave number of the respective absorption bands, [10^3 cm^{-1}]		
		CaF_2-PTRG (Glass F)	BaAS [22]	NaF-PTRG [37]
Ce^{3+}(4f-5d)	Ce^{3+} (1)	47.0	45.7	34.7
	Ce^{3+} (2)	42.7	37.2	32.8
	Ce^{3+} (3)	39.3	32.4	31.4
	Ce^{3+} (4)	35.4	30.6	
	Ce^{3+} (5)	32.1	30.0	
Ce^{4+} (CT)	Ce^{4+} (1)	46.6	45.2	49.4
	Ce^{4+} (2)	39.4	36.7	44.0
	Ce^{4+} (3)			38.7

radiation dosage on the absorption of the PTR glass with all dopants was investigated. The samples of glass A and B were exposed to UV light (308 nm) with different dosages. Fig. 9 shows absorption spectra recorded before and after irradiation with UV light, for glass samples with different cerium concentrations melted under normal, i.e. non-reducing conditions. At first sight it can be noted that the absorbance above 250 nm is much increased in comparison to Fig. 6 (cerium doping only) and Fig. 8 (cerium and silver doping). That means, besides Ag^{+} (see Fig. 8), also the additional ions tin and antimony ions absorb in this wavenumber range.

Also it is shown that the absorption bands of both cerium species increase with increasing cerium concentration in the glass sample, as expected. The prominent absorption band with a maximum at 310 nm is related to the Ce^{3+} absorption peak (4f^{1} → 5 d^{1}) which is superimposed by the broad band Ce^{4+} absorption between 300 and 200 nm as shown earlier by the deconvolution procedure. After irradiation, the absorption intensity increases with the dosage of UV exposure for both glasses: very nicely to be seen is the photo-oxidation of Ce^{3+} to Ce^{4+} (Ce^{3+} → Ce^{4+} + e^{-}), while the relative intensity of the Ce^{3+} peak at 310 nm is decreasing, the overall UV absorption is strongly increasing with increasing irradiation dosage due to the much higher extinction coefficient of Ce^{4+}. The relative decrease of the Ce^{4+} band intensities of glass A compared to glass E in Fig. 8 confirms the occurrence of processes in which antimony and tin ions are involved (Eq. (6), (7)). It is assumed that Ce^{4+} is reduced to Ce^{3+} due to the loss of trapped photo electrons by antimony and tin ions [49,50].

$$Sb^{3+} \rightarrow Sb^{5+} + 2e^{-} \tag{6}$$

$$Sn^{2+} \rightarrow Sn^{4+} + 2e^{-} \tag{7}$$

Moreover, both tin and antimony form redox equilibria with cerium in the melt. In the case of antimony, it can be written as (Eq. (8))

$$Sb^{3+} + 2Ce^{4+} \rightleftarrows Sb^{5+} + 2Ce^{3+} \tag{8}$$

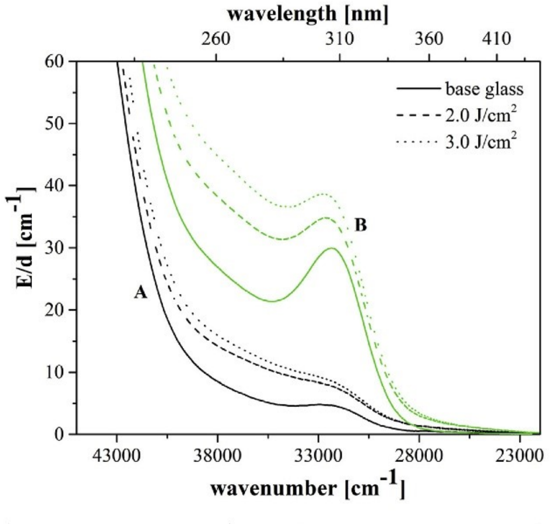

Fig. 9. UV–vis absorption spectra of sample A (0.025 mol% Ce) and sample B (0.1 mol% Ce), before and after exposure (dashed and dotted lines) to different dosages of UV light (308 nm).

Redox equilibria are always shifted to the oxidized state with decreasing temperature; an effect which depends strongly on the type of redox pair. If two or more redox pairs are present, the equilibrium is shifted with temperature according to the standard reaction enthalpies, ΔH°, of the respective redox pair. Since the Sb^{3+}/Sb^{5+} redox pair has a notably higher ΔH°, than the Ce^{3+}/Ce^{4+} redox pair according to [51,52] Eq. (8) is shifted to the right during cooling. That means, the addition of antimony to the glass composition helps to adjust a higher Ce^{3+}/Ce^{4+} ratio in the glass. That means, at high temperature, the Ce^{3+}/Ce^{4+} ratio should be the same if antimony is added, however, during cooling, the redox reaction is shifted and the Ce^{3+}/Ce^{4+} ratio increases. Hence, a higher concentration of Ce^{3+} occurs which enables the reduction of higher silver concentrations to elemental silver.

During heat treatment, the Ce^{4+} absorption notably decreases and the Ce^{3+} absorption band at 310 nm becomes more prominent again (see Fig. 10). The overall UV absorption is decreased. Additionally, a second absorption band with a maximum at 426 nm occurs after the initial heat treatment at 530 °C which is related to the silver plasmon resonance (SPR) of elemental silver [53,54]. The silver is forming clusters after trapping the electron which was released by the Ce^{3+} during the initial UV irradiation (Eqs. (9) and (10)). In this process the present Sb^{3+} and/or Sn^{2+} is supposed to act as redox buffer which contributes to the reduction of Ag^{+}. In glass E (Fig. 8), which was solely doped with silver and cerium, however, not with bromide, tin and antimony, after exposure to UV light and subsequent thermal treatment, the silver plasmon resonance peak was not observed. If no SPR absorption is observed in thermally treated samples, all silver occurs in the oxidized state, i.e. is dissolved as Ag^{+}, because all present Ag^{0} should have formed clusters. However, also glasses which were not exposed to UV-light, do not show any silver plasmon resonance [5].

$$Ag^{+} + e^{-} \rightarrow Ag^{0} \tag{9}$$

$$nAg^{0} \rightarrow Ag_{n}^{0} \tag{10}$$

The intensity of the SPR further increases with the second heat treatment step at 560 °C kept for 20 h. For glass B with the higher concentration of cerium, not only the absorption for the Ce^{3+} increases noticeably in the native glass sample, but also the intensity of the silver plasmon resonance is much higher after heat treatment. The centers of absorption maxima are located between 426 and 438 nm.

3.4. The effect of melting conditions on the photo-thermal process

Furthermore, the effect of non-reducing and reducing melting conditions was studied to clarify the effect of glass technology on the photoprocess. Fig. 11 shows a comparison of UV–vis spectra before and after irradiation and thermal treatment of glasses melted under non-reducing (sample A) and reducing conditions (sample C). Melting under reducing atmosphere should favor the reduced oxidation state according to Eq. (2). Here, the results are much different from the glasses without additional tin and antimony doping:

The intensities of the absorption bands at wavelengths < 350 nm of glass C melted under reducing atmosphere are slightly higher than those of glass A, melted under normal atmosphere, which is completely different from the glasses that only contain cerium (samples F and G). This cannot be an effect of the higher Ce^{3+} concentration in the reduced sample (slightly increased shoulder at around 310 nm for glass C), since Ce^{4+} has a much higher absorption coefficient than Ce^{3+}. Therefore, it is more likely an effect of increased UV absorption due to other polyvalent ions in

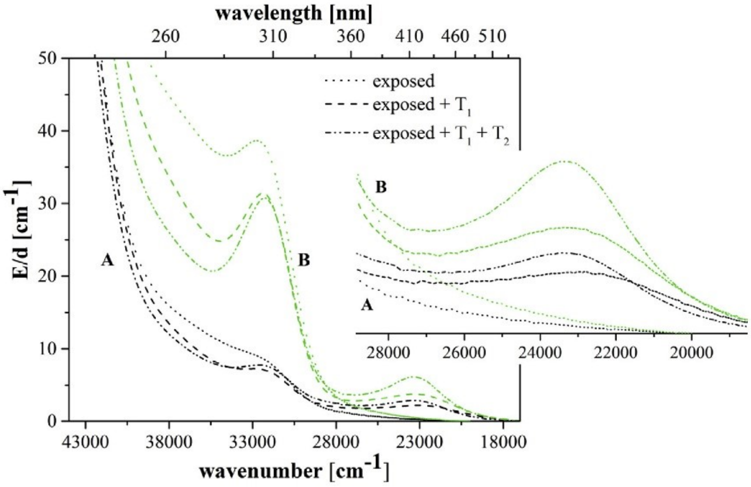

Fig. 10. UV–vis absorption spectra of sample A (0.025 mol% Ce) and sample B (0.1 mol% Ce) irradiated with the same dosage (3.0 J/cm^2) and subsequently heat treated at T$_1$ (530 °C/1 h) and T$_2$ (560 °C/20 h).

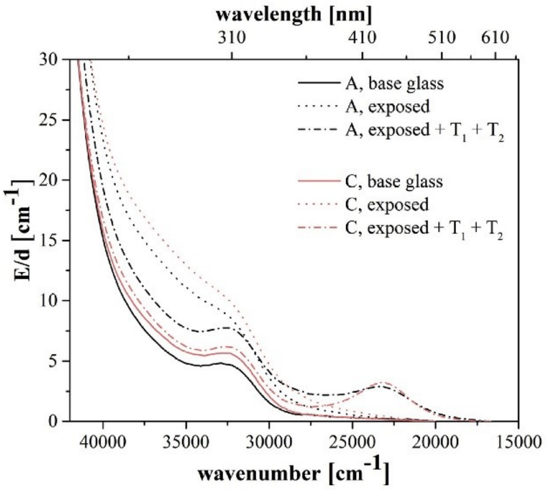

Fig. 11. UV–vis spectra of glass A (non-reducing melting atmosphere) and glass C (reducing melting atmosphere) before (full line), after exposure (dotted line) to UV light (308 nm) and subsequent thermal treatment at 530 °C/1 h and 560 °C/20 h (dotted-full-line).

lower oxidation states as e.g. Sn^{2+} or Sb^{3+} [55]. After irradiation with UV light of a dosage of 3.0 J/cm^2 the absorption band of Ce^{3+} is only observed as a small shoulder due to the overlapping with the increased Ce^{4+} absorption bands. Increased absorption of Sn^{2+} and Sb^{3+} ions may play an additional role [50]. However, photooxidation is stronger for the formerly reduced glass sample. After heat treatment the silver plasmon resonance absorption intensity at around 430 nm is slightly higher. For samples which were exposed to a UV light dosage of 2.0 J/cm^2 the difference between the SPR intensities is larger (not shown). Also, the maximum of the SPR peak seems to be shifted to lower energies for glass C (reduced sample). This means, the silver cluster size is higher in the formerly reduced sample [56].

4. Conclusion

Glass samples of a PTR glass, which in contrast to the conventional PTR glass is based on the crystallization of CaF_2 were prepared. This glass undergoes a permanent refractive index change after exposure to UV light and a subsequent two step thermal treatment. The effect of UV irradiation and thermal treatment on the UV–vis absorption spectra was investigated for glasses with different combinations of dopant ions and produced under different melting conditions. The oxidation of Ce^{3+} to Ce^{4+} by UV light is the initial reaction of the photo process. Therefore, a detailed deconvolution of the spectra for the absorption bands of the two different cerium valence states was carried out after each step of the photo-thermal process by using 7 Gaussian functions. Five bands with moderate bandwidths are attributed to the 4f-5d transitions of Ce^{3+}; two broader absorption bands represent the charge transfer transitions of Ce^{4+}. The application of reducing melting conditions (argon bubbling) did not result in a complete shift of the Ce^{3+}/Ce^{4+} redox equilibrium to the reduced state. Hence, a noticeable concentration of Ce^{4+} ions still occurs in the reduced glass. The deconvolution of the absorption spectra proves the oxidation of Ce^{3+} to Ce^{4+} during the exposure to UV light. The subsequent heat treatment results in the reverse effect, the cerium ions are reduced to the lower oxidation state again. Tin and antimony are essential for the photo-thermal process. It could be proved that metallic silver clusters are only formed in the tin/antimony codoped samples. More silver ions are reduced to elemental silver at higher cerium concentrations indicated by an increasing silver plasmon resonance peak. The formation of silver clusters is also more efficient in the formerly reduced sample. If no SPR absorption is observed in thermally treated samples, all silver occurs in the oxidized state, i.e. is dissolved as Ag^+.

Acknowledgement

This work was funded by the Bundesministerium für Forschung und Bildung, Germany (Wachstumskern Brightlas, 03WKCF3E).

References

[1] S.D. Stookey, Photosensitive glass - a new photographic medium, Ind. Eng. Chem. 41 (1949) 856–861.

[2] V.A. Borgman, L.B. Glebov, N.V. Nikonorov, G.T. Petrovskii, V.V. Savvin, A.D. . tsetkov, Photothermorefractive effect in silicate-glasses, Dokl. Akad. Nauk. Sssr+ 309 (1989) 336–339.

[3] L.B. Glebov, N.V. Nikonorov, Y.I. Panysheva, G.T. Petrovskii, V.V. Savvin, I.V. Tunimanova, V.A. Tsekhomskii, Multichromatic glasses - a new material for recording of volumetric phase Holograms.Dokl, Akad. Nauk. Sssr+ 314 (1990) 849–853.

[4] K. Ritter, S. Gerlach, C. Rüssel, Photo induced surface near crystallization of a glass in the system $Na_2O/K_2O/CaO/CaF_2/Al_2O_3/SiO_2$, J. Non-Cryst. Solids 356 (2010) 3090–3094.

[5] M. Stoica, G.N.B.M. de Macedo, C. Rüssel, Photo induced crystallization of CaF_2 from a $Na_2O/K_2O/CaO/CaF_2/Al_2O_3/SiO_2$ glass, Opt. Mater. Exp. 4 (2014) 1574–1585.

[6] G.P. Souza, V.M. Fokin, C.A. Baptista, E.D. Zanotto, J. Lumeau, L. Glebova, L.B. Glebova, Effect of bromine on NaF crystallization in photo-thermo-refractive glass, J. Am. Ceram. Soc. 94 (2011) 2906–2911.

[7] L. Glebova, J. Lumeau, M. Klimov, E.D. Zanotto, L.B. Glebov, Role of bromine on the thermal and optical properties of photo-thermo-refractive glass, J. Non-Cryst. Solids 354 (2008) 456–461.

[8] C. Bocker, S. Bhattacharyya, T. Höche, C. Rüssel, Size distribution of BaF_2 nanocrystallites in transparent glass ceramics, Acta Mater. 57 (2009) 5956–5963.

[9] R.P.F. de Almeida, C. . Bocker, C. Rüssel, Size of CaF_2 crystals precipitated from glasses in the $Na_2O/K_2O/CaO/CaF_2/Al_2O_3/SiO_2$ system and percolation theory, Chem. Mater. 20 (2008) 5916–5921.

[10] C. Bocker, J. Wiemert, C. Rüssel, The formation of strontium fluoride nano crystals from a phase separated silicate glass, J. Eur. Ceram. Soc. 33 (2013) 1737–1745.

[11] A. de Pablos-Martin, G.C. Mather, F. Munoz, S. Bhattacharryya, T. Höche, J.R. Jinschek, T. Heil, A. Duran, M.J. Pascual, Design of oxy-fluoride glass-ceramics containing $NaLaF_4$ nano-crystals, J. Non-Cryst. Solids 356 (2010) 3071–3079.

[12] C. Rüssel, Nanocrystallization of CaF_2 from $Na_2O/K_2O/CaO/CaF_2/Al_2O_3/SiO_2$ glasses, Chem. Mater. 17 (2005) 5843–5847.

[13] S. Tanabe, H. Hayashi, T. Hanada, N. Onodera, Fluorescence properties of Er^{3+} ions in glass ceramics containing LaF_3 nanocrystals, Opt. Mater. 19 (2002) 343–349.

[14] A. Herrmann, M. Tylkowski, C. Bocker, C. Rüssel, Preparation and luminescence properties of glass-ceramics containing Sm^{3+}-doped hexagonal $NaGdF_4$ crystals, J. Mater. Sci. 48 (2013) 6262–6268.

[15] C. Bocker, C. . Rüssel, I. Avramov, Crystal growth in non-isochemical, highly viscous liquids and percolation theory, Chem. Phys. 406 (2012) 50–54.

[16] A. Höll, Z. Varga, V.S. Raghuwanshi, M. Krumrey, C. Bocker, C. Rüssel, ASAXS study of CaF_2 nanoparticles embedded in a silicate glass matrix, J. Appl. Crystallogr. 47 (2014) 60–66.

[17] V.S. Raghuwanshi, A. Höll, C. Bocker, C. Rüssel, Experimental evidence of a diffusion barrier around BaF_2 nanocrystals in a silicate glass system by ASAXS, Crystengcomm 14 (2012) 5215–5223.

[18] J.S. Stroud, Photoionization of Ce^{3+} in glass, J. Chem. Phys. 35 (1961) 844–850.

[19] J.S. Stroud, Color centers in a cerium-containing silicate glass, J. Chem. Phys. 37 (1962) 836–841.

[20] M. Stephan, M. Zachau, M. Groting, O. Karplak, V. . eyert, K.C. Mishra, P.C. Schmidt, A theoretical investigation of 4f -> 5d transition of trivalent rare earth ions in fluorides and complex oxides, J. Lumin. 114 (2005) 255–266.

[21] H. Ebendorff-Heidepriem, D. Ehrt, Formation and UV absorption of cerium, europium and terbium ions in different valencies in glasses, Opt. Mater. 15 (2000) 7–25.

[22] A. Herrmann, H.A. Othmann, A.A. Assadi, M. Tiegel, S. Kuhn, C. Rüssel, Spectroscopic properties of cerium-doped aluminosilicate glasses, Opt. Mater. Exp. 5 (2015) 720–732.

[23] J.L. Rygel, C.G. Pantano, Synthesis and properties of cerium aluminosilicophosphate glasses, J. Non-Cryst. Solids 355 (2009) 2622–2629.

[24] R. Reisfeld, J. Hormodal, B. Barnett, Ce-$^{3+}$ as a probe of crystal-field and nature of impurity-ligand bond in borate and phosphate glasses, Chem. Phys. Lett. 17 (1972) 248–251.

[25] J.C. Krupa, M. Queffelec, UV and VUV optical excitations in wide band gap materials doped with rare earth ions: 4f-5d transitions, J. Alloy. Compd. 250 (1997) 287–292.

[26] E. Loh, Ultraviolet absorption spectra of Ce^{3+} in alkaline-earth fluorides, Phys. Rev. 154 (1967) 270–276.

[27] V.I. Arbuzov, M.N. Tolstoi, Photochemical properties of activated glass, J. Non-Cryst. Solids 123 (1990) 258–265.

[28] J.A. Duffy, G.O. Kyd, Ultraviolet absorption and fluorescence spectra of cerium and the effect of glass composition, Phys. Chem. Glas. 37 (1996) 45–48.

[29] P. Dorenbos, 5d-level energies of Ce^{3+} and the crystalline environment. III. Oxides containing ionic complexes, Phys. Rev. B 64 (2001) 283–299.

[30] G. Blasse, B.C.Grabmeier,Luminescent Materials, Springer, Berlin, 1994.

[31] M.L. Brandily-Anne, J. Lumeau, L. Glebova, L.B. Glebov, Specific absorption spectra of cerium in multicomponent silicate glasses, J. Non-Cryst. Solids 356 (2010) 2337–2343.

[32] A.M. Efimov, A.I. Ignatèv, N.V. Nikonorov, E.S. Postnikov, Spectral components that form UV absorption spectrum of Ce^{3+} and Ce(IV) valence states in matrix of photothermorefractive glasses, Opt. Spectroscop+ 111 (2011) 426–433.

[33] U. Kreibig, Small silver particles in photosensitive glass - their nucleation and growth, Appl. Phys. 10 (1976) 255–264.

[34] A.P. Nacharov, N.V. Nikonorov, A.I. Sidorov, V.A. Tsekhoskii, Influence of ultraviolet irradiation and heat treatment on the morphology of silver nanoparticles in photothermorefractive glasses, Glass Phys. Chem. 34 (2008) 693–699.

[35] J. Lumeau, L. Glebova, L.B. Glebov, Influence of UV-exposure on the crystallization and optical properties of photo-thermo-refractive glass, J. Non-Cryst. Solids 354 (2008) 425–430.

[36] A.M. Efimov, A.I. Ignatèv, N.V. Nikonorov, E.S. Postnikov, Ultraviolet-Vis spectroscopic manifestations of silver in photo-thermo-refractive glass matrices, Glass Technol.-Part A 54 (2013) 155–164.

[37] A.M. Efimov, A.I. Ignatèv, N.V. Nikonorov, E.S. Postnikov, Quantitative UV-VIS spectroscopic studies of photo-thermo-refractive glasses. II. Manifestations of Ce^{3+} and Ce(IV) valence states in the UV absorption spectrum of cerium-doped photo-thermo-refractive matrix glasses, J. Non-Cryst. Solids 361 (2013) 26–37.

[38] E.M. Sgibnev, A.I. Ignatèv, N.V. Nikonorov, A.M. Efimov, E.S. Postnikov, Effects of silver ion exchange and subsequent treatments on the UV-VIS spectra of silicate glasses. I. Undoped, CeO_2-doped, and ($CeO_2 + Sb_2O_3$)-codoped photo-thermo-refractive matrix glasses, J. Non-Cryst. Solids 378 (2013) 213–226.

[39] J.A. Duffy, Optical basicity of fluorides and mixed oxide-fluoride glasses and melts, Phys. Chem. Glasses- B 52 (2011) 107–114.

[40] E.I. Panysheva, I.V. Tunimanova, The role of fluorine ions in the polychromatic process, Glass Phys. Chem. 22 (1996) 125–131.

[41] V.I. Arbuzov, Photostimulated electron transfer between coactivator ions in alkali silicate glasses, J. Non-Cryst. Solids 253 (1999) 37–49.

[42] J.A. Duffy, A review of optical basicity and its applications to oxidic systems, Geochim. Cosmochim. Ac. 57 (1993) 3961–3970.

[43] V. Dimitrov, T. Komatsu, Classification of simple oxides: a polarizability approach, J. Solid State Chem. 163 (2002) 100–112.

[44] P. Dorenbos, Relating the energy of the [Xe]5d1 configuration of Ce3+ in inorganic compounds with anion polarizability and cation electronegativity. Phys. Rev. B, [65] (200).

[45] M.J. Weber, Optical-spectra of Ce^{3+} and Ce^{3+}-Sensitized fluorescence in $YAlO_3$, J. Appl. Phys. 44 (1973) 3205–3208.

[46] G.A. Slack, S.L. Dole, V. Tsoukala, G.S. Nolas, Optical-absorption spectrum of trivalent cerium in Y_2O_3, Ba_2GdTaO_6, ThO_2, and related-compounds, J. Opt. Soc. Am. B-Opt. Phys. 11 (1994) 961–974.

[47] C. Pedrini, Spectroscopic investigation of isolated silver ions in lithium-chloride single-crystal, J. Phys. Chem. Solids 41 (1980) 653–657.

[48] H. Bach, F.G.K. Baucke, Ultraviolet-absorption spectrum of the Ag^{+} ion in glass, Phys. Chem. Glas. 27 (1986) 215–217.

[49] H. Hosono, Y. Abe, H. Kawazoe, H. Imagawa, Solarization mechanism of glass containing Ce^{3+} and As^{5+}, J. Non-Cryst. Solids 63 (1984) 357–363.

[50] A.M. Efimov, A.I. Ignatèv, N.V. Nikonorov, E.S. Postnikov, Photo-thermo-refractive glasses: effects of dopants on their ultraviolet absorption spectra, Int. J. Appl. Glass Sci. 6 (2015) 109–127.

[51] C. Rüssel, E. Freude, Voltammetric studies of the redox behavior of various multivalent ions in soda-lime-silica glass melts, Phys. Chem. Glas. 30 (1989) 62–68.

[52] A. Paul, R.W. Douglas, Cerous-ceric equilibrium in binary alkali borate and alkali silicate glasses, Phys. Chem. Glas. 6 (1965) 212–215.

[53] U. Kreibig, Kramers kronig analysis of optical properties of small silver particles, Z. Phys. 234 (1970) 307–318.

[54] U. Kreibig, P. Zacharia, Surface plasma resonances in small spherical silver and gold particles, Z. Phys. 231 (1970) 128–143.

[55] D. Ehrt, M. Leister, A. Matthai, Polyvalent elements iron, tin and titanium in silicate, phosphate and fluoride glasses and melts, Phys. Chemis. Glas. 42 (2001) 231–239.

[56] U. Kreibig, M. Vollmer, Optical Properties of Metal Clusters, Springer Berlin Heidelberg, 1995. Berlin, Heidelberg.

Article 3.3

M. Stoica, C. Patzig, C. Bocker, M. Kracker, W. Wisniewski, T. Höche, C. Rüssel

Structural Evolution of CaF_2 Nano Particles During the Photoinduced Crystallization of a $Na_2O/K_2O/CaO/CaF_2/Al_2O_3/ZnO/SiO_2$ Glass

Journal of Materials Science **2017** 52(23):13390-13401

DOI: 10.1007/s10853-017-1443-5

Structural Evolution of CaF_2 Nano Particles During the Photoinduced Crystallization of a $Na_2O/K_2O/CaO/CaF_2/Al_2O_3/ZnO/SiO_2$ Glass							
Beteiligt an							
	Martina Stoica	Dr. Christian Patzig	Dr. Christian Bocker	Dr. Michael Kracker	Dr. Wolfgang Wisniewski	Prof. Thomas Höche	Prof. Christian Rüssel
Konzeption des Forschungsansatzes	X					X	X
Planung der Untersuchung	X	X					
Datenerhebung	X	X	X	X	X		
Datenanalyse und Interpretation	X				X		
Schreiben des Manuskripts	X	X		X	X		X
Vorschlag Anrechnung Publikationsäquivalente	1,0						

Article 3.3

J Mater Sci

Ceramics

Structural evolution of CaF_2 nanoparticles during the photoinduced crystallization of a $Na_2O–K_2O–CaO–CaF_2–Al_2O_3–ZnO–SiO_2$ glass

Martina Stoica[1,*], Christian Patzig[2], Christian Bocker[1], Wolfgang Wisniewski[1], Michael Kracker[1], Thomas Höche[2], and Christian Rüssel[1]

[1] *Otto-Schott-Institut, Jena University, Fraunhoferstraße 6, 07743 Jena, Germany*
[2] *Fraunhofer Institute for Microstructure of Materials and Systems IMWS, Walter-Huelse-Straße 1, 06120 Halle (Saale), Germany*

Received: 18 May 2017
Accepted: 31 July 2017

ABSTRACT

A glass in the system $Na_2O–SiO_2–Al_2O_3–K_2O–CaO–CaF_2–ZnO$ was doped with Ce, Ag, Sn, Sb and Br. Homogeneous and transparent glass ceramics are obtained from this glass by the precipitation of CaF_2 nanoparticles. An interface-controlled crystallization mechanism hinders crystal growth after some time. By adding photosensitive agents, a tailored photoinduced CaF_2 crystallization was achieved. Structural evolution during irradiation and heat treatment was investigated by different electron microscopic techniques, e.g., scanning transmission electron microscopy (STEM) including energy-dispersive X-ray analysis (EDXS) and scanning electron microscopy (SEM) including electron backscatter diffraction (EBSD). Agglomerated structures with a size of ca. 35 nm were observed after the first thermal treatment at 530 °C. The Ag nucleation is accompanied by clustering of several components within the glass. CaF_2 particles with diameters of ca. 300 nm with a spherulitic structure are observed in the glass ceramic after the second heat treatment step at 560 °C. Calcium and fluoride are depleted from the glass matrix during crystallization, while SiO_2 is enriched. From (S)TEM micrographs, supplemented by selected area diffraction (SAD), outward growth of CaF_2 from a central point is observed. STEM–EDXS analyses show residual glass within the spherulitic structure.

Introduction

Photo-thermo-refractive (PTR) glass can be structured by light and subsequent thermal treatment [1]. Traditional PTR glasses are usually within the system $Na_2O–SiO_2–NaF–Al_2O_3–ZnO$ and activated with Ag_2O, CeO_2, Sb_2O_3 and SnO_2. Irradiation by UV light with a wavelength of 325 nm triggers a redox reaction, which leads to the formation of metallic Ag in the glass. A controlled thermal treatment slightly above the glass transition temperature T_g [1–3] leads to the precipitation of NaF in the irradiated regions.

Address correspondence to E-mail: martina.stoica@gmx.de

DOI 10.1007/s10853-017-1443-5

Springer

The irradiated and subsequently crystallized regions of the glass will then exhibit a lower refractive index in comparison with the non-irradiated regions [1, 4, 5]. Irradiation with two beams of light which show interference enables the preparation of volume Bragg gratings (VBGs) and thus of materials with a periodic arrangement of alternating layers of high and low refractive indices [6]. Different types of optical elements are conceivable: transmitting Bragg gratings [7], reflecting Bragg gratings [8], chirped Bragg gratings [9] and phase plates [10]. These elements enable a wide field of applications in laser system technology. Transmitting Bragg gratings are used for the phase locking of multimode lasers [11]. Reflecting Bragg gratings find application as angularly and spectrally selective elements in spectral or coherent beam combining of high-energy lasers [12, 13]. Chirped Bragg gratings are efficient optical materials for stretching and compression of ultra-short-pulse lasers [14].

A PTR glass within the system Na_2O–SiO_2–Al_2O_3–K_2O–CaO–CaF_2–ZnO, i.e., with a chemical composition very different from that of conventional PTR glasses, but also doped with Ce, Ag, Sn, Sb and Br, was recently reported [15]. In this glass, the formation of CaF_2 nanocrystals was observed after irradiation with UV light and a subsequent two-step thermal treatment. The advantage is that the solubility of CaF_2 is much larger in this oxyfluoride glass than that of NaF in the conventional PTR glass. Potentially, higher differences in the refractive indices between irradiated and non-irradiated regions may thus be achieved.

This new glass enables the production of transparent and homogeneous glass ceramics [16]. The nanoparticles in the glass matrix grow via an interface-controlled crystallization mechanism [17] also reported for the precipitation of oxides such as Fe_3O_4 [18–20] and fluorides (BaF_2 [21–25], SrF_2 [26, 27], LaF_3 [28–30], $NaGaF_4$ [31, 32] and CaF_2 [16, 33, 34]) from glasses. The glassy phase near the crystals is enriched in Si and Al, but depleted in Ca and F during growth, because these components form the CaF_2 crystal. These local changes in element concentrations result in the formation of a diffusion profile around the crystal [23, 34], and this leads to an increased viscosity in a shell around the crystal, followed by a subsequent strong decrease in the diffusion coefficients. The latter effect has also been described for other systems, such as a BaF_2-containing multicomponent system [25], where the viscosity around the BaF_2 nanocrystals is increased to values which are high enough to completely freeze further crystal growth [17]. Hence, growth may be restricted to crystal sizes of a few nanometers with a narrow size distribution and a tailored photoinduced CaF_2 crystallization can be achieved by adding photosensitive agents, which finally results in a local refractive index change [15, 35].

As in the conventional PTR glass, exposing the CaF_2-containing glass to UV light leads to the formation of metallic Ag in a photo-thermo-ionization process. This is a complex redox process involving several species: $Ce^{3+/4+/3++}$, $Sn^{2+/4+}$ and $Sb^{3+/5+}$. Ce^{3+} is photoionized to Ce^{4+} (Ce^{3++}) and releases an electron. It should be mentioned that Ce^{3++} has the same oxidation number as Ce^{4+} and the coordination sphere is, however, somewhat different and more similar to that of Ce^{3+}. The thus generated photoelectrons are trapped in trapping centers, which are in principal constituted by Sb^{5+}. Electrons are also trapped by Ag^+ which is therefore reduced to elemental Ag^0. Furthermore, an increase in the temperature leads to the release of the photoelectrons from the $[Sb^{5+}]^-$ centers, which are subsequently trapped by Ag^+. Therefore, metallic Ag clusters are formed during the first annealing step which is performed just above T_g [36, 37]. These silver clusters again act as nuclei for the CaF_2 crystallization in a second heat treatment step performed at a temperature further above T_g. The resulting transparent glass ceramics contain CaF_2 nanocrystals with narrow size distributions and are interesting for photonic applications [38]. Local refractive index changes also make them suitable for holographic optical elements (HOEs) [6, 39, 40].

A liquid–liquid phase separation (LLPS) was reported to occur during heat treatment in conventional NaF PTR glasses [1, 41]. It is assumed that LLPS leads to unwanted scattering losses and uncontrolled refractive index changes. It was reported that adding bromide is able to prevent this effect [42], probably by changing the solubility of NaF in the glass and consequently the driving force of crystallization. Adding small bromide concentrations leads to smaller NaF crystals, and a higher volume fraction of crystals can be achieved [43]. This has a great influence on the refractive index change and light scattering in the visible (vis) spectrum [44]. Similar crystal size changes due to bromide addition were observed in PTR glasses suited for making CaF_2-containing glass–ceramics [15]. While the bromide-free glasses barely crystallized at all, adding bromide provoked a notable crystallization of CaF_2. Numerical simulations showed that the formation of a dielectric shell of AgBr around silver nanoparticles would explain the plasmon absorption band changes during the heat treatment [45, 46].

Further studies on oxyfluoride glasses demonstrated that some glass compositions showed LLPS during heat treatment, forming a droplet phase enriched in Ca and F. In many cases, the droplets subsequently crystallized to CaF_2. Hill et al. remarked that the phase separation caused by Ca^{2+} and F^- in the glass occurs much easier than the nucleation of a crystalline phase, because the interfacial energy between two glassy phases is much lower than that between a glassy and a crystalline phase [47–49].

In order to control the heterogeneous crystallization, triggered by light and thermal development, the present work is focused on structural investigations of the crystallization process in a CaF_2-forming photosensitive glass in the system Na_2O–SiO_2–Al_2O_3–K_2O–CaO–CaF_2–ZnO. This paper provides a detailed study of the crystallization mechanism for the first time and combines the different electron microscopic techniques of scanning transmission electron microscopy (STEM) including energy-dispersive X-ray analysis (EDXS), supplemented by selected area diffraction (SAD), and scanning electron microscopy (SEM) including electron backscatter diffraction (EBSD).

Experimental

A glass with the composition 59.6 SiO_2–9.2 Na_2O–5.4 K_2O–12.0 CaO–8.4 CaF_2–3.7 Al_2O_3–0.7 ZnO–1.0 KBr (mol%) was melted from analytical grade Na_2CO_3, K_2CO_3, $CaCO_3$, CaF_2, ZnO, KBr, $Al(OH)_3$ and SiO_2 in a 300-g batch. The glass composition was chosen, because a comparably high alkali oxide concentration is required to facilitate the melting process. The reason for a partial replacement of sodium oxide by potassium oxide is the suppression of additional NaF crystallization. The goal is to only crystallize CaF_2. The glass was additionally doped with 0.01 Ag_2O, 0.01 CeO_2, 0.02 SnO_2 and 0.04 Sb_2O_3 (mol%). The batch was melted in a covered 200-ml platinum crucible using an inductive furnace at a temperature of 1430 °C, where the melt was held for 4 h. It was homogenized with a Pt stirrer (75 rpm), then cast into a preheated steel mold and placed into a muffle furnace, and preheated to 530 °C for 2 h before the furnace was switched off, allowing the glass to slowly cool to room temperature (RT). The glass was cut into pieces of $10 \times 20 \times 1$ mm^3 and subsequently polished on the opposing large surfaces.

Samples were irradiated with UV light using a high-pressure Xe arc lamp (LOT Oriel). Two steps of thermal treatment were performed in a muffle furnace (Nabertherm N11/H): step 1 at 530 °C for 1 h and step 2 at 560 °C for 20 h. The heating rate was 5 K min^{-1}. Respective sample treatments are listed in Table 1.

Optical absorption spectra of the samples with 1 mm thickness were recorded at RT using wavelengths from 200 to 1000 nm by a commercial double-beam UV–Vis–NIR spectrophotometer (3102PC, Shimadzu) with air as the reference; the error in the wavelength is about ±1 nm.

The dispersion of the glass was calculated using the Wemple equation [50].

$$\frac{1}{n^2(E)-1} = \frac{E_s}{E_d} - \frac{E^2}{E_s E_d} \tag{1}$$

where E is the light energy (=hν), E_s is the Sellmeier gap and E_d is the dispersion energy. Refractive indices were measured at 20 °C with a Pulfrich refractometer PR2 equipped with a VoF5 prism at certain wavelengths according to the Fraunhofer lines (C, d, e, F, g and h). A linear regression of the measured values using the curve $1/(n^2-1)$ vs. E^2 enables the calculation of the optical dispersion of the glass for a further adaption. The freely available software "MiePlot" ver. 4.6 (supplied by Laven [51] and based on the BHMIE algorithm [52]) was used to calculate the optical behavior of Ag nanoparticles with different sizes in a glass matrix. The required dielectric function of Ag is based on data provided by Johnson and Christy [53]. The plasmon resonance wavelengths of the calculated and measured spectra were

Table 1 Conditions of sample preparation

Material	Irradiation	$T_1 = 530$ °C/1 h	$T_2 = 560$ °C/20 h
A	–	–	–
B	X	X	–
C	X	X	X

determined by fitting the peaks with a Gaussian function and locating of the center of gravity.

Thermal analyses were performed on polished samples using a non-isothermal differential scanning calorimeter (DSC 822, Mettler Toledo) with a heating rate of 10 K min^{-1} from 50 to 650 °C. X-ray diffraction (XRD) measurements were taken over a 2θ range from 10° to 60° (recorded with a step size of 0.02 nm and a scanning speed of 1°/min) on compact samples using an X-ray diffractometer Rigaku Miniflex 300.

The microstructure of irradiated and thermally treated samples was analyzed using electron microscopy. A scanning electron microscope (JSM 7001F FEM, JEOL) equipped with an EDAX Trident analyzing system containing a TSL Digiview 3 EBSD-camera and energy-dispersive X-ray spectroscopy (EDXS) was used. Electron backscatter diffraction (EBSD) patterns were acquired and evaluated using the program TSL OIM Data Collection 5.31.

(Scanning) Transmission electron microscopy in combination with energy-dispersive X-ray spectroscopy [(S)TEM-EDXS] was performed using a transmission electron microscope (Titan^3 G280-300, FEI Company) operated at 80 kV and equipped with a SuperX-EDXS detector (FEI Company). The STEM images were acquired using a high-angle annular dark-field (HAADF) detector (Fischione Model 3000, Fischione). The visualization of the lateral element distribution by means of EDXS mapping of the peak intensity of the K_α X-ray emission lines was performed using the commercially available software Esprit 1.9 (Bruker Company). The samples for the STEM experiments were prepared by a purely mechanical wedge polishing approach, followed by a low-energy (2.5 keV) Ar^+ ion broad beam polishing with a precision ion polishing system (PIPS, Gatan).

Results

The prepared glass was visually transparent and colorless. Refractive indices at the corresponding wavelengths are 1.5384 at 435.8 nm, 1.5341 at 480.0 nm, 1.5296 at 546.0 nm, 1.5275 at 587.6 nm and 1.5252 at 643.8 nm. DSC measurements provided a $T_g = 519$ °C for the native glass (material A in Table 1) and a $T_g = 526$ °C for material B. Figure 1 presents the optical absorption spectra in the UV–Vis range for the materials A and B. The native glass shows an absorption peak at around 310 nm, which can be attributed to absorption by Ce^{3+} ions [54]. An increasing absorption for wavelengths below 290 nm is observed. According to the literature on conventional PTR glass, the UV absorption edge, and the high absorption in the UV range ($\lambda < 290$ nm) is due to the combined absorption of the components Sb^{3+}, Sn^{2+}, Ag^+ and Ce^{4+} (see [55–57]).

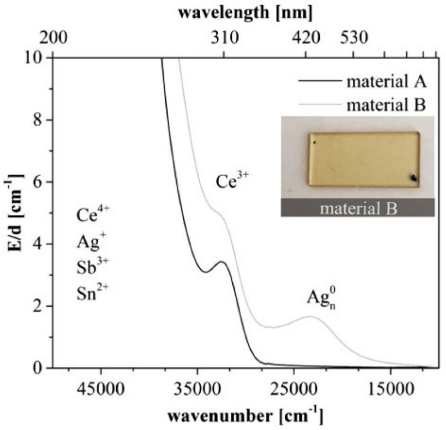

Figure 1 UV–Vis spectra of the materials A and B.

After irradiation and heat treatment at 530 °C for 1 h, the material shows a yellowish coloration. The absorption in the short wavelength range is increased, and the previously observed Ce^{3+}-induced absorption peak developed into a shoulder. An additional peak is now observed at a wavelength of 428 nm, which can be attributed to the silver plasmon resonance of Ag^0 particles (see Ref. [58]).

Figure 2a shows a TEM micrograph of material B. The microstructure appears inhomogeneous, and structures with diameters of roughly 20–50 nm are

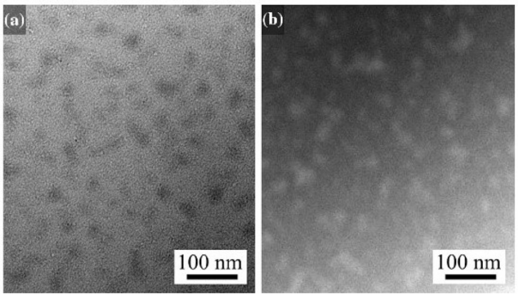

Figure 2 **a** TEM micrograph and **b** HAADF micrograph of the material B.

observed in the glass matrix. The dark appearance of these inhomogeneities could be due to an increased absorption of the primary electron beam, i.e., a mass-thickness-contrast mechanism, and hence indicate a densification of these areas in comparison with the surrounding glass.

It was not possible to analyze these structures directly via STEM-EDXS due to extensive sample damage by the electron beam. However, the silver plasmon resonance absorption band in Fig. 1 indicates that Ag particles occur in this material. A high-angle annular dark-field (HAADF) STEM micrograph of this material is shown in Fig. 2b, where the structures appear brighter than the surrounding matrix. As HAADF imaging is based on the inelastic scattering of electrons within the sample and is thus very sensitive to atomic numbers, this suggests a higher average atomic number of these structures in comparison with the glass matrix. This is in agreement with the TEM micrograph in Fig. 2a, where the dark appearance of the structures is most possibly due to an increased electron absorption due to a locally higher density.

Assuming a spherical shape of the particles enables to calculate their volume fraction from Fig. 2. Average sphere diameters were calculated to be 35 nm by visually fitting circle equivalents to the particles. The thickness of the TEM sample is assumed to be between 30 and 50 nm. If, in a simple approximation, the area density of the particles is assumed to be approximately equal to the volume density, the latter can be estimated to be ≈20–30%. However, the calculated volume fraction of Ag in the glass melt (0.1558 g $AgNO_3$ in 300 g glass batch) is only 0.008%. Hence, it is clear that the particles cannot be solely composed of Ag. More likely, the observed structures are liquid–liquid phase separations.

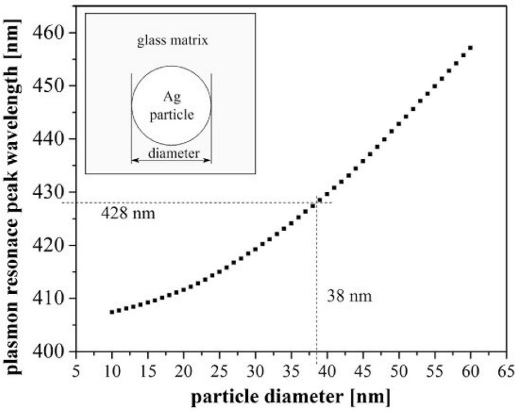

Figure 3 Simulated plasmon resonance peak positions for a single Ag particle in the glass matrix of the current system. The *dashed line* corresponds to the Ag plasmon resonance wavelength determined from Fig. 1.

A simulation of the expected plasmon resonance in this glass matrix was performed and is shown in Fig. 3 in order to compare the peak at 428 nm observed in the spectrum shown in Fig. 1 (attributed to the plasmon resonance of Ag) with the structures presented in Fig. 2.

The resonance wavelength increases from 407 nm for a particle of 10 nm diameter up to 457 nm for a particle 60 nm in diameter. Thus, this simulation covers the representative wavelength range for the Ag^0 plasmon peak observed in Fig. 1. These results will be discussed later.

The second heat treatment step at 560 °C for 20 h is performed in order to grow CaF_2 around the Ag-containing nuclei and hence to obtain the glass-ceramic material C. Spontaneous (homogeneous) nucleation cannot be ruled out during this process [15, 16]. The samples become slightly light scattering during this second annealing step, meaning that the overall scattering is increased. The latter is determined by the sum of the scattering at each individual crystal [3].

Figure 4 presents XRD patterns obtained from compact samples of the materials A–C. As expected, the native glass is X-ray amorphous. After irradiation and the first annealing step, no peaks are observed in the corresponding XRD pattern. After the second annealing step, two peaks are observed at $2\theta = 28.4°$ and 47.2°.

Figure 5 shows SEM micrographs of a fractured surface of material C, etched using diluted hydrofluoric acid (HF, 5%) to increase the topographical contrast. Bright spherical particles with diameters of up to ca. 300 nm are observed. Figure 5a shows a surface tilted by 70° to enable a 3D impression. The underlying structures with straight edges but the same contrast and chemical composition (determined by EDXS in the SEM) as the matrix are probably artifacts of the etching routine. Two of these spherical particles are presented in greater detail in Fig. 5b to show that they are not homogeneous and

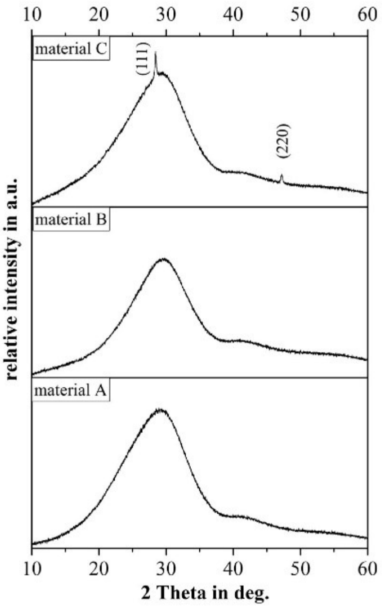

Figure 4 XRD patterns of the native glass A and the glass–ceramics B and C.

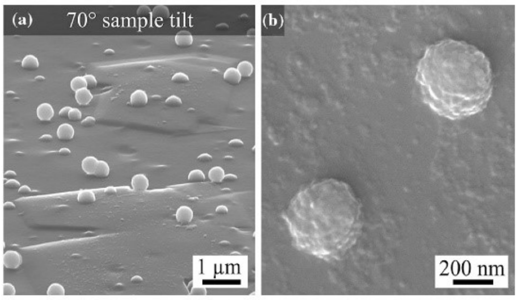

Figure 5 SEM micrographs of material C: **a** sample tilted by 70°, **b** two particles in greater detail, no sample tilt.

possess a substructure <50 nm in size. SEM-EDXS showed the enrichment of Ca and F in these particles.

An EBSD analysis of these features is presented in Fig. 6. The EBSD patterns 1–3 were obtained from elongated crystals rarely observed in the microstructure. While the patterns 1 and 2 may be reliably indexed as cubic CaF_2, pattern 3 has a slightly weaker intensity but already contains not enough details to be reliably indexed. The patterns 1 and 2 were obtained from opposite ends of one crystal. Pattern 4 is representative for the pattern quality obtained from the spherical nanoparticles, which is also too low to allow reliable indexing, making EBSD scans of these particles useless. EBSD patterns could not be obtained from the underlying structures shown in Fig. 5a.

The TEM micrographs of glass-ceramic C shown in Fig. 7 feature cross sections through the spherical particles. They are clearly inhomogeneous, which explains the low EBSD pattern quality of pattern 4 in Fig. 6. With dark-field TEM imaging by using only selected, diffracted electrons with the help of an objective aperture placed in the back-focal plane of the TEM enable to qualitatively image crystalline areas, which then appear bright due to the diffraction.

Figure 8 shows a further cross section through a nanoparticle as well as selected area diffraction (SAD) patterns obtained in the TEM by restricting the information volume to the circled areas with an appropriate aperture. The bright sphere around the particle is an artifact of the electron beam.

Analyzing chemical compositions in these materials via STEM-EDXS is problematic. Figure 9 illustrates particles in material C before and after STEM-EDXS analysis. The analyzed area was clearly modified by the electron beam.

Nevertheless, a qualitative analysis of the element distribution is possible. EDXS spectra obtained from a particle and the glass matrix are presented in Fig. 10 to show that the signal of the dopant elements is either too small (e.g., Ag, Ce), superimposed by elements of the glass (e.g., Sn, Sb), or both. The element-dependent detection limit of EDXS usually ranges from 0.5 to 1.0 at%.

Hence only the EDXS element maps of Ca, F, Si, Na, K, Al, Zn and O are shown in Fig. 11. As expected, Ca and F are enriched in the particles, while the glass matrix mainly contains Si and O as well as Na, K, Al and Zn which are in turn depleted in the particles.

Discussion

During the course of the photoreaction and the subsequent clustering of the silver atoms, the network modifier Ag_2O is removed from the glass network. Simultaneously, Ce^{3+}, which primarily acts as network modifier, is oxidized to Ce^{4+} which acts as a

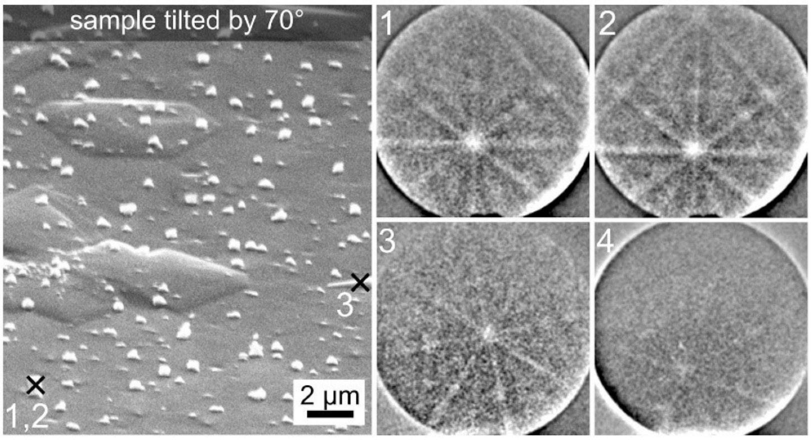

Figure 6 SEM micrograph of material C and EBSD patterns 1–4 acquired at the locations 1–3 as well as at 4: from one of the bright particles.

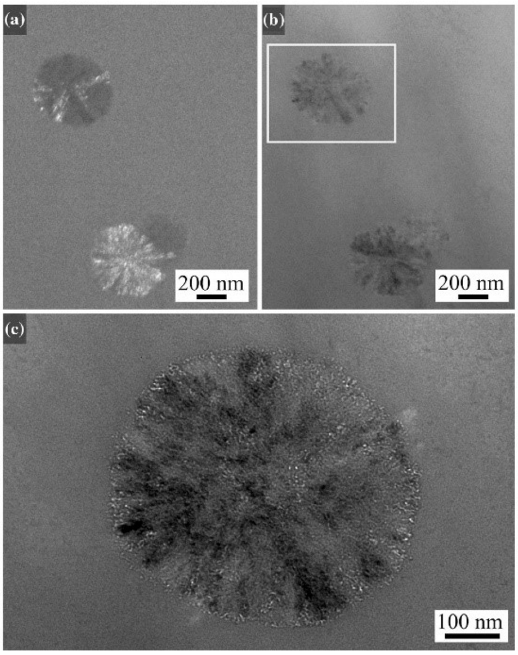

Figure 7 TEM micrographs of material C: **a** dark-field image, **b**, **c** bright-field image; the framed area in (**b**) is presented in (**c**) with a higher magnification.

network former. In some similar compositions, it has been proposed that a liquid–liquid phase separation by depletion of Ca and F occurs in the early stage of CaF_2 crystallization [49]. The structures observed in the TEM studies support this assumption. Both the oxidation to Ce^{4+} and the removal of CaF_2 lead to an increased network connectivity, which easily explains the increase in Tg.

All UV absorptions of the components Sb^{3+}, Sn^{2+}, Ag^{+} and Ce^{4+} occur at approximately the same wavelengths (<290 nm) and cannot be distinguished in the UV–Vis absorption spectra obtained at room temperature. The absorption maximum at 310 nm belongs to the 4f–5d transitions of Ce^{3+}. The change after irradiation below $\lambda < 350$ nm is due to an overlap of the Ce^{3+} peak with the charge transfer (CT) transitions of Ce^{3++} (see [35]). The irradiation induces a photoionization of Ce^{3+}, which leads to a reduction of Ag^{+} to Ag^{0}. The species denoted as Ce^{3++} is attributed to the valency state +4; however, the coordination shell of cerium should still be similar to that of Ce^{3+}, because higher temperature would be required to form new Ce–O bonds and re-arrange the Ce coordination [59].

The metallic Ag forms nanometer-sized clusters during the first thermal treatment step at 530 °C for 1 h, as shown in Fig. 2. However, the clusters shown in Fig. 2 are too large to be completely composed of Ag and most likely are liquid–liquid phase separations. The absorption peak at 428 nm in Fig. 1 is the characteristic plasmon resonance and causes the yellowish coloration of the material. The optical properties of Ag dramatically change if the metallic Ag particles are much smaller than the wavelength of visible light [60]. The extinction cross section

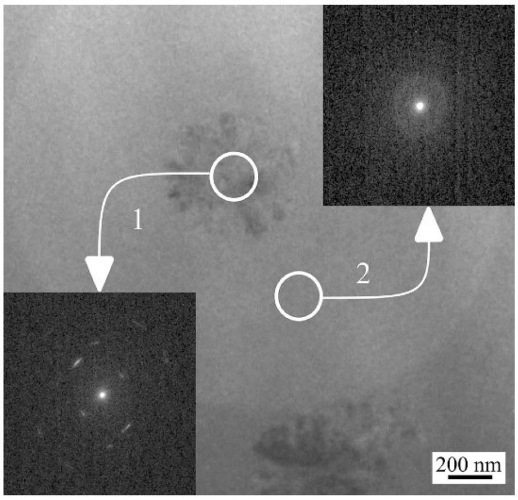

Figure 8 TEM micrograph of a nano particle and SAD patterns 1 and 2 acquired from the respective circled areas.

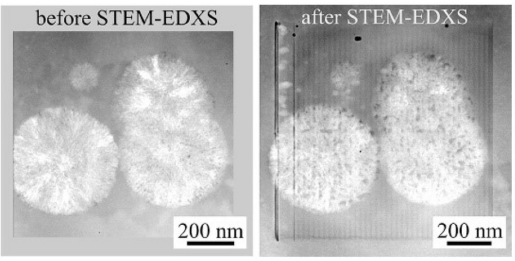

Figure 9 STEM micrographs of particles in material C before and after STEM-EDXS analysis.

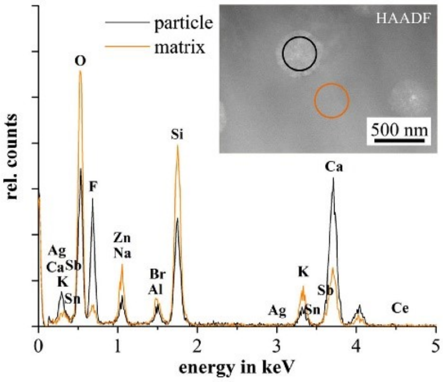

Figure 10 STEM micrograph of material C and respective EDXS spectra of one particle (*black*) and the matrix (*orange*).

corresponds to the interaction intensity of particle and light [61], and the optical cross section area may be larger than the true geometric size [52]. In general, the resulting optical behavior is affected by (i) the refractive index of the glass matrix, i.e., the surrounding medium, (ii) the particle size, (iii) the size distribution and (iv) the shape of the particles [62, 63]. The dispersion properties of the glass matrix have the dominant effect in most cases.

As expected for the behavior of small metal particles, the characteristic plasmon resonance wavelength increases with an increase in the particle size in the performed simulation. A plasmon resonance of 428 nm corresponds to an Ag particle diameter of 38 nm in a glass matrix as discussed above. In Fig. 2, a mean particle diameter of 35 nm was observed. If these structures consisted of pure Ag (impossible as outlined above), there would be a good agreement between the predicted and measured particle sizes. Furthermore, the broadness of the corresponding peak would be in agreement with a certain size distribution of the resonating domains. Previous studies showed that bromide is of major importance during the photoinduced crystallization process. The high refractive index of AgBr ($n = 2.2$) leads to a noticeable shift of the plasmon resonance toward higher wavelengths so that a AgBr shell of a few nm thickness would lead to a significant resonance wavelength shift, i.e., of up to several 10 nm according to Ref. [45]. It has been proposed that an AgBr shell forms around the clusters [45, 46]. In this study, the presence of AgBr could be neither proven by XRD nor confirmed by TEM imaging due to the sample damage. Moreover, the XRD pattern obtained after step 2 clearly shows diffraction peaks attributable to cubic CaF_2. In order to exclude a potential effect of surface crystallization and texture, the compact samples were repolished before XRD analysis so that any surface crystallized layer would be removed. CaF_2 has a fluorite structure, and the (111) peak should occur at $2\theta = 28.28°$ with a relative intensity of 95%. It is noteworthy that the (220) peak at 47.02° (100%) is of reduced intensity and the (311) peak at 55.78° (33%) is not observed in pattern C.

In the material C, the existence of CaF_2 crystals was confirmed by EBSD and TEM analysis. These crystals occur in the shape of numerous almost spherical particles with diameters up to 300 nm which cause a

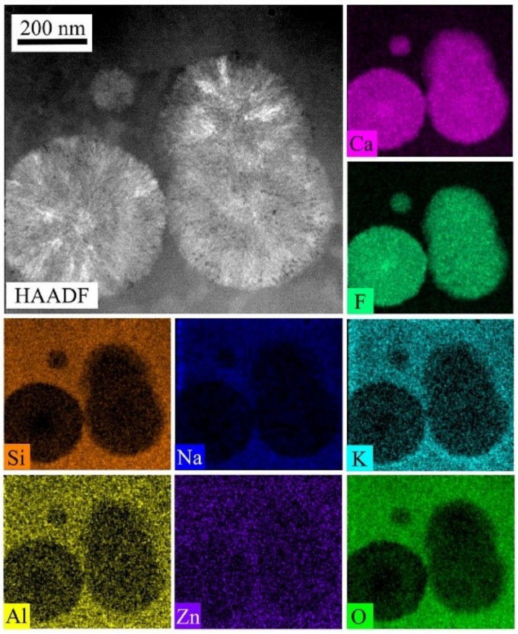

Figure 11 HAADF micrograph of material C as well as TEM–EDXS maps for Ca, F, Si, Na, K, Al, Zn and O in the presented area.

certain translucency of the material by scattering light. This is not a real problem for possible applications as, e.g., wavelengths in the near infrared, i.e., 1040 nm, are normally used for writing holograms. Some compact CaF_2 crystals allow the acquisition of higher-quality EBSD patterns; they are formed in agreement with Ref. [48], probably by homogeneous nucleation. Most particles, however, are not single crystals. Instead, they show a microstructure suggesting outward growth from a central point, see, e.g., Fig. 7. This is in agreement with the assumption that the clusters act as heterogeneous nucleation sites. The growth mechanism could hence be related to dendritic growth [64–66] or spherulites [67]. The mechanism similar to viscous fingering has also been proposed to occur in glasses [68].

The SAD pattern of zone 1 in Fig. 8 exhibits circular positioned elongated spots which arise from similarly oriented crystals and could indicate a spherulitic microstructure. By comparison, the SAD pattern of zone 2 shows the characteristic halo around the primary central beam confirming the amorphous matrix. The STEM-EDXS element distributions (Figs. 10, 11) of material C are in agreement with the expectations of CaF_2 crystals growing in a glass matrix. However, especially Si, Na, Al and O are also detected in small but not negligible concentrations inside the spheres. Hence, the intercrystalline spaces in the particles probably contain residual glass which would be in agreement with all three growth mechanisms mentioned above.

Conclusions

A photo-thermo-refractive (PTR) glass based on the system Na_2O–SiO_2–Al_2O_3–K_2O–CaO–CaF_2–ZnO and doped with Ce, Ag, Sn, Sb and Br was obtained by conventional glass melting techniques. The controlled crystallization of CaF_2 from this glass was investigated by various electron microscopy techniques and is summarized as follows:

1. In the nucleation stage (first heat treatment), the silver atoms cluster and agglomerations ~35 nm in diameter were observed after UV exposure and first heat treatment. A calculation of the plasmon resonance of Ag nanoparticles shows that the structures found in the TEM images would match the optical band at 428 nm shown in the optical spectra if they were composed of pure metallic Ag. The formation of a shell of AgBr with a high refractive index around the Ag cluster would lead to a characteristic plasmon resonance shift to higher wavelengths but the presence of AgBr could neither be proved by XRD nor be confirmed by TEM.
2. In the crystallization stage (second heat treatment), CaF_2 nanocrystals with diameters up to ca. 300 nm are formed and are homogeneously distributed in the glass matrix. We observed that the CaF_2 crystals show an inhomogeneous microstructure. Each particular crystal seems to be oriented from a central point to the interface crystal/glass. Intercrystalline spaces between the particular crystals contain a residual glassy phase.

The translucency of the material is not a real problem for possible applications as, e.g., wavelengths in the near infrared, i.e., 1040 nm, are normally used for writing holograms. The occurrence of phase separation has a mandatory effect on the crystallization behavior and needs to be investigated in detail because this could cause undesired scattering effects and might lead to problems during the volume phase hologram recording process.

Acknowledgements

This work was funded by the Bundesministerium für Bildung und Forschung, Germany (Wachstumskern Brightlas, 03WKCF3E).

Compliance with ethical standards

Conflict of interest The authors declare that they have no conflict of interest.

References

[1] Lumeau JL, Zanotto ED (2016) A Review of the photo-thermal mechanism and crystallization of photo-thermo-refractive (PTR) glass. Int Mater Rev. doi:10.1080/09506608.2016.1264132

[2] Klimov M, Glebov L, Glebova L (2016) Differentiation of crystalline and amorphous phases in photothermorefractive glass by secondary ion mass spectrometry. J Vac Sci Technol B 34:03H118

[3] Lumeau J, Chamma K, Glebova L, Glebov LB (2014) X-ray diffraction study of NaF nano-crystals in photo-thermo-refractive glass. J Non Cryst Solids 405:188–195

[4] Borgman VA, Glebov LB, Nikonorov NV, Petrovskii GT, Savvin VV, Tsvetkov AD (1989) Photothermorefractive effect in silicate-glasses. Dokl Akad Nauk Sssr 309:336–339

[5] Nikonorov NV, Panysheva EI, Tunimanova IV, Chukharev AV (2001) Influence of glass composition on the refractive index change upon photothermoinduced crystallization. Glass Phys Chem 27:241–249

[6] Efimov OM, Glebov LB, Smirnov VI (2000) High-frequency Bragg gratings in a photothermorefractive glass. Opt Lett 25:1693–1695

[7] Ciapurin IV, Glebov LB, Smirnov VI (2006) Modeling of phase volume diffractive gratings, part 1: transmitting sinusoidal uniform gratings. Opt Eng 45(1):015802

[8] Smirnov VI, Lumeau J, Mokhov S, Zeldovich BY, Glebov LB (2010) Ultranarrow bandwidth moire reflecting Bragg gratings recorded in photo-thermo-refractive glass. Opt Lett 35(4):592–594

[9] Andrusyak O, Canioni L, Cohanoschi I, Rotari E, Smirnov VI, Venus G et al (2009) Cross-correlation technique for dispersion characterization of chirped volume Bragg gratings. Appl Optics 48(30):5786–5792

[10] SeGall M, Rotar V, Lumeau J, Mokhov S, Zeldovich BY, Glebov LB (2012) Binary volume phase masks in photo-thermo-refractive glass. Opt Lett 37(7):1190–1192

[11] Paboeuf D, Vijayakumar D, Jensen OB, Thestrup B, Lim J, Sujecki S et al (2011) Volume Bragg grating external cavities for the passive phase locking of high-brightness diode laser arrays: theoretical and experimental study. J Opt Soc Am B 28(5):1289–1299

[12] Drachenberg DR, Andrusyak O, Venus G, Smirnov VI, Lumeau J, Glebov LB (2013) Ultimate efficiency of spectral beam combining by volume Bragg gratings. Appl Optics 52(30):7233–7242

[13] Andrusyak O, Smirnov VI, Venus G, Glebov LB (2009) Beam combining of lasers with high spectral density using volume Bragg gratings. Opt Commun 282(13):2560–2563

[14] Glebov LB, Smirnov VI, Rotari E, Cohanoschi I, Glebova L, Smolski O et al (2014) Volume-chirped Bragg gratings: monolithic components for stretching and compression of ultrashort laser pulses. Opt Eng 53(5):051514

[15] Stoica M, de Macedo GNBM, Rüssel C (2014) Photo induced crystallization of CaF_2 from a $Na_2O/K_2O/CaO/CaF_2/Al_2O_3/SiO_2$ glass. Opt Mater Express 4:1574–1585

[16] Rüssel C (2005) Nanocrystallization of CaF_2 from $Na_2O/K_2O/CaO/CaF_2/Al_2O_3/SiO_2$ glasses. Chem Mater 17:5843–5847

[17] Bocker C, Rüssel C, Avramov I (2013) Transparent nano crystalline glass-ceramics by interface controlled crystallization. Int J Appl Glass Sci 4:174–181

[18] Woltz S, Rüssel C (2004) Self organized nano crystallinity of magnetite precipitated from a $4.9Na_2O$ $33.3CaO$ 17.1 Fe_2O_3 $44.7B_2O_3$ glass. J Non Cryst Solids 337:226–231

[19] Harizanova R, Gugov I, Rüssel C, Tatchev D, Raghuwanshi VS, Hoell A (2011) Crystallization of (Fe, Mn)-based nanoparticles in sodium-silicate glasses. J Mater Sci 46:7169–7176. doi:10.1007/s10853-011-5840-x

[20] Harizanova R, Volksch G, Rüssel C (2011) Crystallization and microstructure of glasses in the system $Na_2O/MnO/SiO_2/Fe_2O_3$. Mater Res Bull 46:81–86

[21] Bocker C, Bhattacharyya S, Höche T, Rüssel C (2009) Size distribution of BaF_2 nanocrystallites in transparent glass ceramics. Acta Mater 57:5956–5963

[22] Bocker C, Rüssel C (2009) Self-organized nano-crystallisation of BaF_2 from $Na_2O/K_2O/BaF_2/Al_2O_3/SiO_2$ glasses. J Eur Ceram Soc 29:1221–1225

[23] Raghuwanshi VS, Hoell A, Bocker C, Rüssel C (2012) Experimental evidence of a diffusion barrier around BaF_2 nanocrystals in a silicate glass system by ASAXS. Crystengcom 14:5215–5223

[24] Bhattacharyya S, Bocker C, Heil T, Jinschek JR, Höche T, Rüssel C, Kohl H (2009) Experimental evidence of self-

limited growth of nanocrystals in glass. Nano Lett 9:2493–2496

[25] Bocker C, Avramov I, Rüssel C (2010) Viscosity and diffusion of barium and fluoride in $Na_2O/K_2O/Al_2O_3/SiO_2/BaF_2$ glasses. Chem Phys 369:96–100

[26] Bocker C, Wiemert J, Rüssel C (2014) The effect of viscosity on nanocrystallization of strontium fluoride from a silicate glass. Solid State Sci 30:55–60

[27] Bocker C, Wiemert J, Rüssel C (2013) The formation of strontium fluoride nano crystals from a phase separated silicate glass. J Eur Ceram Soc 33:1737–1745

[28] de Pablos-Martin A, Mather GC, Munoz F, Bhattacharyya S, Höche T, Jinschek JR, Heil T, Duran A, Pascual MJ (2010) Design of oxy-fluoride glass-ceramics containing $NaLaF_4$ nano-crystals. J Non Cryst Solids 356:3071–3079

[29] Hemono N, Pierre G, Munoz F, de Pablos-Martin A, Pascual MJ, Duran A (2009) Processing of transparent glass-ceramics by nanocrystallisation of LaF_3. J Eur Ceram Soc 29:2915–2920

[30] Bhattacharyya S, Höche T, Hemono N, Pascual MJ, van Aken PA (2009) Nano-crystallization in LaF_3–Na_2O–Al_2O_3–SiO_2 glass. J Cryst Growth 311:4350–4355

[31] Herrmann A, Tylkowski M, Bocker C, Rüssel C (2013) Cubic and hexagonal $NaGdF_4$ crystals precipitated from an aluminosilicate glass: preparation and luminescence properties. Chem Mater 25:2878–2884

[32] Herrmann A, Tylkowski M, Bocker C, Rüssel C (2013) Preparation and luminescence properties of glass-ceramics containing Sm^{3+}-doped hexagonal $NaGdF_4$ crystals. J Mater Sci 48:6262–6268. doi:10.1007/s10853-013-7423-5

[33] de Almeida RPF, Bocker C, Rüssel C (2008) Size of CaF_2 crystals precipitated from glasses in the $Na_2O/K_2O/CaO/CaF_2/Al_2O_3/SiO_2$ system and percolation theory. Chem Mater 20:5916–5921

[34] Hoell A, Varga Z, Raghuwanshi VS, Krumrey M, Bocker C, Rüssel C (2014) ASAXS study of CaF_2 nanoparticles embedded in a silicate glass matrix. J Appl Crystallogr 47:60–66

[35] Stoica M, Herrmann A, Hein J, Rüssel C (2016) UV-vis spectroscopic studies of a CaF_2 photo-thermo-refractive glass. Opt Mater 62:424–432

[36] Magon CJ, Gonzalez JPD, Lima JF, Eckert H, Zanotto ED, Lumeau J, Glebova L, Glebov L (2016) Paramagnetic resonance (EPR) studies on the photo-thermo ionization process of photo-thermo-refractive glasses. J Non Cryst Solids 452:320–324

[37] Ivanov SA, Nikonorov NV, Ignatiev AI (2015) In: Proceedings of the 3rd international conference on photonics, optics and laser technology

[38] Mortier M (2002) Between glass and crystal: glass-ceramics, a new way for optical materials. Philos Mag B 82:745–753

[39] Glebov LB (2007) Photosensitive holographic glass—new approach to creation of high power lasers. Phys Chem Glass B 48:123–128

[40] Hofmann P, Amezcua-Correa R, Antonio-Lopez E, Ott D, SeGall M, Divliansky I, Lumeau J, Glebova L, Glebov L, Peyghambarian N, Schulzgen A (2013) Strong Bragg gratings in highly photosensitive photo-thermo-refractive-glass optical fiber. IEEE Photonic Tech L 25:25–28

[41] Souza GP, Fokin VM, Rodrigues CF, Rodrigues ACM, Zanotto ED, Lumeau J, Glebova L, Glebov LB (2011) Liquid-liquid phase separation in photo-thermo-refractive glass. J Am Ceram Soc 94:86–91

[42] Souza GP, Fokin VM, Baptista CA, Zanotto ED, Lumeau J, Glebova L, Glebov LB (2011) Effect of bromine on NaF crystallization in photo-thermo-refractive glass. J Am Ceram Soc 94:2906–2911

[43] Fokin VM, Souza GP, Zanotto ED, Lumeau J, Glebova L, Glebov LB (2010) Sodium fluoride solubility and crystallization in photo-thermo-refractive glass. J Am Ceram Soc 93:716–721

[44] Glebova L, Lumeau J, Klimov M, Zanotto ED, Glebov LB (2008) Influence of UV-exposure on the crystallization and optical properties of photo-thermo-refractive glass. J Non Cryst Solids 354:456–461

[45] Nikonorov NV, Sidorov AI, Tsekhomskii VA, Lazareva KE (2009) Effect of a dielectric shell of a silver nanoparticle on the spectral position of the plasmon resonance of the nanoparticle in photochromic glass. Opt Spectrosc 107:705–707

[46] Aseev VA, Burdaev PA, Kolobkova EV, Nikonorov NV (2012) Fluorophosphate glasses activated by rare-earth ions and AgBr glass. Phys Chem 38:366–372

[47] Barry TI, Clinton DJ, Wilson AD (1979) Structure of a glass-ionomer cement and its relationship to the setting. Process J Dent Res 58:1072–1079

[48] Hill RG, Goat C, Wood D (1992) Thermal-analysis of a SiO_2–Al_2O_3–CaO–CaF_2 glass. J Am Ceram Soc 75:778–785

[49] Deng W, Gong YX, Cheng JS (2014) Liquid-phase separation and crystallization of high silicon canasite-based glass ceramic. J Non Cryst Solids 385:47–54

[50] Wemple SH (1973) Refractive-index behavior of amorphous semiconductors and glasses. Phys Rev B 7:3767–3777

[51] Laven P (2004) Simulation of rainbows, coronas and glories using Mie theory and the Debye series. J Quant Spectrosc Ra 89:257–269

[52] Bohren CF, Huffman DR (1983) Absorption and scattering of light by small particles. Wiley, New York

[53] Johnson PB, Christy RW (1972) Optical constants of noble metals. Phys Rev B 6:4370–4379

[54] Stroud JS (1962) Color centers in a cerium-containing silicate glass. J Chem Phys 37:836–841

[55] Efimov AM, Ignatiev AI, Nikonorov NV, Postnikov ES (2013) Quantitative UV-VIS spectroscopic studies of photo-thermo-refractive glasses. II. Manifestations of Ce^{3+} and Ce(IV) valence states in the UV absorption spectrum of cerium-doped photo-thermo-refractive matrix glasses. J Non Cryst Solids 361:26–37

[56] Sgibnev EM, Ignatiev AI, Nikonorov NV, Efimov AM, Postnikov ES (2013) Effects of silver ion exchange and subsequent treatments on the UV-VIS spectra of silicate glasses. I. Undoped, CeO_2-doped, and ($CeO_2 + Sb_2O_3$)-codoped photo-thermo-refractive matrix glasses. J Non Cryst Solids 378:213–226

[57] Ehrt D (2008) Redox behaviour of Sn^{4+}/Sn^{2+} in alkali free aluminosilicate glasses and melts. Phys Chem Glass B 49:68–72

[58] Kreibig U, Zacharias P (1970) Surface plasma resonances in small spherical silver and gold particles. Z Phys 231:128–143

[59] Kido L, Müller M, Rüssel C (2012) The effect of viscosity on the kinetics of redox reactions in highly viscous silicate liquids. J Chem Phys 136:224502

[60] Mie G (1908) Beiträge zur Optik trüber Medien, speziell kolloidaler Metalllösungen. Ann Phys 330:377–445

[61] Kelly KL, Coronado E, Zhao LL, Schatz GC (2003) The optical properties of metal nanoparticles: the influence of size, shape, and dielectric environment. J Phys Chem B 107:668–677

[62] Worsch C, Kracker M, Wisniewski W, Rüssel C (2012) Optical properties of self assembled oriented island evolution of ultra-thin gold layers. Thin Solid Films 520:4941–4946

[63] Garcia MA (2011) Surface plasmons in metallic nanoparticles: fundamentals and applications. J. Phys. D Appl Phys 44:283001

[64] Granasy L, Pusztai T, Borzsonyi T, Warren JA, Douglas JF (2004) A general mechanism of polycrystalline growth. Nat Mater 3:645–650

[65] Granasy L, Pusztai T, Warren JA, Douglas JF, Borzsonyi T, Ferreiro V (2003) Growth of 'dizzy dendrites' in a random field of foreign particles. Nat Mater 2:92–96

[66] Souza GP, Fokin VM, Zanotto ED, Lumeau J, Glebova L, Glebov LB (2009) Micro and nanostructures in partially crystallised photothermorefractive glass. Phys Chem Glass B 50:311–320

[67] Shtukenberg AG, Punin YO, Gunn E, Kahr B (2012) Spherulites Chem Rev 112:1805–1838

[68] Wisniewski W, Patschger M, Rüssel C (2013) Viscous fingering and dendritic growth of surface crystallized $Sr_2TiSi_2O_8$ fresnoite. Sci Rep 3:3558

Article 3.4

M. Stoica, M. Brehl, C. Bocker, A. Herrmann, C. Rüssel

Microstructure and Luminescence of Erbium doped $Na_2O/K_2O/CaO/CaF_2/Al_2O_3/SiO_2$ Nano Glass-ceramics

Materials Chemistry & Physics **2018** 207:36-43

DOI: 10.1016/j.matchemphys.2017.12.032

Microstructure and Luminescence of Erbium doped $Na_2O/K_2O/CaO/CaF_2/Al_2O_3/SiO_2$ Nano Glass-ceramics					
Beteiligt an					
	Martina Stoica	Martin Brehl	Dr. Christian Bocker	Dr. Andreas Herrmann	Prof. Christian Rüssel
Konzeption des Forschungsansatzes	X				X
Planung der Untersuchung	X		X		
Datenerhebung	X	X	X	X	
Datenanalyse und Interpretation	X	X	X	X	
Schreiben des Manuskripts	X		X	X	X
Vorschlag Anrechnung Publikationsäquivalente	1,0				

Materials Chemistry and Physics 207 (2018) 36–43

Contents lists available at ScienceDirect

Materials Chemistry and Physics

journal homepage: www.elsevier.com/locate/matchemphys

Microstructure and luminescence of erbiumdoped $Na_2O/K_2O/CaO/CaF_2/Al_2O_3/SiO_2$ nano glass-ceramics

Martina Stoica*, Martin Brehl, Christian Bocker, Andreas Herrmann, Christian Rüssel

Otto-Schott-Institut, Jena University, Fraunhoferstr. 6, 07743 Jena, Germany

HIGHLIGHTS

- Glasses within the system $Na_2O/K_2O/CaO/CaF_2/Al_2O_3/SiO_2$ show phase separation.
- Tendency to phase separation increases with Al_2O_3 concentration.
- CaF_2 nanocrystals are formed inside the fluoride rich droplets during annealing.
- The crystallization temperature decreases with increasing Al_2O_3 concentration.
- Doping with Er^{3+} triggers CaF_2 nano crystallization.

ARTICLE INFO

Article history:

Keywords:
Luminescence
Electron microscopy
Nanocrystals
Erbium
Oxyfluoride glass

ABSTRACT

Oxyfluoride glasses with the mol% compositions (63-*x*) SiO_2, *x* Al_2O_3, 12.3 CaO, 5.3 K_2O, 9.0 Na_2O and 10.4 CaF_2 with $x = (10, 8, 6)$ were doped with an Er^{3+}-concentration of $1 \cdot 10^{20}\,cm^{-3}$. The glasses were thermally treated at temperatures in the range from 550 to 620 °C. This led to the crystallization of cubic CaF_2 with extremely broadened XRD-lines caused by mean crystallite sizes ranging from 14 to 38 nm. An interface controlled crystallization mechanism is proposed. Phase separation was observed in the as casted glasses by electron microscopy. Droplet like particles occur with a size of ca. 360 nm after heat treatment. These particles are composed by small crystallites with sizes of around 50 nm. Increasing Al_2O_3 concentration increases the tendency to liquid/liquid phase separation and decreases the crystallization temperature. Doping with Er^{3+} triggers CaF_2 nanocrystallization by decreasing the crystallization temperature.

1. Introduction

Glass-ceramics with crystallites with sizes in the nanometer scale are appropriate materials for photonic applications due to their low scattering and absorption effects [1]. From oxyfluoride glasses, which are usually multicomponent systems, nanocrystals can be precipitated during thermal treatment. The nanocrystals grow in the glass matrix via an interface controlled crystallization mechanism which restricts the crystal sizes to a few nanometers with a narrow size distribution [2]. This was reported for a series of alkaline earth and rare earth fluorides (BaF_2 [3–6], CaF_2 [7,8], SrF_2 [9,10], LaF_3 [11,12], $NaLaF_4$ [13], $NaGdF_4$ [14] and PbF_2 [15]). During the crystallization process, the glassy phase near the growing crystal is depleted in those components which form the crystal and therefore is enriched in Si and Al. This results in the formation of a diffusion profile due to the local changes of the element concentrations. Near the crystal, the viscosity strongly increases due to the Si and Al enrichment and the diffusion coefficients strongly decrease during the course of the crystallization until diffusion is stopped and crystal growth is frozen [3,6,8]. Furthermore, liquid/liquid phase separation might occur where droplets enriched in network modifiers, for instance fluoride, are formed in an SiO_2 enriched glass matrix. Nucleation of the crystals occurs inside the droplet phase. Then, the growth of the crystals is additionally limited by the size of the droplets [2].

Oxyfluoride glass-ceramics may combine the advantages of aluminosilicate matrices and the optical features of low phonon fluoride crystals which can be activated by the incorporation of rare earth ions [16–18]. These materials are characterized by a narrow phonon spectrum, high luminescence quantum yields and long lifetimes of the excited state, i.e. fluorescence lifetimes.

---

* Corresponding author.
E-mail address: martina.stoica@gmx.de (M. Stoica).

https://doi.org/10.1016/j.matchemphys.2017.12.032

Fluorescence lifetimes of rare earth ions depend on their incorporation, e.g. coordination numbers, and the phonon energy. The phonon energy is reduced by less tightly bound atoms in a crystal structure. Thus the lifetime of the excited state should increase [19]. In pure fluoride glasses, i.e. glasses in which fluorine is the only anionic species, the phonon energy is low [20], however, these materials have several serious disadvantages: the high expenditure for the fabrication and the poor mechanical and chemical stability as well as their high tendency towards crystallization. By contrast, the oxyfluoride glass-ceramics are considerably easier to produce, provide properties similar to fluoride single crystals and the mechanical properties are governed by the surrounding glass matrix [21]. Hence, a different venue in the area of potential luminescence and laser materials is opened.

In the past few years, a number of oxyfluoride glass-ceramics with different rare earth ions incorporated into the fluoride crystals were studied and their optical properties were reported [22]. The first question, which needs to be clarified, is whether the rare earth ions are quantitatively incorporated in the crystal phase or, however, remain preferably in the residual glassy phase. The intensity and shape of luminescence spectra of the doped glass-ceramics in comparison with the undoped are frequently used to conclude on the incorporation of the rare earth ions [23–26]. Enhanced fluorescence lifetimes and/or intensities are only supposed for those ions incorporated into the crystal phase. The fluorescence lifetime in Er^{3+} doped glass-ceramics is strongly increased compared to the glasses due to the lower phonon energy of the fluoride nanocrystals surrounding the Er^{3+} ions [24]. For Dy^{3+} doped oxyfluoride glasses and glass ceramics, the proportion of Dy^{3+} ions in the fluoride-type nanocrystals increases with concentration and with duration of the thermal treatment [26]. The splitting of peaks could be another indication of a crystal environment [27,28]. On the other hand, changes in the microstructure, i.e. turbidity, bubbles or liquid/liquid phase separation (LLPS) might also cause an increase in luminescence intensity due to increased light scattering and an enhanced excitation within the sample [29], since fluorescence measurements are performed integral over a macroscopic area and therefore show a superposition of luminescence contributions of all phases and different local rare earth sites.

Oxyfluoride glass-ceramics of similar chemical composition can be used to prepare photo-thermo-refractive glasses [30,31]. By doping with photosensitizers (Ce, Ag), local refractive index changes ($\Delta n \sim 10^{-4}$) can be generated by a photoinduced crystallization process due to the precipitation of CaF_2 [32].

This study is based on the glass system $Na_2O/K_2O/CaO/CaF_2/Al_2O_3/SiO_2$. Glass-ceramics of this composition show high transparency [7], are non-toxic and have a high solubility for rare earth ions [22]. An indication for the incorporation of rare earth ions into the CaF_2 host lattice is the change in the lattice parameter, which is increased after heat treatment by the incorporation of Er^{3+} [33,34]. Doping oxyfluoride glasses with rare earth ions can also lead to the occurrence of phase separation and can significantly affect the crystallization [35–37].

In this paper, the effect of Er^{3+} on the crystallization of CaF_2 from glasses in the system $Na_2O/K_2O/CaO/CaF_2/Al_2O_3/SiO_2$ is described. The effect of Al_2O_3 on the resulting phase formation and microstructure is described as well as the effect of temperature and the Er^{3+} concentration.

2. Materials and methods

Glasses with the mol% composition (63-x) SiO_2, x Al_2O_3, 12.3 CaO, 5.3 K_2O, 9.0 Na_2O, 10.4 CaF_2 with $x = (10, 8, 6)$ were melted from reagent grade raw materials $Al(OH)_3$, $CaCO_3$, K_2CO_3, Na_2CO_3, SiO_2 (quartz) and CaF_2 in batches of 200 g using a platinum crucible in an induction furnace at 1480 °C. The rare earth doping of 1×10^{20} cm^{-3} Er^{3+} was added to the batch as Er_2O_3 which corresponds to about 0.2 mol% Er_2O_3 in the glass (see Table 1). The fining procedure was carried out for 120 min. The melt was homogenized with a Pt stirrer for 60 min at 1420 °C. Then, the glass melt was cast in a preheated (560 °C) steel mould and placed in a preheated furnace where the glass slowly cooled to room temperature (cooling rate: approximately 2 K/min).

The samples were thermally treated at temperatures in the range from 560 to 620 °C for 1–80 h. In order to reduce the error induced by the heating rate, especially at short annealing times, the samples were placed into the preheated furnace (at the desired temperature). After the respective crystallization time, the furnace was switched off and allowed to cool.

Powdered samples from the grain-size fraction 250–315 µm were studied by differential thermal analysis (DTA 50, Shimadzu, Japan) as well as by differential scanning calorimetry (DSC 822, Mettler Toledo GmbH, Greifensee, Swizzerland) with a heating rate of 10 K/min to obtain values for the glass transition temperature, T_g and the crystallization temperature, T_c.

XRD patterns were recorded from thermally treated and subsequently powdered samples using a D 5000 X-ray diffractometer, (Bruker AXS GmbH, Karlsruhe, Germany) with $Cu_{K\alpha}$ radiation ($\lambda_{CuK\alpha 1} = 1.54$ Å) and θ-2θ geometry. From the peak broadening in the XRD profiles, the average crystallite size d was estimated using Scherrer's equation [38]:

$$d = \frac{G \cdot \lambda}{B \cdot \cos\theta} \tag{1}$$

where G = 0.899 for a cubic crystal, λ is the used wavelength (= 0.154 nm), B is the full width at half maximum (FWHM), and θ is the Bragg angle of the respective XRD peak. The peak broadening caused by the instrumentation was taken into account by measuring the FWHM of a silicon single crystal with the same equipment and subtracting the value from the FWHM of the respective samples.

A scanning electron microscope (SEM; JSM7001F, Jeol Ltd., Tokyo, Japan) was used. For imaging, the samples were etched for 10–20 s, using diluted hydrofluoric acid (HF, 5%) and in order to avoid surface charging, they were subsequently coated with carbon (Auto 306; Edwards, Crawley, UK) by evaporation in high vacuum (10^{-3} Pa). A transmission electron microscope (TEM; H8100, Hitachi High-Tech, Tokyo, Japan) at 200 kV was used additionally.

Fluorescence spectra were collected using a spectrometer (RF-5301 PC, Shimadzu, Japan) at wavelengths in the range from 220 to 900 nm with a resolution of 0.2 nm. The analyzed samples were 10 mm thick and were polished at both sides. The emission spectra were measured with an excitation wavelength of around 520 nm and the excitation spectra at an emission wavelength around 545 nm depending on sample composition.

3. Results

The as poured glass with the composition A is completely

Table 1
The glass composition in mol% of the prepared samples.

Sample	SiO_2	Al_2O_3	CaO	K_2O	Na_2O	CaF_2	Er_2O_3
A	53	10	12.3	5.3	9	10.4	
B	55	8	12.3	5.3	9	10.4	
C	57	6	12.3	5.3	9	10.4	
B_Er	54.78	7.97	12.25	5.28	8.96	10.36	0.2
C_Er	56.77	5.98	12.25	5.28	8.96	10.36	0.2

opaque. Therefore, this composition was not considered for further studies. Sample B is transparent but slightly turbid. Sample C is clear and visually transparent. Doping with Er^{3+} (sample B_Er and C_Er) results in the typical pink colour of the glasses while it does not affect the turbidity of the samples. The fluorine loss was determined by energy-dispersive X-ray (EDX) spectrometry, amounting to an average of 30% ± 3% for all glasses.

Fig. 1 shows samples with a thickness of 10 mm crystallized at different temperatures. After thermal treatment at increasing temperatures, the transparency of the samples decreases and their opacity increased. This effect is observed for all studied compositions.

The results of the thermal analyses of the as poured glasses of samples A, B/B_Er and C/C_Er are summarized in Table 2.

The glass transition temperatures determined using DSC and dilatometry are in agreement within the limits of error (±5 K) with each other for the same glass composition. With decreasing aluminum concentration, the dilatometric softening point T_d decreases from 627 to 591 °C while the thermal expansion coefficient α increases from 10.4 to 12.0 $10^{-6}\,K^{-1}$. Furthermore, the crystallization temperature T_c (first exothermic peak in the DSC curve) increases from 685 to 775 °C with decreasing aluminum concentration. The sample A shows several exothermic peaks at higher temperatures.

Fig. 2 shows the glass transition temperatures (T_g) measured by DSC from heat treated samples as a function of the heat treatment time at 580 °C. If crystallization occurred during heat treatment, the determined T_g is attributed to the residual glassy phase. In all the samples which were crystallized at 580 °C for different periods of time, a T_g drop of around 10 K occurred after crystallizing the glasses for 1 h (see inset of Fig. 2). With increasing time of thermal treatment, T_g increases and finally reaches nearly the supplied temperature of thermal treatment. The doping with erbium does not affect T_g of the residual glassy phase in the partially crystallized samples.

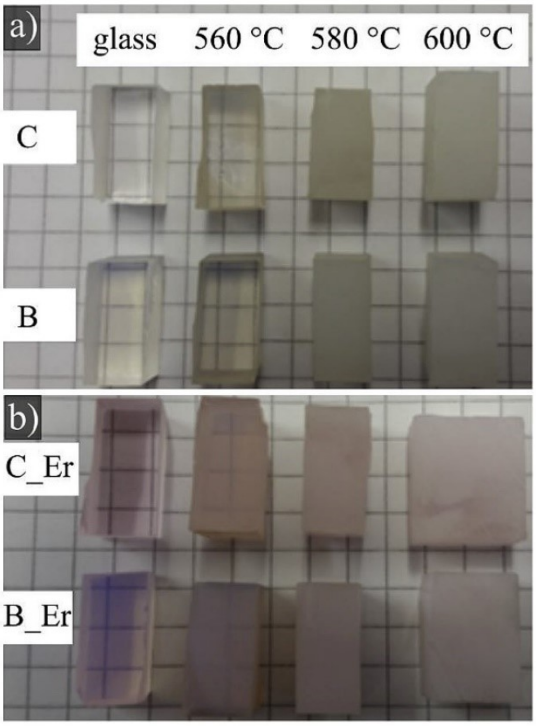

Fig. 1. Images of glasses and glass-ceramics with different chemical compositions (see Table 1), heat treated at different temperatures for 20 h, a) undoped b) doped with $1{\cdot}10^{20}\,cm^{-3}$ Er^{3+}.

Table 2
Thermal characterization of the as casted glasses.

Sample	DSC		Dilatometry		
	T_g [°C]	T_c [°C]	T_g [°C]	T_d [°C]	α [$10^{-6}\,K^{-1}$]
A	555	685 (720, 870)			
B	545	715	548	600	10.7
B_Er	545	715	541	627	10.4
C	547	775	542	594	11.3
C_Er	546	775	546	591	12.0

Glass transition temperature T_g, temperature of the crystallization peak T_c, dilatometric softening point T_d and coefficient of thermal expansion α.

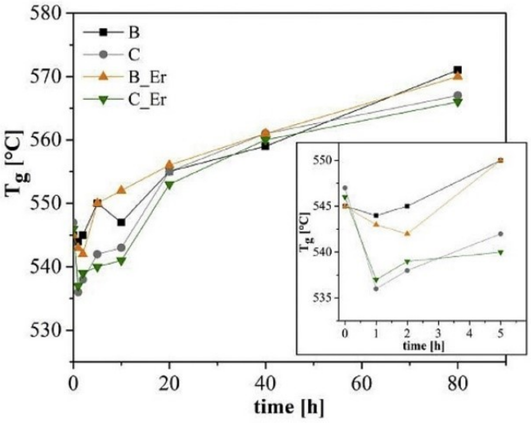

Fig. 2. Glass transition temperature T_g measured by DSC as a function of heat treatment time for the samples B/B_Er and C/C_Er annealed at 580 °C.

Fig. 3 shows X-ray diffraction pattern of an untreated sample C

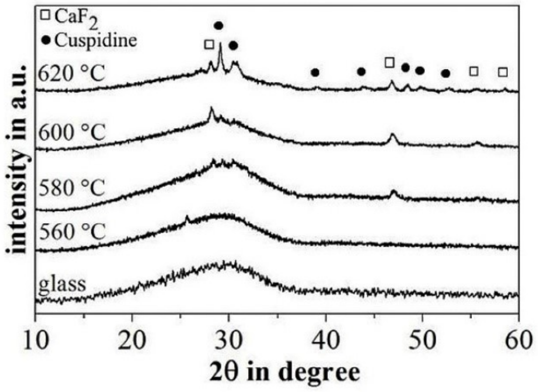

Fig. 3. XRD patterns of samples C, as casted glass and samples heat treated for 20 h at different temperatures (560–620 °C).

and samples C thermally treated at different temperatures for 20 h. The X-ray diffraction patterns of the as casted glasses of the undoped sample C and B (not shown) do not show diffraction peaks and should therefore be amorphous.

After heat treatment at 580 °C, peaks at $2\theta = 28.3°$ and 47.0° appear, which can be attributed to cubic CaF_2 crystals (JCPDS 35–0816). At higher heat treatment temperatures, additional peaks are observed at $2\theta = 55.8°$ and 58.6° related to cubic CaF_2 and several peaks that might be attributed to a second crystal phase, cuspidine $Ca_4Si_2O_7(F, OH)_2$ (JCPDS 76–0624). In sample B, this phase already appears after heat treatment at 600 °C (not shown), while for sample C, a temperature of 620 °C is necessary.

Fig. 4 shows the XRD pattern of sample C heat treated at 580 °C for longer periods of time. After 2 h, no peaks appear, while after 20 h, broadened peaks at $2\theta = 28.3°$ and 47.0° attributed to CaF_2 occur. Longer annealing times do not change the shape of the CaF_2 peaks. After 80 h of heat treatment, peaks at $2\theta = 29.1°$and 30.5° appear, attributed to cuspidine. Sample B shows the crystallization of cuspidine already after 40 h annealing time while the XRD pattern remains nearly the same for 80 h (not shown).

If the samples are doped with erbium, the overall crystallization trend observed from XRD does not change, i.e. with increasing temperature and time, the crystallization of CaF_2 occurs first and then, cuspidine is formed while the crystallization and the peak shape does not notably change with time. However, it should be noted, that the crystallization of CaF_2 is observed at lower temperatures in the case of the Er^{3+} doped samples. In sample C_Er and B_Er, CaF_2 peaks appear already after 20 h at 560 °C (not shown).

The sizes of the precipitated CaF_2 crystals were calculated for samples B, B_Er, C and C_Er by fitting a Gaussian function to the peak at around $2\theta = 47°$ and using Eq. (1). These results are shown in Table 3. The errors given in parenthesis result from fitting and the instruments step size.

The crystallite sizes are 10–38 nm and there is no clear trend in crystallite size with increasing temperatures from 560 to 620 °C or annealing times from 20 to 80 h at 580 °C. It is seen that with decreasing Al-concentration, from sample B to sample C, the crystallite size decreases slightly. Erbium doped samples already show CaF_2 crystals at 560 °C with sizes of 14 and 10 nm in samples B_Er and C_Er, respectively.

Fig. 5 shows SEM micrographs of the etched surface of sample C without thermal treatment (a) and of samples C (b) and C_Er (c) heat treated at 560 °C for 20 h. Sample C without thermal treatment (Fig. 5a) shows heterogeneities with sizes of approximately 100 nm, which are evidence for liquid/liquid phase separation since the sample is X-ray amorphous. In the thermally treated samples (Fig. 5b, c), homogeneously distributed spherical particles with diameters of 220–360 nm are observed and a larger number of smaller particles with a size around 50 nm can be noticed which are better visible in (Fig. 5 c) for the Er^{3+} doped sample.

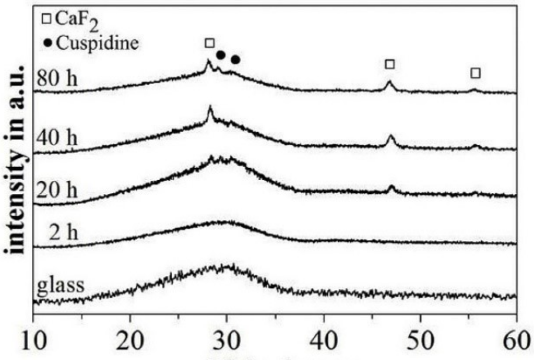

Fig. 4. XRD patterns of sample C, untreated and heat treated at 580 °C for 2–80 h.

Table 3
Mean crystallites size of undoped and Er^{3+}-doped samples, heat treated at different temperatures and times, (absolute error in parenthesis).

Temperature [°C]	Mean crystallite size [nm]				
	Time [h]	B	B_Er	C	C_Er
560	20	–	14 (1)	–	10 (3)
580	20	19 (4)	26 (3)	16 (2)	28 (4)
580	40	17 (3)	18 (2)	14 (1)	14 (1)
580	80	16 (4)	33 (4)	14 (1)	12 (1)
600	20	17 (4)	31 (3)	14 (1)	14 (1)
620	20	38 (4)	29 (3)	22 (3)	23 (4)

Fig. 6 shows a TEM bright field micrograph of sample C_Er heat treated at 560 °C for 20 h. This is in good agreement with the SEM micrographs in Fig. 5: large particles with diameters from 300 to 500 nm occur. However, smaller particles with diameters of 50 nm as expected from SEM are not observed. Some particles seem to be frayed, i.e. the edges are frayed. This indicates either electron beam damage and/or ion beam damage during sample preparation. Both may lead to a decomposition of the particles which are supposedly composed of smaller structures.

If the samples are thermally treated at a higher temperature (580 °C), the particles grow in number and in size to approximately 700 nm for the sample C as well as for sample C_Er (not shown).

The increased aluminum concentration in sample B results in a very similar microstructure in comparison to sample C as shown in Fig. 7. In this case, the etched surface was coated with iridium for an enhanced electron signal based on topography contrast. The glass-ceramics, heat treated at 560 °C for 20 h in analogy to sample C, shows a bimodal distribution of particles with sizes of around 50 and 360 nm. Increasing the annealing temperature to 580 °C results in more numerous and larger particles with sizes of around 460 nm (Fig. 7a). Additionally, a substructure of interpenetrating smaller particles of sizes below 100 nm is observed between the larger particles (see Fig. 7b).

The static luminescence spectra of sample C_Er are shown in Fig. 8 a. Relatively broad excitation (left) and emission (right) peaks of Er^{3+} typical for an amorphous host material are observed. The excitation peaks correspond to the ground state absorption of the energy levels $^4G_{9/2}$ (365 nm), $^4G_{11/2}$ (380 nm), $^2H_{5/2}$ (405 nm), $^4F_{3/2}$ (442 nm), $^4F_{5/2}$ (450 nm), $^4F_{7/2}$ (490 nm) and $^2H_{11/2}$ (520 nm). Most of the luminescence emission in the visible range at room temperature originates from the electronic energy level $^4S_{3/2}$. Noticeable are two fluorescence emission peaks, a relatively strong emission at about 545 nm ($^4S_{3/2} \rightarrow {}^4I_{15/2}$, green) and a weak peak at 660 nm ($^4F_{9/2} \rightarrow {}^4I_{15/2}$, red). The heat treatment results in a systematic increase in intensity up to an annealing temperature of 580 °C. For the sample annealed at 600 °C, the luminescence emission decreases again. Sample B shows a similar result, but here the intensity of the 600 °C sample is even smaller than for the base glass (not shown). For a better comparison and classification, a sintered ceramic sample of Er^{3+} doped ($1 \cdot 10^{20}$ cm^{-3}) CaF_2 was prepared by solid state reaction (Fig. 8 b).

Furthermore, a fluoride free glass similar to the composition of sample C was prepared. In this sample, all fluorides are replaced by the respective oxides. The fluoride free sample shows slightly smaller emission intensity in comparison to fluoride containing glasses and glass-ceramics. A large difference in the spectra can be

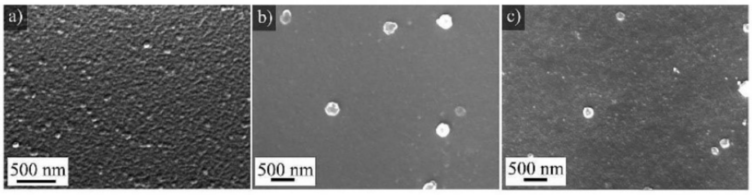

Fig. 5. SEM micrographs of the etched fractured surface of a) sample C (as casted glass), b) sample C (560 °C/20 h) and c) sample C_Er (560 °C/20 h).

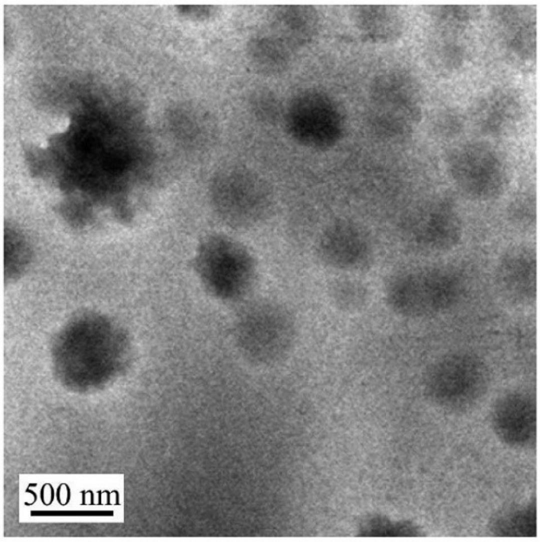

Fig. 6. TEM bright field image of sample C_Er heat treated at 560 °C for 20 h.

observed for the CaF_2 sinter ceramics. The excitation and emission peaks are notably taller and obviously split up into several components. This is especially well to be seen for the emission peak at around 545 nm: For the glass ceramics (all samples B and C), a clear splitting into 2 distinct peaks is observed, while for the CaF_2 sample at least 4 peaks can be resolved. Furthermore, most of the peak positions are shifted to slightly smaller wavelengths for the CaF_2 sample. Additionally, the spectra of the base glass of sample B are included in the diagram. Its intensity is somewhat higher than for the base glass of sample C.

4. Discussion

Fundamental studies on the nanocrystallization of CaF_2 from oxyfluoride glasses have been conducted [7,8,39]. Hence, these glasses proved to be promising for the preparation of photonic materials, i.e. as potential photo-thermo-refractive glass [31,32,40] or by rare earth doping [41]. In the literature, compositions of oxyfluoride glasses which show the ability to incorporate rare earth ions in the precipitated crystal phase possess usually high Al_2O_3 concentrations. Accordingly, the Al_2O_3 concentration was varied in this study based on the original glass with an Al_2O_3 concentration of 3.9 mol% [7].

However, the sample A with 10 mol% Al_2O_3 showed a remarkable opaqueness. Only glass C with 6 mol% Al_2O_3 was colorless and transparent (see Fig. 1). The as casted glasses were examined by XRD, but did not show crystalline phases although heterogeneities were detected in the electron microscope. This suggests that a phase separation into a fluoride rich and a silica rich phase occurs that gives rise to the opacity. The proportion of F bonded to Al was reported to increase with increasing Al_2O_3 concentration. This would explain the higher tendency to phase separation with increasing Al_2O_3 concentration [33,42].

Only a slight change in the glass transition temperature of the samples was observed for varying Al_2O_3 concentrations. In sample A, T_g is only 10 K higher (see Table 2) in comparison to samples B and C. Since in the studied glasses, the molar concentration of Al_2O_3 is much smaller than the concentration of network modifiers, in the homogeneous glass, aluminum should predominantly be incorporated in four-fold coordination, i.e. as AlO_4^- tetrahedra [43–46]. Hence, an increasing Al_2O_3 concentration leads to increasing network connectivity. Thus, a higher Al_2O_3 concentration should lead to increasing viscosity and a higher T_g [47,48]. Additionally, some aluminum should occur in five- and six-fold coordination due to the presence of fluorine [35]. These effects lead to the observed marginal changes in T_g with changing glass composition. However, this effect is superimposed by the phase separation, which leads to the enrichment of Ca, F and possibly also Al in the droplet phase

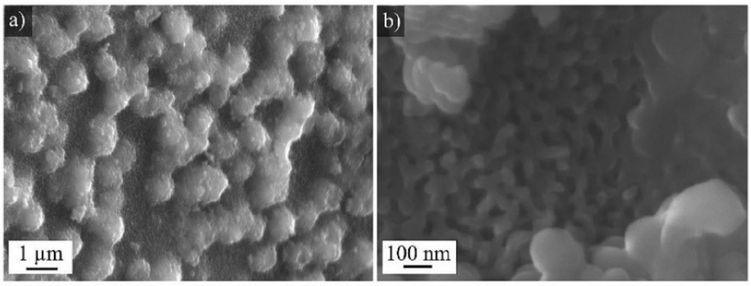

Fig. 7. SEM micrographs of sample B heat treated at 580 °C for 20 h (different magnifications). The polished surface was etched with diluted HF and coated with iridium.

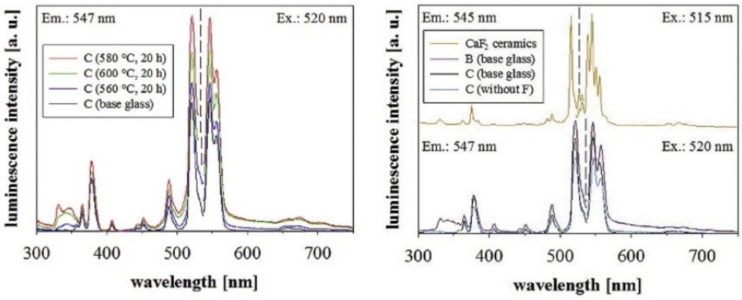

Fig. 8. a) Excitation (left of the dashed line) and emission (right of the dashed line) spectra of samples C_Er untreated and heat treated at different temperatures. b) For comparison, spectra of a Er^{3+} doped CaF_2 ceramic, a fluorine free sample and sample B_Er are shown.

which is not observed in the dilatometric measurement. Here the measured T_g is attributed to the residual glassy matrix. Otherwise a second kink in the dilatometric curve should be observed, attributed to the droplet phase. However, this is not the case (not shown).

The crystallization temperature T_c decreases with increasing Al_2O_3 concentration, which at a first glance appears surprising. This behavior is not expected from a homogeneous glass, where usually the tendency towards crystallization decreases with increasing Al_2O_3 concentration (at least in the concentration range under investigation). Hence, it is assumed that this effect is due to the liquid/liquid phase separation. The first precipitated phase during heating the sample is CaF_2, which crystallizes inside the droplets of the liquid/liquid phase separated glass. The composition of the droplet phase, however, is totally different from that of the nominal glass composition and is surely not an alumosilicate glass. The local increase of the Ca and F ion concentration inside the droplets drives the crystallization. This explains the occurrence of CaF_2 peaks in the XRDs already at lower heat treatment temperature and comparatively short treatment time (see Fig. 3 and Fig. 4). The crystallization behavior of the studied glasses is similar to the mechanism of nano crystallization previously described in the literature [2,49]. During the course of the crystallization, the viscosity and hence also T_g around the growing nuclei increases until the crystallization gets frozen if T_g of the residual glass phase reaches the supplied heat treatment temperature [7]. In the present case, the supplied crystallization time is not long enough to reach this saturation point (see Fig. 2). For short heat treatment times (<1 h), surprisingly a slight drop of T_g is observed (see inset Fig. 2). This effect is observed in all samples, although it is less pronounced for the sample B/B_Er. This can be explained as follows: (i) the as casted glass is already phase separated (ii) during nucleation and crystallization inside the droplets or at the droplet/matrix interface, other network modifiers, such as Na^+, K^+ are shoved away from the crystallization front and may diffuse out of the droplets. Since these are network modifying ions and hence the fastest diffusing species, this will lead to a decrease in the viscosity of the matrix phase. (iii) During ongoing crystallization, Ca^{2+} as well as F^- must further diffuse from the matrix to the droplets. Since this results in a depletion of the matrix phase in Ca^{2+} and F^-, the viscosity increases. This leads to a deceleration of the crystal growth, i.e. the crystals do not exceed the size of the initial droplet phase. The growth of the spherical particles, i.e. droplet phase separation, during heat treatment is also observed in the micrographs. A schematic representation of the proposed nanocrystallization mechanism is illustrated in Fig. 9.

A liquid/liquid phase separation as a precursor stage of crystallization is preferred because the interfacial energy between two glassy phases is much lower than that between a glassy and a crystalline phase [50]. Hence, the kinetic hindrance of the crystallization is much larger than that of the phase separation.

Doping with erbium does not influence the measured T_g but affects the crystallization behavior. The XRD results prove findings from the literature where it is described that erbium triggers the CaF_2 crystallization [35]. Erbium doped samples show CaF_2 peaks already at lower heat treatment temperatures (see Fig. 3). Sample C without erbium does not show crystallization peaks for CaF_2 after 560 °C/20 h heat treatment, but SEM micrographs show spherical structures with a size of 360 nm and a high number of structures with sizes of around 50 nm. However, TEM micrographs show only structures with diameters from 300 to 500 nm (see Fig. 6). It is assumed that during sample preparation using ion milling or even during observation, i.e. beam damage, the sample may change the substructure. It is well known that the electron beam, especially in the TEM, may cause diffusion, evaporation or amorphization in sensitive samples due to introduced heat and electron charges. The erbium doped sample (C_Er) shows a more pronounced formation of smaller structures with sizes of around 50 nm. This could be described by a higher tendency to phase separation also caused by comparatively small erbium concentrations. Similar observations were made for a Tb doped oxyfluoride glass [41]. The higher tendency to phase separation with higher Al concentration is supported by SEM results, which give evidence of an increased number of smaller structures (not shown). Neither the aluminum nor the erbium concentrations have a significant influence on the crystallite size. The limitation of the crystal size is due to the interface controlled crystallization mechanism as previously described. However, while increasing the heat treatment temperature to 580 °C, the larger structures grow in number and size to approximately 460 nm resulting in an interpenetrating structure similar to previous studies [51]. The diameters of these structures are much larger than the mean crystallite sizes calculated from XRD line broadening and hence they should contain numerous CaF_2 crystals.

Crystallization of the second crystalline phase cuspidine is also influenced by aluminum. With increased aluminum concentration, it occurs at lower temperatures. Cuspidine $Ca_4Si_2O_7(F, OH)_2$ is monoclinic ($P2_1/a$) and is obviously closely related to the crystallization of cubic CaF_2 (Fm3m) since with the appearance of cuspidine, the intensities of the CaF_2 peaks decrease.

This leaves the question of the location of the rare earth ions. An incorporation of erbium into the crystalline CaF_2 phase might be proved by a shift of the peaks in the XRD patterns after thermal treatment, if the lattice parameter is sufficiently different. In the present study, XRD data do not show a significant effect. The luminescence spectra could indicate the location of the rare earth ions since different local structures and phonon energies might

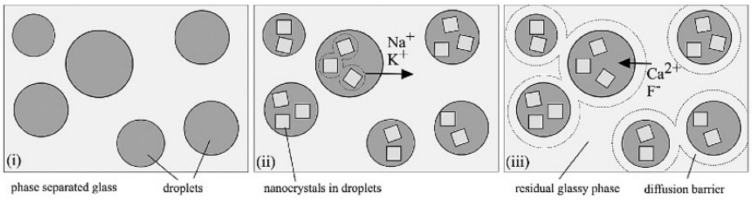

Fig. 9. Schematic of the nanocrystallization mechanism; (ii) phase separated as casted glass, (ii) CaF_2 nanocrystals inside the droplets, network modifiers diffuse out of droplets, (iii) diffusion of Ca^{2-} and F^- from matrix to droplets, formation of a diffusion barrier around droplets.

affect the shape of the spectra and the intensities of the respective lines. During crystallization, the intensities of the fluorescence lines increase, which might have different reasons. One of them is the incorporation of Er^{3+} into the CaF_2 lattice and the other is an increased scattering/optical path length due to phase separation and crystallization (see Fig. 8). The latter effect is reversed if light scattering becomes too strong which is caused by too large dimensions of the heterogeneities. Therefore, the intensities of the fluorescence lines decrease if the samples were annealed at too high temperatures. Furthermore, additional peak splitting is not observed for the thermally treated samples: Er^{3+} ions incorporated into large CaF_2 crystals exhibit a clearly different spectrum as shown for the sintered CaF_2 sample in Fig. 8 b. However, the spectrum may change if the crystals have sizes in the nanometer range as shown in Table 3.

The fluorescence of the fluoride free sample shows notably lower emission intensities. This is evidence that fluoride ions play an important part and fluoride ions should closely be connected to erbium ions, i.e. fluoride should be incorporated into the first coordination shell of erbium. Nevertheless, the erbium ions need not necessarily be incorporated into the CaF_2 lattice, but might also be located in the droplets which are enriched in Ca and F. Fig. 8 b also shows a higher emission intensity for sample B compared to sample C. This is most likely due to a stronger phase separation/crystallization in all samples of series B with higher Al_2O_3 concentration.

5. Conclusion

Glasses with the mol% compositions (63-*x*) SiO_2, *x* Al_2O_3, 12.3 CaO, 5.3 K_2O, 9.0 Na_2O and 10.4 CaF_2 with $x = (10, 8, 6)$ doped with Er^{3+} ($1 \cdot 10^{20}\,cm^{-3}$) were prepared. The as cast glasses were phase separated. Subsequent thermal treatment slightly above the glass transition temperature (560–620 °C) led to the precipitation of CaF_2 nanocrystals with sizes smaller than 40 nm. Fluoride is incorporated into the coordination shell of Er^{3+} and occurs either in the CaF_2 crystals or in the amorphous part of the droplets. During further crystallization, Ca^{2+} and F^- diffuse to the droplets and lead to crystal growth. The glass phase near the droplets is depleted in Ca^{2+} and F^- which leads to an increase in viscosity, i.e. also in T_g. This increase in viscosity runs parallel to a decrease in the diffusivities and leads to a deceleration of crystal growth. Finally, a rigid shell is formed around the droplets which hinders further crystal growth or Ostwald ripening. The pronounced microstructure leads to local concentration quenching of erbium influencing the fluorescence measurements.

Acknowledgement

This work was funded by the Bundesministerium für Bildung und Forschung, Germany (Wachstumskern Brightlas, 03WKCF3E)

References

[1] M. Mortier, Between glass and crystal: glass-ceramics, a new way for optical materials, Philos. Mag. B 82 (2002) 745–753.
[2] C. Bocker, C. Rüssel, I. Avramov, Transparent nano crystalline glass-ceramics by interface controlled crystallization, Int. J. Appl. Glass Sci. 4 (2013) 174–181.
[3] C. Bocker, I. Avramov, C. Rüssel, Viscosity and diffusion of barium and fluoride in $Na_2O/K_2O/Al_2O_3/SiO_2/BaF_2$ glasses, Chem. Phys. 369 (2010) 96–100.
[4] C. Bocker, S. Bhattacharyya, T. Höche, C. Rüssel, Size distribution of BaF_2 nanocrystallites in transparent glass ceramics, Acta Mater. 57 (2009) 5956–5963.
[5] C. Bocker, C. Rüssel, Self-organized nano-crystallisation of BaF_2 from $Na_2O/K_2O/BaF_2/Al_2O_3/SiO_2$ glasses, J. Eur. Ceram. Soc. 29 (2009) 1221–1225.
[6] V.S. Raghuwanshi, A. Hoell, C. Bocker, C. Rüssel, Experimental evidence of a diffusion barrier around BaF_2 nanocrystals in a silicate glass system by ASAXS, Crystengcomm 14 (2012) 5215–5223.
[7] C. Rüssel, Nanocrystallization of CaF_2 from $Na_2O/K_2O/CaO/CaF_2/Al_2O_3/SiO_2$ glasses, Chem. Mater. 17 (2005) 5843–5847.
[8] A. Hoell, Z. Varga, V.S. Raghuwanshi, M. Krumrey, C. Bocker, C. Rüssel, ASAXS study of CaF_2 nanoparticles embedded in a silicate glass matrix, J. Appl. Crystallogr. 47 (2014) 60–66.
[9] C. Bocker, J. Wiemert, C. Rüssel, The effect of viscosity on nanocrystallization of strontium fluoride from a silicate glass, Solid State Sci. 30 (2014) 55–60.
[10] C. Bocker, J. Wiemert, C. Rüssel, The formation of strontium fluoride nano crystals from a phase separated silicate glass, J. Eur. Ceram. Soc. 33 (2013) 1737–1745.
[11] S. Bhattacharyya, T. Höche, N. Hemono, M.J. Pascual, P.A. van Aken, Nano-crystallization in LaF_3-Na_2O-Al_2O_3-SiO_2 glass, J. Cryst. Growth 311 (2009) 4350–4355.
[12] N. Hemono, G. Pierre, F. Munoz, A. de Pablos-Martin, M.J. Pascual, A. Duran, Processing of transparent glass-ceramics by nanocrystallisation of LaF_3, J. Eur. Ceram. Soc. 29 (2009) 2915–2920.
[13] A. de Pablos-Martin, G.C. Mather, F. Munoz, S. Bhattacharyya, T. Höche, J.R. Jinschek, T. Heil, A. Duran, M.J. Pascual, Design of oxy-fluoride glass-ceramics containing $NaLaF_4$ nano-crystals, J. Non-Cryst. Solids 356 (2010) 3071–3079.
[14] A. Herrmann, M. Tylkowski, C. Bocker, C. Rüssel, Cubic and hexagonal $NaGdF_4$ crystals precipitated from an aluminosilicate glass: preparation and luminescence properties, Chem. Mater. 25 (2013) 2878–2884.
[15] R. Wurth, C. Rüssel, The crystallization of (Pb, Yb, Er)F-X nano particles from glasses with the composition 20 SiO_2 • 13.5 B_2O_3 • 6 Al_2O_3 • 10 PbO • 6.6 CdO • 20 PbF_2 • 13.3 CdF_2 • 10 YbF_3 • 0.5 ErF_3, Solid State Sci. 13 (2011) 1132–1136.
[16] A.J. Stevenson, H. Serier-Brault, P. Gredin, M. Mortier, Fluoride materials for optical applications: single crystals, ceramics, glasses, and glass-ceramics, J. Fluorine Chem. 132 (2011) 1165–1173.
[17] I. Gugov, M. Müller, C. Rüssel, Transparent oxyfluoride glass ceramics co-doped with Er^{3+} and Yb^{3-} - crystallization and upconversion spectroscopy, J. Solid State Chem. 184 (2011) 1001–1007.
[18] S. Tanabe, H. Hayashi, T. Hanada, N. Onodera, Fluorescence properties of Er^{3+} ions in glass ceramics containing LaF_3 nanocrystals, Opt. Mater. 19 (2002) 343–349.
[19] C.S. Ma, Q. Jiao, L.J. Li, D.C. Zhou, Z.W. Yang, Z.G. Song, J.B. Qiu, Up-conversion luminescence properties and energy transfer of Er^{3+}/Yb^{3+} co-doped oxyfluoride glass ceramic containing CaF_2 nano-crystals, Chin. Phys. B 23 (2014), 057802.
[20] W. Seeber, E.A. Downing, L. Hesselink, M.M. Fejer, D. Ehrt, Pr^{3+}-doped fluoride glasses, J. Non-Cryst. Solids 189 (1995) 218–226.
[21] G.H. Beall, Glass-ceramics for photonic applications, Glass Sci. Technol. 73 (2000) 3–11.
[22] P.P. Fedorov, A.A. Luginina, A.I. Popov, Transparent oxyfluoride glass ceramics, J. Fluorine Chem. 172 (2015) 22–50.
[23] P. Babu, K.H. Jang, C.S. Rao, L.A. Shi, C.K. Jayasankar, V. Lavin, H.J. Seo, White light generation in Dy^{3+}-doped oxyfluoride glass and transparent glass-ceramics containing CaF_2 nanocrystals, Optic Express 19 (2011) 1836–1841.
[24] C.R. Kesavulu, M.Y. Yoo, J.H. Lee, K.S. Lim, P. Dharmaiah, C.K. Jayasankar, P. Babu, Optical and upconversion properties of Er^{3+}-doped oxyfluoride

transparent glass-ceramics containing SrF_2 nanocrystals, J. Mater. Res. 28 (2013) 1481–1489.

[25] P. Babu, K.H. Jang, E.S. Kim, L. Shi, H.J. Seo, F. Rivera-Lopez, U.R. Rodriguez-Mendoza, V. Lavin, R. Vijaya, C.K. Jayasankar, L.R. Moorthy, Spectral investigations on Dy^{3+}-doped transparent oxyfluoride glasses and nanocrystalline glass ceramics, J. Appl. Phys. 105 (2009), 013516.

[26] P. Babu, K.H. Jang, E.S. Kim, L. Shi, R. Vijaya, V. Lavin, C.K. Jayasankar, H.J. Seo, Optical properties and energy transfer of Dy^{3+}-doped transparent oxyfluoride glasses and glass-ceramics, J. Non-Cryst. Solids 356 (2010) 236–243.

[27] X.S. Qiao, X.P. Fan, J. Wang, M.Q. Wang, Luminescence behavior of Er^{3+} ions in glass-ceramics containing CaF_2 nanocrystals, J. Non-Cryst. Solids 351 (2005) 357–363.

[28] D.Q. Chen, Y.S. Wang, Y.L. Yu, E. Ma, F. Bao, Z.J. Hu, Y. Cheng, Influences of Er^{3+} content on structure and upconversion emission of oxyfluoride glass ceramics containing CaF_2 nanocrystals, Mater. Chem. Phys. 95 (2006) 264–269.

[29] H. Hijiya, T. Kishi, A. Yasumori, Photoluminescent properties of fresnoite phosphors prepared from phase-separated $BaO\text{-}TiO_2\text{-}SiO_2$ glasses, J. Ceram. Soc. Jpn. 116 (2008) 1255–1259.

[30] J.L. Lumeau, E.D. Zanotto, A review of the photo-thermal mechanism and crystallization of photo-thermo-refractive (PTR) glass, Int. Mater. Rev. 62 (2017) 348–366.

[31] M. Stoica, G.N.B.M. de Macedo, C. Rüssel, Photo induced crystallization of CaF_2 from a $Na_2O/K_2O/CaO/CaF_2/Al_2O_3/SiO_2$ glass, Opt. Mater. Express 4 (2014) 1574–1585.

[32] M. Stoica, A. Herrmann, J. Hein, C. Rüssel, Uv-vis spectroscopic studies of a CaF_2 photo-thermo-refractive glass 62 (2016) 424–432.

[33] M.H. Imanieh, B.E. Yekta, V. Marghussian, I.R.M. Benenzuela, A.H. Creus, S. Shakhesi, E. Eslami, Effect of alumina content and heat treatment on microstructure and upconversion emission of Er^{3+} ions in oxyfluoride glass-ceramics, J. Rare Earths 30 (2012) 1228–1234.

[34] Y. Kishi, S. Tanabe, S. Tochino, G. Pezzotti, Fabrication and efficient infrared-to-visible upconversion in transparent glass ceramics of Er-Yb co-doped CaF_2 nano-crystals, J. Am. Ceram. Soc. 88 (2005) 3423–3426.

[35] G.B. Wu, S.H. Fan, Y.H. Zhang, G.Q. Chai, Z.J. Ma, M.Y. Peng, J.R. Qiu, G.P. Dong, 2.7 µm emission in Er^{3+}:CaF_2 nanocrystals embedded oxyfluoride glass ceramics, Optic Lett. 38 (2013) 3071–3074.

[36] J.R. Barros, C. Bocker, C. Rüssel, The effect of Er^{3+} and Sm^{3+} on phase separation and crystallization in $Na_2O/K_2O/BaF_2/BaO/Al_2O_3/SiO_2$ glasses, Solid State Sci. 12 (2010) 2086–2090.

[37] Z.J. Hu, Y.S. Wang, E. Ma, F. Bao, Y.L. Yu, D.Q. Chen, Crystallization and spectroscopic properties investigations of Er^{3+} doped transparent glass ceramics containing CaF_2, Mater. Res. Bull. 41 (2006) 217–224.

[38] L. Alexander, H.P. Klug, Determination of crystallite size with the x-ray spectrometer, J. Appl. Phys. 21 (1950) 137–142.

[39] R.P.F. de Almeida, C. Bocker, C. Rüssel, Size of CaF_2 crystals precipitated from glasses in the $Na_2O/K_2O/CaO/CaF_2/Al_2O_3/SiO_2$ system and percolation theory, Chem. Mater. 20 (2008) 5916–5921.

[40] M. Stoica, C. Patzig, C. Bocker, W. Wisniewski, M. Kracker, T. Hoche, C. Rüssel, Structural evolution of CaF_2 nanoparticles during the photoinduced crystallization of a $Na_2O\text{-}K_2O\text{-}CaO\text{-}CaF_2\text{-}Al_2O_3\text{-}ZnO\text{-}SiO_2$ glass, J. Mater. Sci. 52 (2017) 13390–13401.

[41] C. Bocker, A. Herrmann, P. Loch, C. Rüssel, The nano-crystallization and fluorescence of terbium doped $Na_2O/K_2O/CaO/CaF_2/Al_2O_3/SiO_2$ glasses, J. Mater. Chem. C 3 (2015) 2274–2281.

[42] R.G. Hill, A. Stamboulis, R.V. Law, Characterisation of fluorine containing glasses by F-19, Al-27, Si-29 and P-31 MAS-NMR spectroscopy, J. Dent. 34 (2006) 525–532.

[43] H. Scholze, Glas- Natur, Struktur und Eigenschaften, third ed., Springer Verlag, Berlin Heidelberg, New York London Paris Tokyo, 1988.

[44] P.C. Hess, M.I. Wood, Aluminum coordination in metaaluminous and peralkaline silicate melts, Contrib. Mineral. Petrol. 81 (1982) 103–112.

[45] M. Sroda, K. Szlosarczyk, M. Rozanski, M. Sitarz, P. Jelen, Spectroscopic properties of transparent Er-doped oxyfluoride glass-ceramics with GdF_3, Spectrochim. Acta 134 (2015) 631–637.

[46] B.O. Mysen, P. Richet, Silicate Glasses and Melts: Properties and Structure, Elsevier, Amsterdam, 2005.

[47] J.E. Shelby, Introduction to Glass Science and Technology, The Royal Society of Chemistry, Cambridge, UK, 2005.

[48] T. Munhoz, N. Karpukhina, R.G. Hill, R.V. Law, L.H. De Almeida, Setting of commercial glass ionomer cement Fuji IX by Al-27 and F-19 MAS-NMR, J. Dent. 38 (2010) 325–330.

[49] C. Bocker, C. Rüssel, I. Avramov, Crystal growth in non-isochemical, highly viscous liquids and percolation theory, Chem. Phys. 406 (2012) 50–54.

[50] R.G. Hill, C. Goat, D. Wood, Thermal-analysis of a $SiO_2\text{-}Al_2O_3\text{-}CaO\text{-}CaF_2$ glass, J. Am. Ceram. Soc. 75 (1992) 778–785.

[51] C.G. Lin, C. Bocker, C. Rüssel, Nanocrystallization in oxyfluoride glasses controlled by amorphous phase separation, Nano Lett. 15 (2015) 6764–6769.

Article 3.5

M. Stoica, M. Kracker, C. Rüssel

Photoinduced Formation of Silver Nanoparticles in a new $Na_2O/K_2O/CaO/CaF_2/Al_2O_3/ZnO/SiO_2$ Photo Thermal Refractive Glass-Evidence of Ag/AgBr core-shell structures

Optical Materials Express **2017** 7(12): 4427-4434

DOI: 10.1364/OME.7.004427

Photoinduced Formation of Silver Nanoparticles in a new $Na_2O/K_2O/CaO/CaF_2/Al_2O_3/ZnO/SiO_2$ Photo Thermal Refractive Glass- Evidence of Ag/AgBr core-shell structures			
Beteiligt an			
	Martina Stoica	Dr. Michael Kracker	Prof. Christian Rüssel
Konzeption des Forschungsansatzes	X		X
Planung der Untersuchung	X		
Datenerhebung	X	X	
Datenanalyse und Interpretation	X	X	
Schreiben des Manuskripts	X	X	X
Vorschlag Anrechnung Publikationsäquivalente	1,0		

Research Article Vol. 7, No. 12 | 1 Dec 2017 | OPTICAL MATERIALS EXPRESS 4427

Optical Materials EXPRESS

Photoinduced formation of silver nanoparticles in a new $Na_2O/K_2O/CaO/CaF_2/Al_2O_3/ZnO/SiO_2$ photo thermal refractive glass: evidence of Ag-AgBr core shell structures

MARTINA STOICA,* MICHAEL KRACKER, AND CHRISTIAN RÜSSEL

Otto-Schott-Institut, Jena University, Fraunhoferstraße 6, 07743 Jena, Germany
**martina.stoica@gmx.de*

Abstract: Photo thermal refractive glasses of the type Na_2O-SiO_2-Al_2O_3-K_2O-CaO-CaF_2-ZnO doped with CeO_2, Ag_2O, SnO_2, Sb_2O_3 were prepared using different concentrations of KBr. A UV irradiation followed by a thermal treatment leads to the formation of Ag-nanoparticles, indicated by the appearance of a plasmon resonance peak. This optical resonance position shifts with increasing KBr concentrations to higher wavelengths caused by the formation of an AgBr shell. The Mie theory with the aid of the optical dispersion of AgBr together with the measured dispersion of the used glasses was successfully applied to describe the optical relation of particle size and AgBr core shell thickness within the given glass. The results were compared with UV-vis-NIR spectroscopy.

OCIS codes: (160.0160) Materials; (160.2750) Glass and other amorphous materials; (160.5335) Photosensitive materials; (160.4760) Optical properties; (300.0300) Spectroscopy.

References and links

1. M. Quinten, *Optical Properties of Nanoparticle Systems: Mie and Beyond* (Wiley-VCH, 2011).
2. F. Gonella, "Silver doping of glasses," Ceram. Int. **41**(5), 6693–6701 (2015).
3. U. Kreibig, "Small Silver Particles in Photosensitive Glass - Their Nucleation and Growth," Appl. Phys. (Berl.) **10**(3), 255–264 (1976).
4. S. D. Stookey, "Photosensitive Glass - a New Photographic Medium," Ind. Eng. Chem. **41**(4), 856–861 (1949).
5. V. A. Borgman, L. B. Glebov, N. V. Nikonorov, G. T. Petrovskii, V. V. Savvin, and A. D. Tsvetkov, "Photothermorefractive Effect in Silicate-Glasses," Dokl. Akad. Nauk SSSR **309**(2), 336–339 (1989).
6. L. B. Glebov, N. V. Nikonorov, E. I. Panysheva, G. T. Petrovskii, V. V. Savvin, I. V. Tunimanova, and V. A. Tsekhomskii, "New Potentialities of Photosensitive Glasses for Volume Phase Hologram Recording," Opt. Spektrosk. **73**(2), 404–412 (1992).
7. L. B. Glebov, N. V. Nikonorov, Y. I. Panysheva, G. T. Petrovskii, V. V. Savvin, I. V. Tunimanova, and V. A. Tsekhomskii, "Multichromatic Glasses - a New Material for Recording of Volumetric Phase Holograms," Dokl. Akad. Nauk SSSR **314**(4), 849–853 (1990).
8. M. Stoica, G. N. B. M. de Macedo, and C. Rüssel, "Photo induced crystallization of CaF_2 from a $Na_2O/K_2O/CaO/CaF_2/Al_2O_3/SiO_2$ glass," Opt. Mater. Express **4**(8), 1574–1585 (2014).
9. W. A. Weyl, *Coloured Glasses* (The Society of Glass Technology, 1951).
10. C. F. Bohren and D. R. Huffman, *Absorption and scattering of light by small particles* (Wiley, 1983).
11. D. Manikandan, S. Mohan, and K. G. M. Nair, "Annealing-induced metallic core-shell clusterization in soda-lime glass: an optical absorption study - experiment and theory," Physica B **337**(1–4), 64–68 (2003).
12. A. P. Nacharov, N. V. Nikonorov, A. I. Sidorov, and V. A. Tsekhomskii, "Influence of ultraviolet irradiation and heat treatment on the morphology of silver nanoparticles in photothermorefractive glasses," Glass Phys. Chem. **34**(6), 693–699 (2008).
13. J. Lumeau, L. Glebova, and L. B. Glebov, "Influence of UV-exposure on the crystallization and optical properties of photo-thermo-refractive glass," J. Non-Cryst. Solids, **354**(2-9), 425–430 (2008).
14. L. Glebova, J. Lumeau, M. Klimov, E. D. Zanotto, and L. B. Glebov, "Role of bromine on the thermal and optical properties of photo-thermo-refractive glass," J. Non-Cryst. Solids, **354**(2-9), 456–461 (2008).
15. J. Lumeau, A. Sinitskii, L. Glebova, L. B. Glebov, and E. D. Zanotto, "Spontaneous and photo-induced crystallisation of photo-thermo-refractive glass," Phys. Chem. Glasses-B **48**(4), 281–284 (2007).
16. N. V. Nikonorov, A. I. Sidorov, V. A. Tsekhomskii, and K. E. Lazareva, "Effect of a dielectric shell of a silver nanoparticle on the spectral position of the plasmon resonance of the nanoparticle in photochromic glass," Opt. Spectrosc. **107**(5), 705–707 (2009).

#304786 https://doi.org/10.1364/OME.7.004427
Journal © 2017 Received 17 Aug 2017; revised 25 Oct 2017; accepted 25 Oct 2017; published 29 Nov 2017

17. V. A. Aseev, P. A. Burdaev, E. V. Kolobkova, and N. V. Nikonorov, "Fluorophosphate glasses activated by rare-earth ions and AgBr," Glass Phys. Chem. **38**(4), 366–372 (2012).
18. M. Stoica, A. Herrmann, J. Hein, and C. Rüssel, "UV-vis spectroscopic studies of a CaF_2 Photo-Thermo-Refractive Glass," Opt. Mater. **62**, 424–432 (2016).
19. S. H. Wemple, "Refractive-Index Behavior of Amorphous Semiconductors and Glasses," Phys. Rev. B **7**(8), 3767–3777 (1973).
20. P. Laven, "Simulation of rainbows, coronas and glories using Mie theory and the Debye series," J. Quant. Spectrosc. Ra. **89**(1–4), 257–269 (2004).
21. P. B. Johnson and R. W. Christy, "Optical Constants of Noble Metals," Phys. Rev. B **6**(12), 4370–4379 (1972).
22. H. Schröter, "On the refractive indices of some heavy-metal halides in the visible and calculation of interpolation formulas for dispersion," Z. Phys. **67**(1,2), 24–36 (1931).
23. M. Stoica, C. Patzig, C. Bocker, W. Wisniewski, M. Kracker, T. Höche, and C. Rüssel, "Structural evolution of CaF_2 nanoparticles during the photoinduced crystallization of a Na_2O-K_2O-CaO-CaF_2-Al_2O_3-ZnO-SiO_2 glass," J. Mater. Sci. **52**(23), 13390–13401 (2017).
24. U. Kreibig and P. Zacharia, "Surface Plasma Resonances in Small Spherical Silver and Gold Particles," Z. Phys. **231**(2), 128–143 (1970).
25. E. I. Panysheva, I. V. Tunimanova, and V. A. Tsekhomskii, "The influence of the Matrix Composition of a Polychromatic Glass on its Properties," Fiz. Khim. Stekla **17**(6), 891–989 (1991).

1. Introduction

Optical properties of glasses can be modified by the formation of metal colloids inside the glass matrix [1]. In particular, the photosensitization by metallic silver is of great interest for optical applications [2]. The nucleation and growth kinetics of silver particles in a photo process show the requirement of UV light and that even small amounts of cerium sensitize this process [3]. Stookey developed a photo-thermo-induced crystallization process in glass wafers already in 1949 [4]. These photo-thermo-refractive (PTR) glasses are usually silicate glasses doped with Ce, Ag, Sn, Sb and Br [5]. This was the beginning for modern volume phase hologram writing using refractive index modulation [6]. UV exposure leads to a redox reaction where Ce^{3+} is oxidized ($Ce^{3+} + h\upsilon \rightarrow Ce^{4+} + e^-$). The released electrons are trapped by various trapping centers, e.g. Sn^{4+}, Sb^{5+} and Ag^+. The desired equilibrium of the photosensitivity is controlled by the Sb^{3+}/Sb^{5+} and Sn^{2+}/Sn^{4+} redox pairs. The Ag^+ ions are finally reduced to neutral silver atoms Ag^0 ($Ag^+ + e^- \rightarrow Ag^0$). During a subsequent heat treatment step slightly above T_g, the silver particles grow by aggregation of silver atoms. A certain temperature is necessary to reach a sufficiently large diffusion coefficient for a reasonable growth velocities. These Ag cluster act as nuclei for (earth) alkaline fluoride nano crystallization in a second heat treatment step at a higher temperature [5, 7, 8]. In the case that the Ag particles are small compared to the wavelength of light, the colour of the glass is determined by size, shape, volume fraction of the colloidal metal particles as well as the dispersion properties of the glass matrix [9, 10]. Also the optical properties of core-shell structures within the nano scale range are described in the literature [11]. The changes in the localized surface plasmon resonance are easy accessible by optical absorption spectroscopy.

In photo-thermo-refractive glass, the nucleation and growth of the silver particles is affected by the dosage of UV exposure and by the heat treatment temperature [12, 13]. This affects not only the shift of the surface plasmon resonance (SPR) band maximum, but also the full width at half maximum [12]. In conventional NaF PTR glass, a linear increase of the Ag absorption band position with the UV dosage is observed [13]. Moreover, the Ag band maximum shifts to longer wavelengths with increasing bromide concentration [14]. It is proposed, that this may be associated with the appearance of silver bromide particles shell around the Ag cluster which results in an additional shift of the plasmon resonance peak to longer wavelengths [15]. More likely is that the occurrence of a shell with high refractive index around the silver nanoparticles is responsible for this behavior [16]. The addition of low quantities of AgBr in a fluorophosphate glass matrix leads to a shift of the plasmon absorption band of silver nanoparticles after heat treatment to higher wavelengths. Using simulations according to Mie theory showed that a ~0.5 nm AgBr shell formed on the surface of the metallic Ag^0_n cluster might explain this behavior [17].

Research Article Vol. 7, No. 12 | 1 Dec 2017 | OPTICAL MATERIALS EXPRESS 4429

Optical Materials EXPRESS

Glasses within the system $Na_2O/K_2O/CaO/CaF_2/Al_2O_3/ZnO/SiO_2$ were doped with Ce, Ag, Sn, Sb and Br which show photosensitivity and refractive index change after UV exposure and heat treatment due to the tailored nanoscale precipitation of CaF_2 [8, 18]. This paper provides a study on the effect of KBr additions on the plasmonic resonance of metallic silver in the $Na_2O/K_2O/CaO/CaF_2/Al_2O_3/ZnO/SiO_2$ glass system.

2. Experimental part

Glasses with the mol% composition (100-*x*) (60.18% SiO_2 • 12.12% CaO • 9.32% Na_2O • 8.46% CaF_2 • 5.44% K_2O •3.76% Al_2O_3•0.72% ZnO) (*x* KBr) with x = 0.0%, 1.0%, 2.0% were doped with 0.02% Ag_2O, 0.02% CeO_2, 0.02% SnO_2, 0.04% Sb_2O_3 and melted from analytical grade raw materials in 300 g batches. The batch was melted in an inductive furnace for 4 h at a temperature of 1430 °C in a Pt crucible. Stirring was applied to homogenize the melt. After stirring, the melt was cast into a preheated steel mold. The obtained glass was placed in a muffle furnace which was then switched off to enable a slow cooling to room temperature (RT) with a rate of approximately 3 K/min. The glass was cut into pieces of 10 x 10 x 1 mm^3 size and the surfaces were polished.

The final concentration of bromide was measured by X-ray fluorescence (XRF) analysis according to DIN 51001. Nominal Br concentrations and measured Br concentrations (wt%) are listed in Table 1.

Table 1. Comparison of nominal and measured Br concentration of the PTR glasses

sample	nominal Br concentration [wt%]	measured Br concentration [wt%]
KBr 0 mol%	0.00	0.002
KBr 1 mol%	0.61	0.099
KBr 2 mol%	1.21	0.135

UV exposure was carried out with a high pressure Xe arc lamp (LOT Oriel). The thermal treatments were performed in a muffle furnace (Nabertherm N11/H) applying a heating rate of 5 K/min.

Optical absorption spectra were recorded at RT using wavelengths from 200 to 1200 nm by a commercial double beam UV-vis-NIR spectrophotometer (3102PC, Shimadzu) with air as the reference; the error in the wavelength is about ± 1 nm.

Refractive indices were measured at 20 °C with a Pulfrich refractometer PR2 equipped with VoF5 prism at certain wavelengths according to the Fraunhofer lines (D, d, e, F, g, and h).

The dispersion of the glass was calculated using the Wemple equation [19].

$$\frac{1}{n^2(E)-1} = \frac{E_0}{E_d} - \frac{1}{E_0 E_d} * E^2 \tag{1}$$

where E is the light energy (= hν), E_0 is the energy of the effective dispersion oscillator and E_d is the dispersion energy. According to Eq. (1), a plot of measured refractive indices as $1/(n^2-1)$ and the square of photon energy E^2 enables the calculation of E_0/E_d and $1/(E_0E_d)$ from intercept and slope of a simple linear regression. Finally, the optical dispersion of the glass is available for a further adaption. The "MiePlot" software ver. 4.6 (supplied by Laven [20]) based on the BHMIE and BHCOAT algorithm [10] was used to calculate the optical behavior of Ag nano particles with different sizes in a glass matrix. The required dielectric function of Ag is based on data provided by Johnson and Christy [21]. The required optical dispersion for AgBr was taken from Schröter [22].

The plasmon resonance wavelengths of the calculated and measured spectra were determined by fitting the peaks with a Gaussian function and locating of the center of gravity.

3. Results and discussion

The obtained glasses were homogeneous, colorless and transparent. Samples from the glass with the composition (mol%) 59.58 SiO_2 • 12.0 CaO • 9.22 Na_2O • 8.38 CaF_2 • 5.39 K_2O • 3.72 Al_2O_3 • 0.71 ZnO • 1.0 KBr doped with Ag_2O, CeO_2, Sb_2O_3 and SnO_2 were irradiated and heat treated. The influence of the UV irradiation and heat treatment on the silver nano particle formation was investigated. Samples were UV irradiated at the same intensity for different times with a Xe lamp and were subsequent heat treated at 530 °C for 1 h. After heat treatment, the glass samples had a yellow colour due to the presence of colloidal silver nanoparticles. Optical absorption spectra exhibit the characteristic silver plasmon resonance. In previous studies, the photosensitivity of the Ag nano particle formation in this glass matrix has already been shown [8]. The formation of the Ag nanoparticles was studied in detail by high resolution TEM imaging [23]. The results showed that TEM studies in high resolution with high acceleration voltages or comparatively high currents, as needed for EDXS generate artefacts. In particular, an EDXS mapping was not possible due to the high damage of the electron beam. Furthermore, the evidence of Ag nanoparticles with electron microscopy techniques was not possible due to the resolution limit of the method which is 0.5 at%.

Furthermore, samples of the glass were irradiated and heat treated at 450, 480, 500, 515 and 530 °C for 1 h, respectively. The respective absorption band maximum wavelengths of 3the plasmon resonance peaks after irradiation and subsequent heat treatment are shown in Fig. 1.

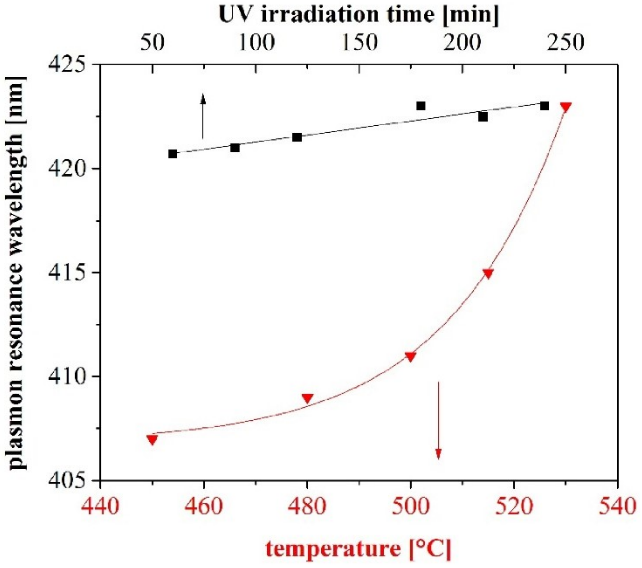

Fig. 1. Comparison of Ag plasmon resonance absorption band maximum wavelengths for: ▼ samples irradiated (180 min, Xe lamp) and heat treated at temperatures of 450 and 530 °C for 1 h, ■ samples irradiated at respective time and heat treated at 530 °C for 1 h.

The position of the plasmon resonance maximum is shifted very slightly to longer wavelengths with increasing irradiation dosage (see Fig. 1). The overall shift of 2.3 nm is very small and is near to the limit of the error of the measurement. A shift of 2.3 nm corresponds to an increase in size of 3 nm at the mentioned wavelength range. Hence, at a certain value of irradiation dosage Ag particles with larger sizes are formed. The dosage of irradiation does affect the number of the formed Ag particles. The position of the Ag plasmon resonance peak maximum is shifted to higher wavelengths with increasing heat treatment temperature. The peak maximum is shifted from a wavelength at 407 nm to 423 nm. The Ag nanoclusters grow with increasing heat treatment temperature and change the plasmon resonance frequency. Moreover, the respective absorption band intensities vs. irradiation time are shown in Fig. 2. The plasmon resonance absorption band intensity is increasing with irradiation dosage up to a certain value and is then decreasing again. The slope of the absorption band intensity with irradiation time is linear. The Ag particles grow with increasing irradiation dosage. With higher UV dosage, more Ce^{3+} is reduced and consequently more electrons are released to reduce Ag^+ to Ag^0 which can agglomerate in a subsequent heat treatment. At a certain size of the Ag cluster the plasmon resonance intensity decreases and the band is broadened [1].

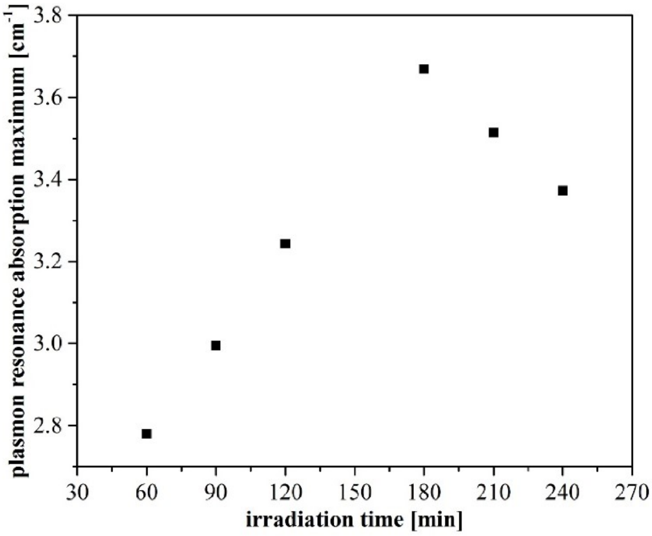

Fig. 2. Ag plasmon resonance absorption band intensity vs. irradiation time; samples irradiated and heat treated at 530 °C for 1 h.

As mentioned the position of the plasmon resonance peak is dependent on the particle size and the refraction index of the matrix surrounding it. The simulation of the Ag plasmon resonance peak position for Ag particle for the glass matrices with the mol% composition (100-x) (60.18% SiO_2 • 12.12% CaO • 9.32% Na_2O • 8.46% CaF_2 • 5.44% K_2O • 3.76% Al_2O_3 • 0.72% ZnO) (x KBr) with $x = 0.0\%$, 1.0%, 2.0%, was performed and is shown in Fig. 3. The calculation was performed using the measured dispersion of the glasses containing different KBr concentrations.

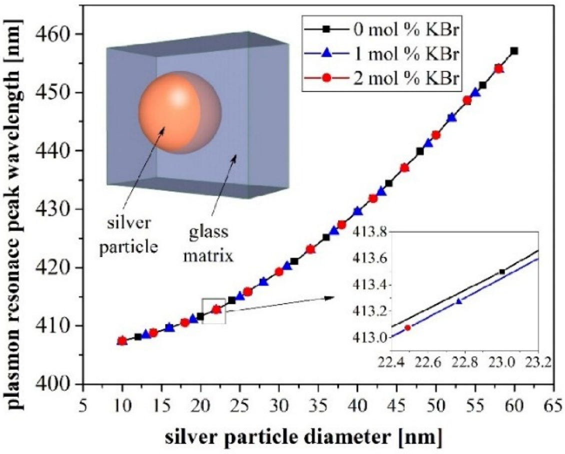

Fig. 3. Simulated plasmon resonance peak positions for a single Ag particle in the glass matrix containing 0 mol %, 1 mol % or 2 mol % KBr, in the initial batch composition.

The calculated resonance wavelength increases from 407 nm for a particle of 10 nm diameter up to 457 nm for a particle of 60 nm in diameter. A comparison of the simulated plasmon resonance peak wavelengths with measured plasmon resonances (see Fig. 1), it is considered that Ag particles of 10 nm in diameter are grown at a heat treatment temperature of 450 °C and the Ag particle diameter increases up to 34 nm at a heat treatment temperature of 530 °C. For particles below around 10 nm, quantum confinement effects cause to an additional size dependence of complex dielectric function of the silver [24].

With increasing Br content, a difference in resonance wavelength has almost not occurred (see also the inset with higher magnification shown in the lower right part of the image). Hence, the simulation of the plasmon resonance peak position shows that the plasmon resonance frequency is very sensitive to the particle size, but not to the Br concentration in the matrix. The influence of the bromide, especially in the measured concentrations, on the refractive index of the glass is much too small to cause a significant influence.

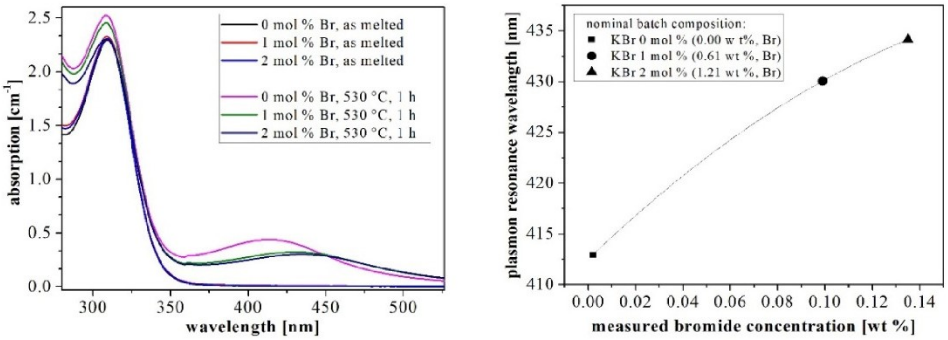

Fig. 4. left: UV-vis absorption spectra of native glass samples and respective irradiated, heat treated samples with different bromide concentrations; right: plasmon resonance peak wavelength position of irradiated and heat treated samples vs. measured bromide concentration (XRF- analyses) of respective samples.

In Ref [14], it was shown that a long wavelength shift of the plasmon resonance is caused by the incorporation of bromide in the glass matrix. Hence in this study, samples were irradiated (180 min, Xe lamp) and heat treated at 530 °C for 1 h and optical absorption spectra were measured. Figure 4 (left) shows the optical absorption spectra of the native glass samples with different bromide concentrations. Furthermore, the respective absorption spectra of irradiated and heat treated samples are shown. The absorption spectra of the as melted glasses are similar for different bromide concentrations in the initial batch composition.

After irradiation and heat treatment, the intensity of the absorption peak maximum at 310 nm, related to the Ce^{3+} [18], is decreasing with increasing bromide concentration. This is an effect of the matrix composition on the redox equlibrium of cerium ions [25]. The position of the silver plasmon resonance absorption peak is shifted to longer wavelengths, from 414 to 433 nm by adding bromide to the initial batch composition. The intensity of the plasmon resonance absorption maximum is decreasing with increasing bromide concentration.

Figure 4 (right) shows the plasmon resonance peak wavelength maximum vs. the measured bromide concentration of the respective samples. The measured bromide concentrations by XRF analyses confirm the high volatility of the bromide (see section 2,). But as already shown in Fig. 3, the influence of the measured Br content to the glass matrix cannot be responsible for the resonance shift. Hence, the shift of the plasmon resonance absorption to longer wavelengths by the addition of bromide indicates the formation of larger Ag particles or by the formation of an AgBr shell around the Ag particles. The formation of such a dielectric shell around silver nanoparticles with a high refractive index leads to a notable wavelength shift of the plasmon absorption band as proposed in Ref [16].

According to Ref [17] where the formation of a dielectric shell of AgBr around the Ag particles is proposed, a simulation of the plasmon resonance peak positions was performed for a single Ag particle surrounded by a dielectric shell of AgBr. The hole core-shell structure was additionally embedded in the glass matrix described by the measured dispersion of the glass. The as calculated positions of plasmon resonance peak maxima for different initial Ag particle diameters are shown in Fig. 5.

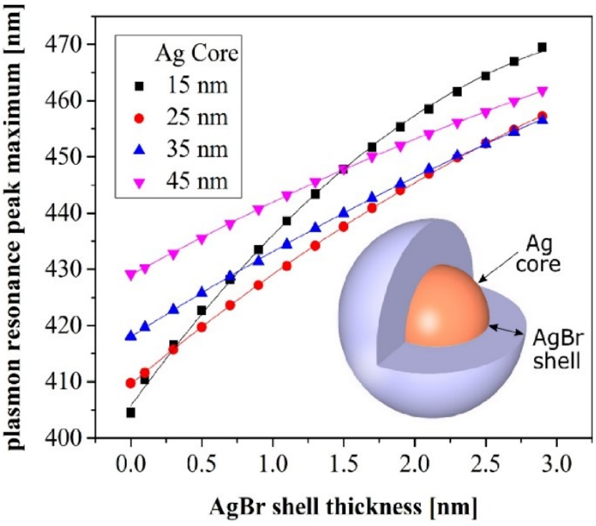

Fig. 5. Simulated plasmon resonance peak positions for single Ag particle with different diameters surrounded by a dielectric AgBr shell of different thickness; in the glass matrix of the current system.

The positions are shown for particles with an Ag core with diameters of 15, 25, 35 and 45 nm and for different AgBr shell thickness in the range from 0.0 to 3.0 nm. The silver core diameter was kept constant and the AgBr shell was added in a certain thickness. Without a dielectric shell, the plasmon resonance peak maximum is, as expected, shifted to longer wavelengths with increasing Ag core diameter. With increasing thickness of the AgBr shell, the plasmonic resonance is shifted to longer wavelength. The slope of the band positions with increasing AgBr shell thickness is nearly the same for particles with a Ag core size of 25, 35 and 45 nm and is nearly linear. If the AgBr shell reaches a thickness of 2.0 nm, the positions of the plasmon resonance peak maxima are slightly different for particles with an Ag core of 25 and 35 nm. Moreover, the plasmon resonance peak maximum positions of a particle with an Ag core of only 15 nm in diameter shows a recognizable larger slope with increasing shell thickness probably caused by the ratio of core diameter to shell thickness. The plasmon resonance peak maximum position increases from a wavelength of 405 nm for an Ag particle without an AgBr shell to a wavelength of 470 nm for an Ag particle with a 3.0 nm AgBr shell and a core diameter of 15 nm. The high refractive index of AgBr (n = 2.2) leads for very thin shell dimension to the observed notable shift of the plasmon resonance peak position towards higher wavelengths.

Similar glass compositions as well as similar UV and thermal treatment processes leads to similar Ag particle sizes. Hence the strong shift caused by adding KBr to the glass composition, can only be explained by forming a dielectric shell around an Ag particle.

4. Conclusion

The photoinduced formation of Ag nanoparticles in an oxyfluoride glass was investigated. The number of the Ag particles is affected by the irradiation dosage. The heat treatment of irradiated samples leads to the occurrence of a plasmon resonance peak. This peak is shifted to longer wavelengths with increasing temperature of the subsequent thermal treatment. A simulation of the plasmon resonance peak position of a Ag particle with different diameters was performed for this particular glass matrix using Mie theory. Both, experimental and simulation results show, that the plasmon resonance frequency is very sensitive to the particle size. The addition of bromide to the initial batch composition has a significant effect on the spectral position of the plasmon resonance band. The simulation of the plasmon resonace peak position for Ag particles surrounded by a shell of AgBr show the most noticeable spectral red shift for small Ag particles and is further increased with increasing AgBr shell thickness.

Funding

Bundesministerium für Bildung und Forschung, Germany (Wachstumskern Brightlas, 03WKCF3E)

4. Discussion

4.1 Chosen base glass system and its modification

Glasses within the system $Na_2O/K_2O/CaO/CaF_2/Al_2O_3/ZnO/SiO_2$ were chosen for the adaption of the photo-thermal process. These glasses showed in previous studies the ability to form nanocrystals with a narrow size distribution during thermal treatment [26] via an interface-controlled crystallisation mechanism [59]. Glasses with the mol% composition (63-x) SiO_2- x Al_2O_3- 12.3 CaO- 5.3 K_2O- 9.0 Na_2O- 10.4 CaF_2 with x = (10, 8, 6) were melted and respective samples were thermally treated described in **article 3.4**.

The Al_2O_3 concentration was varied because oxyfluoride glasses, which have shown the ability to incorporate rare earth ions in the precipitated nanocrystalline phase, possess usually high Al_2O_3 concentrations [45]. Additionally, it is reported that the Al_2O_3 concentration has a major effect on the refractive index change in conventional PTR glass [145].

For the purpose to adapt the photo-thermal process with successful refractive index change and further to incorporate rare earth ions in the crystalline CaF_2 phase which is attractive for photonic applications, different glass compositions were studied. A detailed investigation by thermal analyses and investigation of the microstructure by electron microscopy (SEM and TEM) of the as casted base glasses and the thermally treated glasses is presented in **article 3.4**. The as casted glass with composition $x = 10$ is completely opaque which is due to a phase separation by a fluorine rich amorphous phase as it was proven by XRD analysis. The glasses with the compositions $x = 8, 6$ are clear and visually transparent. The turbidity of the glasses is decreasing while the transparency is increasing with decreasing Al_2O_3 concentration (Fig. 1, **article 3.4**). Hence, optical quality of the as casted glasses is increasing with decreasing Al_2O_3 concentration. The transformation temperatures determined from the DSC compared with values from the dilatometry remains nearly constant for all glasses within the limits of error (± 5 K) (Tab. 2, **article 3.4**). Nevertheless, the T_g for glass $x = 10$ is only 10 K higher in comparison to the other compositions. The crystallisation temperature Tc decreases with increasing Al_2O_3 concentration, which at a first glance appears surprising. From a homogeneous glass, it is expected that usually the tendency towards crystallisation decreases with increasing Al_2O_3 concentration. The behaviour of T_g and Tc is a result of two effects. First, the higher tendency to phase separation could be explained by increasing F concentration bonded to Al with increasing Al_2O_3 concentration [189]. Five and six-fold coordinations can be assumed due to the presence of fluorine [190]. The formation of more Al-F sites leads to an increase of network connectivity due to the reduced number of non-bridging oxygens (NBOs) which also results in an increase in T_g [191]. Moreover, Al is predominantly incorporated in four-fold coordination, i.e. as AlO_4^- tetrahedron, since in the studied glasses the molar concentration of Al_2O_3 is much smaller than those of network modifiers. Hence, increasing Al_2O_3 concentration leads to increasing network connectivity. Thus, a higher Al_2O_3 concentration should lead to increasing viscositiy and a higher T_g [192, 193]. However, this is superimposed by the second effect, the phase separation which is observed in the scanning electron microscope (SEM) (see 5 a in **article 3.4**), which leads to the enrichment of Ca and F and possibly also Al in the droplet phase. An enrichment of Ca and F, which are the components of the crystallising phase, drives the crystallisation to lower temperatures as it was also proven by XRD analyses of heat treated samples from 560 to 620 °C (Fig. 3, **article 3.4**). The crystal sizes remain to be constant between 10 and 38 nm which was estimated using Scherrer`s equation (Tab. 3, **article 3.4**).

The occurrence of phase separation in the initial stages of the crystallisation were observed from the slope of transformation temperature T_g (DSC) vs. heat treatment time. The samples heat treated at 580 °C show a slight drop of T_g for short heat treatment times (< 1 h, inset of Fig. 2, **article 3.4**). With increasing time of thermal treatment, T_g increases and finally reaches nearly the supplied temperature of thermal treatment. The unwanted effect of phase separation was also reported in the literature for the NaF PTR glass and was suppressed by the addition of KBr to the initial batch composition [139], which has a major effect on the photosensitivity of the PTR glass [146] and is discussed later in sections 4.4.4 and 4.5.3 in terms of **articles 3.1 and 3.5**.

The crystallisation behaviour of the studied glasses is similar to the mechanism of nano crystallisation previously described in the literature [59, 96]. During the course of the crystallisation, the viscosity and hence also T_g around the growing nuclei increases until the crystallisation is frozen in if T_g of the residual glass phase reaches the supplied heat treatment temperature [26]. A schematic representation of the proposed nano crystallisation mechanism is illustrated in Fig. 9, **article 3.4**. The observed effects can be explained as follows: (i) the as casted glass is already phase separated. (ii) During nucleation and crystallisation inside the droplets or at the droplet/matrix interface, other network modifiers, such as Na^+ and K^+ are shoved away from the crystallisation front and may diffuse out of the droplets. Since these are network modifying ions and hence the fastest diffusing species, this will lead quickly to a decrease in the viscosity of the matrix phase. (iii) During ongoing crystallisation, Ca^{2+} as well as F^- must further diffuse from the matrix to the droplets. Since this results in a depletion of the matrix phase in Ca^{2+} and F^-, the viscosity increases. This leads to a deceleration of the crystal growth, i.e. the crystals do not exceed the size of the initial droplet phase. The growth of the spherical particles, i.e. droplet phase separation, during heat treatment is also observed in the micrographs. A liquid/liquid phase separation as a precursor stage of crystallisation is preferred because the interfacial energy between two glassy phases is much lower than that between a glassy and a crystalline phase [194]. Hence, the kinetic hindrance of the crystallisation is much larger than that of the phase separation.

4.2. Adaption of the photo-thermal process

For the development of a new photo-thermo-refractive glass based on the glass system $Na_2O/K_2O/CaO/CaF_2/Al_2O_3/ZnO/SiO_2$, the glass was doped with Ag_2O, CeO_2, SnO_2, Sb_2O_3 and KBr. A glass composition based on the composition previously studied with 3.7 mol% Al_2O_3 was chosen [26] due to the proof of nanocrystallisation and as it was shown, the lower tendency to phase separation. The main glass composition is 59.6 SiO_2•12.0 CaO•9.3 Na_2O•8.4 CaF_2•5.4 K_2O•3.7 Al_2O_3•0.7 ZnO•1.0 KBr, doped with 0.02 Ag_2O, 0.02 CeO_2, 0.02 SnO_2, 0.04 and Sb_2O_3 (mol%). All prepared glasses were homogeneous and transparent to the naked eye. The parameters for the thermal treatment are based on results of previous studies [26, 73]. A schematic representation of the adapted photo-thermal process to CaF_2 PTR glass is illustrated in Figure 4.

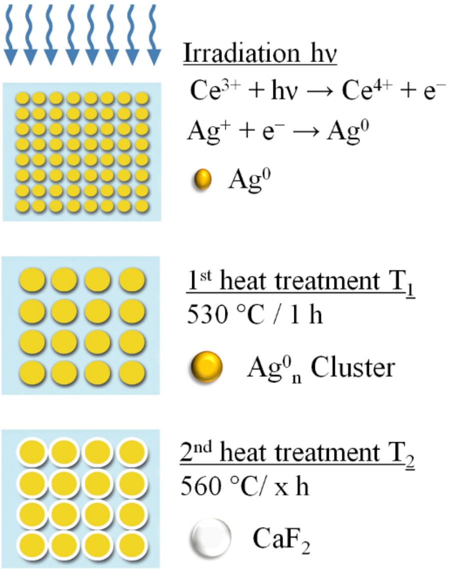

Figure 4 *Schematic representation of the photoinduced crystallisation process in a CaF_2 PTR glass*

4.3. Photoionization

The photoreaction is the initial process of the heterogeneous crystallisation of CaF_2 resulting in a refractive index change. The knowledge on the nature of the photo process involving Ce, Ag, Sn and Sb is essential for the optimization. First, the focus is on the excitation of the cerium by UV-light (Eq. 8).

$$Ce^{3+} + h\nu \rightarrow Ce^{4+} + e^{-} \qquad (8)$$

Detailed UV-vis spectroscopic studies were performed to investigate the spectral components of the cerium and are presented in **article 3.2**. The absorption spectrum of the homogeneous and transparent CaF_2 PTR glass shows high absorptions at wavelengths < 275 nm with a shoulder at 310 nm (Fig. 1, **article 3.2**). According to the literature on conventional NaF PTR glasses, the high absorption in the UV range < 275 nm is due to the combination of absorptions of the components Sb^{3+}, Sn^{2+}, Ag^{+} and Ce^{4+} [131, 195]. The absorption band with a maximum at 310 nm is related to the Ce^{3+} absorption and sensitizes the glass to UV light. However, the high amount of fluoride in the CaF_2 PTR glass causes low polarisability and comparatively low optical basicity [162] which leads to a shift of the redox equilibrium to the reduced state, i.e. to Ce^{3+} (Eq. 9) [161].

$$4Ce^{4+} + 2O^{2-} \leftrightarrow 4Ce^{3+} + O_2 \qquad (9)$$

The theoretical optical basicity was calculated with the averaged experimentally determined or calculated basicity values for the oxides and fluorides of Duffy and Lebouteiller/Courtine [162, 196] to be $\lambda_{theo} = 0.59$. This value leads to the assumption that the Ce^{3+}/Ce^{4+} redox equlibrium is shifted to the reduced state. Furthermore, the Ce^{3+}/Ce^{4+} ratio is influenced by the melting conditions [156] and is further discussed in **article 3.2**. Hence, if the glass is melted under reducing conditions (Ar atmosphere and Ar bubbling), most cerium is expected to be reduced to Ce^{3+}. To understand the effect and behaviour of the cerium during the photo process, the optical absorption bands caused by Ce^{3+} and Ce^{4+} ions were investigated in detail by the deconvolution of the absorption spectra using Gaussian functions. Previous studies wanted to achieve a deconvolution of the spectra by a minimum number of gaussian functions [131, 133]. For this approach, they independently extracted the bands of the Ce^{3+} and Ce^{4+} by using a mathematical combination of various spectra in all wavelength ranges. The deconvolution of the absorption spectra of the CaF_2 PTR glass described in detail in **article 3.2** is based on a physical model and confirms the role of the Ce^{3+} as important photosensitizer due to its electron donation ability by electronic excitation from the 4f to the 5d shell. The deconvolution of the absorption spectrum of the CaF_2 PTR glass only doped with CeO_2 and melted under reducing conditions was fitted with seven Gaussian functions (Fig. 3, **article 3.2**) according to Refs [150, 156]. The deconvoluted bands are characterized by the peak wavenumber, ν_p, the full width at half maximum, FWHM, and the intensity. The five bands in the range from 350 to 200 nm with a constant moderate bandwidth are attributed to the 4f-5d transition of Ce^{3+}. The two broader absorption bands represent the charge transfer (CT) transitions of the Ce^{4+} ions. The addition of these broad absorption bands for the CT transition indicates that a complete shift of the redox equilibrium to the reduced state was not possible. This means, not every cerium ion can provide an electron for the photoreduction of the Ag^{+}. The same deconvolution procedure was applied to the absorption spectrum of the glass melted under non-reducing conditions before (Fig. 4, **article 3.2**) and after irradiation (Fig. 5, **article 3.2**). The bands of Ce^{3+} and Ce^{4+} obtained from the deconvolution of the absorption spectrum of the reduced sample have been added at the same spectral positions under the assumption that the absorption of the photoionized Ce^{3+} (Ce^{3++}) is identical to Ce^{4+} and no intrinsic colour centers are generated [149, 165]. Generally, the CT transitions of Ce^{4+} have higher intensities than the 4f-5d transition bands of Ce^{3+}. The Ce^{4+} CT transitions are due to an electron transfer from oxygen and fluoride to the cerium ion. The 4f-5d band intensities of the deconvoluted absorption bands are decreased to about 2/3 of the intensities of the reduced glass. By contrast, the Ce^{4+} CT transitions are in the non-reduced glass four times higher than in the reduced glass. After irradiation, the intensities of the Ce^{3+} are decreased and the Ce^{4+} intensities are increased (Fig. 5, **article 3.2**). The deconvolution of the absorption spectrum obtained after irradiation proves the oxidation of Ce^{3+} to Ce^{4+} (see Eq. 8). The slight shift of the five Ce^{3+} absorption bands to lower wavenumbers is due to the generation of Ce^{3++} colour centers which are different from Ce^{4+} (see Eq. 1). The colour centers Ce^{3++} have the same valencies as Ce^{4+}, however, the bond lengths and -angles might be different and rather similar to those of Ce^{3+}.

4.4. Photoreduction and Ag agglomeration

The electrons provided by the photoionization of the Ce^{3+} are trapped by Ag^+ ions. The Ag^+ ions are reduced to neutral Ag^0 atoms (Eq. 10).

$$Ag^{+} + e^{-} \rightarrow Ag^{0} \qquad (10)$$

The initial thermal treatment for 1 h at 530 °C (a temperature close to T_g) results in the agglomeration of the Ag^0 atoms and the formation of nucleation centers in the previously irradiated samples (Eq. 11).

$$nAg^{0} \rightarrow Ag_{n}^{0} \qquad (11)$$

This is indicated by the yellow colour of the sample (see Fig. 1, **article 3.3**) which did not occur in non-irradiated and heat-treated samples. The UV-vis spectrum of the irradiated and heat-treated sample show a characterisic plasmon resonance absorption peak between 410 and 450 nm (Fig. 2, **article 3.1**; Fig. 1, **article 3.3**). This plasmon resonance is not observed in the non-irradiated and heat-treated sample. Hence, the Ag agglomeration is a photosensitive process in the CaF_2 PTR glass matrix.

4.4.1 The role of dopants Sb and Sn on the photo-thermal process

If only cerium and silver were involved in this process, the photoreaction should work without the other dopants, i.e. SnO_2 and Sb_2O_3. This was investigated in detail in **article 3.2**. The development of the UV-vis spectra in a glass without Sn/Sb during irradiation and first heat treatment is in the wavelength range < 350 nm similar to Sn/Sb doped CaF_2 PTR glass (Fig. 8, **article 3.2**). Noteworthy is the missing of the plasmon resonance absorption peak after heat treatment. Thus, no plasmon resonance is observed, all silver occurs in the oxidized state, i.e. is dissolved as Ag^+. In the short wavelength range of the absorption spectra a relative decrease of the band intensity in the Sn/Sb free glass after irradiation was observed in comparison to the Sn/Sb containing CaF_2 PTR glass (Fig. 2 and Fig. 8, **article 3.2**). This confirms the occurrence of processes in which Sb and Sn ions are involved. An additional absorption band occurs at around 215 nm [147]. It is assumed that Sn/Sb traps the electrons of the photoionization and that Ag^+ is reduced to Ag^0 due to the loss of trapped photo electrons by Sb and Sn ions during the heat treatment (Eq. 12). This was recently confirmed in an EPR study of NaF PTR glass by Magon et al. [134]. The formation of a Sb^{4+} species was revealed (Eq. 4), which confirms the proposed mechanism in Ref. [145]. The concentration of Sb^{3+} ions in the initial glass determines the formation kinetics of silver nanoparticles according to the law of mass action [197].

$$2Ag^{+} + Sb^{3+} \leftrightarrow 2Ag^{0} + Sb^{5+} \tag{12}$$

Additionally, the ratio between Sb and Sn has an noticeable influence on the photo process [142]. Both, Sb and Sn form redox equilibria with cerium in the melt. For Sb, it can be written as Eq. 13

$$Sb^{3+} + 2Ce^{4+} \rightleftarrows Sb^{5+} + 2Ce^{3+} \tag{13}$$

Redox equilibria are always shifted to the oxidized state with decreasing temperature; an effect which strongly depends of the type of redox pair. If two or more redox pairs are present, the equilibrium is shifted with the temperature according to the standard reaction enthalpies, $\Delta H°$, of the respective redox pair. Since the Sb^{3+}/Sb^{5+} redox pair has a notably higher $\Delta H°$ than Ce^{3+}/Ce^{4+} redox pair according to [152, 153], Eq. 9 is shifted to the right during cooling. That means the addition of antimony to the glass composition helps to adjust a higher Ce^{3+}/Ce^{4+} ratio in the glass. Hence, a higher concentration of Ce^{3+} occurs which enables the reduction of higher Ag^{+} concentrations to elemental Ag^{0}.

4.4.2 Influence of UV dosage and temperature

The Ag nanoparticle formation is photosensitive (**article 3.1**), even by small amounts of cerium and requires the presence of antimony and tin (**article 3.2**). During heat treatment, the silver particles grow by aggregation of silver atoms. A certain temperature is necessary to reach a sufficiently large diffusion coefficient for reasonable growth velocities [170]. The Ag particle formation is clearly visible by the characteristic yellow colouration of the CaF_2 PTR glass (Fig. 1, **article 3.3**). The Ag particle formation in the CaF_2 PTR glass was investigated in detail by electron microscopy in **article 3.3** and by UV-vis spectroscopy in **article 3.5** with the assistance of computational simulations.

In the case that the Ag particles are small compared to the wavelength of light, the colour of the glass is determined by the size, shape, volume fraction of the colloidal metal particles as well as the dispersion properties of the glass matrix [173, 198, 199]. For the CaF_2 PTR glass a linear increase of the Ag particle formation with UV dosage is observed (Fig. 1, **article 3.5**) as it was also reported in [177]. The overall shift of 2.3 nm is very low. The colour of the samples is different from NaF PTR glass for respective heat treatments due to the position of the plasmon resonance in longer wavelength range. In contrast to the NaF PTR glass, the Ag particle formation dependent on the heat treatment temperature (Fig. 1, **article 3.5**), is not linear [177]. The overall shift is 16 nm from a wavelength of 407 nm to 423 nm and the Ag nanoclusters grow with increasing heat treatment temperature and change the plasmon resonance frequency as expected.

The linear increase of the plasmon absorption band intensity vs. irradiation time (Fig. 2, article 3.5) indicates that the number of Ag particles grow with UV dosage. With higher UV dosage, more Ce^{3+} is reduced and consequently more electrons are released to reduce Ag^{+} to Ag^{0} which can agglomerate during subsequent heat treatment. At a certain size of the Ag cluster the plasmon resonance intensity decreases and the band is noticeably broadened, which is in agreement with Ref. [198].

4.4.3 Microstructure

The microstructure during the Ag particle formation was investigated by electron microscopy techniques and are presented in **article 3.3**. The microstructure in the (TEM) micrographs (Fig. 2, **article 3.3**) of an irradiated and heat-treated sample (530 °C/1 h) appears inhomogeneous. The observed structures are 20-50 nm in diameter. The dark appearance of these inhomogeneities are due to an increased absorption of the primary electron beam, i.e. a mass thickness-contrast mechanism, and hence indicate a densification of these areas in comparison to the surrounding glass matrix. In the high-angle annular dark field (HAADF) STEM micrograph these structures appear brighter than the surrounding matrix. Since HAADF imaging is based on the inelastic scattering of electrons within the sample and is thus very sensitive to atomic numbers. This suggests a higher average atomic number of these structures in comparison to the glass matrix. The volume density of these structures can be estimated to be ≈ 20-30 % but the calculated volume fraction of Ag in the glass melt is only 0.008 %. Hence, these structures cannot be solely composed of Ag and are associated with a phase separation (see section 4.1). Analysis via STEM-EDXS was not possible due to extensive sample damage by the electron beam. Further, it is assumed that the volume concentration of Ag^{0} is below the detection limit. The proof of colloidal Ag^{0} particle formation after photoionization and heat treatment was given in a PTR glass matrix with 0.5 wt% Ag_2O [175].

4.4.4 Evidence of Ag-AgBr core-shell structure

The addition of bromide to the glass composition has a noticably effect on the photo-thermal process [139]. Especially, it was observed in UV-vis studies (see Fig. 4, **article 3.5**) that the Ag plasmon resonance peak maximum is shifted to longer wavelengths with increasing bromide concentration [146]. As mentioned, the position of the plasmon resonance peak is dependent on the particle shape, size and the refraction index of the matrix surrounding it. The occurrence of a shell with higher refractive index around the silver nanoparticles would explain the long wavelength shift of the plasmon resonance band maximum. For this purpose, a simulation of the Ag plasmon resonance peak position for Ag particle for the glass matrices with the mol% composition (100-x) (60.18 SiO_2•12.12 CaO•9.32 Na_2O•8.46 CaF_2•5.44 K_2O•3.76 Al_2O_3•0.72 ZnO) (x KBr) with $x = 0.0, 1.0, 2.0$, (doped with 0.02 Ag_2O, 0.02 CeO_2, 0.02 SnO_2, 0.04 Sb_2O_3 (mol%)) was performed based on Mie theory (Fig. 3, **article 3.5**). The dispersion of the glasses containing different KBr concentrations was used for the calculation. The dispersion of the glasses was calculated from the measured refractive indices at certain wavelengths according to the Fraunhofer lines (D, d, e, F, g, h) using the Wemple equation (Eq. 14) [200].

$$\frac{1}{n^2(E)-1} = \frac{E_0}{E_d} - \frac{1}{E_0 E_d} * E^2 \qquad (14)$$

The calculated resonance wavelength increases from 407 nm for a particle of 10 nm diameter up to 457 nm for a particle of 60 nm in diameter. By comparison of the simulated plasmon resonance peak wavelengths with the measured plasmon resonances (see Fig. 1 and 3, **article 3.5**), it is considered that Ag particles of 10 nm in diameter have grown at a heat treatment temperature of 450 °C and the Ag particle diameter increases up to 34 nm during a heat treatment temperature of 530 °C. For particles below around 10 nm, quantum confinement effects lead to an additional size dependence of the complex dielectric function of silver [198]. With increasing KBr concentration, a difference in resonance wavelength has almost not occurred. Hence, the simulation of the plasmon resonance peak position shows that the plasmon resonance frequency is very sensitive to the particle size, but not to the Br concentration in the matrix. The influence of the Br, especially in the measured concentrations, on the refractive index of the glass is much too small to cause a significant influence. Furthermore, the measured absorption spectra of the as casted glasses are similar for different bromide concentrations in the initial batch composition (Fig. 4 left, **article 3.5**). After irradiation and heat treatment the position of the silver plasmon resonance peak position is shifted to longer wavelengths from 414 nm to 433 nm by adding bromide (Fig. 4 right, **article 3.5**). The intensity of the plasmon resonance absorption maximum is decreasing with increasing bromide concentration. The influence of the measured Br concentration is not responsible for the wavelength shift. The long-wavelength shift and the decrease of the plasmon resonance band intensity indicates the growth of larger Ag particles or the formation of a AgBr shell around the Ag particles.

4.4.4 Evidence of Ag-AgBr core-shell structure

A simulation of the plasmon resonance peak positions was performed for a single Ag particle surrounded by a dielectric shell of AgBr (Fig. 5, **article 3.5**) according to [181]. The whole core-shell structure was additionally embedded in the glass matrix described by the measured dispersion of the glass. Without a dielectric shell, the plasmon resonance peak maximum is shifted to longer wavelengths with increasing Ag core diameter and is also shifted with increasing AgBr shell thickness by keeping the Ag core diameter constant. The plasmon resonace peak maximum position increases from a wavelength of 405 nm for a particle without AgBr shell to a wavelength of 470 nm for an Ag particle with 3.0 nm AgBr shell and a core diameter of 15 nm. The high refractive index of AgBr ($n = 2.2$) leads for very thin shell dimension to the observed notable shift of the plasmon resonance peak position towards higher wavelengths. Similar glass compositions as well as similar UV and thermal treatment processes lead to similar Ag particle sizes. Hence, the strong shift caused by adding KBr to the glass composition can only be explained by the formation of a dielectric shell around the Ag particle.

4.5 CaF_2 Nanocrystallisation

4.5.1 Evidence of photoinduced crystallisation

Samples without previous irradiation did not show plasmonic resonance bands in the absorption spectra (Fig. 2, **article 3.1**). As already mentioned, Ag cluster formation is photosensitive and these clusters act as nucleation centers for the CaF_2 in a second heat treatment step at a temperature above T_g. After this second heat treatment at 560 °C for 20 h the samples become slightly light scattering, meaning that the overall scattering is increased. The latter is determined by the sum of the scattering at each individual crystal [185]. This translucency of the material is not a real problem for possible applications as, e.g., wavelengths in the near infrared, i.e., 1040 nm, are normally used for writing holograms.

The XRD patterns of non-irradiated samples show a distinct, but weak line related to cubic CaF_2 (Fig. 3, **article 3.1**) after the two-step heat treatment at 530 °C/1 h and 560 °C/20 h. By contrast, the XRD pattern of the irradiated and two-step heat treated sample reveals an intense and narrow peak at $2\theta = 28.4°$ related to cubic CaF_2 (JCPDS file no. 35-0816) (Fig. 4, **article 3.1**). Crystallisation of CaF_2 was not noticeably observed after one-step heat treatment at 560 °C/20 h (Fig. 4, **article 3.1**). Hence, pre-irradiation and a subsequent two-step heat treatment has a distinct effect on the crystallisation behaviour of CaF_2 in the glass matrix. The first step of the thermal process is quite essential; obviously, the formation of Ag nucleation centers is hindered in the absence of the first heat treatment slightly above T_g and hence, the crystallisation of CaF_2 is not triggered.

4.5.2 Influence of UV dosage on crystallisation

The irradiation time has a significant effect on the volume concentration of CaF_2 nanocrystals (Fig. 6, **article 3.1**). Noticeably, longer irradiation times led to an increase of the intensity of the peak at $2\theta = 28.4°$ and the occurrence of a peak at $2\theta = 57.0°$ attributed to cubic CaF_2 due to the formation of a higher number of nucleation centers. The ratio of the intensity of the two peaks at $2\theta = 28.4°$ and $2\theta = 31.7°$ increases by a factor of two after using a twice as long exposure time. It is not clear, if the peak at $2\theta = 31.7°$ is related to the (200) peak of cubic CaF_2 or if it this peak might be due to the occcurence of AgBr which (200)-peak fits well according to JCPDS file no. 06-0438. Since the occcurence of silver in the glass is only 0.04 wt%, the concentration seems to be very small for a peak of comparably high intensity.

4.5.3 Role of bromide on the crystallisation

The peak at 2θ = 31.7° in the XRD patterns (Fig. 4, article 3.1) predominantly occurs in KBr containing CaF_2 PTR glass. Furthermore, the addition of bromide to the initial glass composition is significant for the success of the controlled heterogeneous CaF_2 crystallisation (Fig. 7, **article 3.1**). For a bromide free CaF_2 PTR glass XRD pattern of the colourless non-irradiated samples show distinct lines related to CaF_2 after heat treatment. The homogeneous CaF_2 crystallisation predominantly occurs in the bromide free glass. Furthermore, it is observed that by the addition of bromide the peak intensities for cubic CaF_2 are changed in comparison to the bromide free CaF_2 PTR glass. The peak at 2θ = 47.0° which is normally the 100% peak is attenuated in its intensity or is completely absent. By contrast, the peak at 2θ = 28.4° which is normally of 95% intensity is increased to 100% intensity. From these observations, it can be assumed that the crystal growth mechanism is in the bromide containing glass is different from the bromide free glass.

For the traditional NaF PTR glass, it was observed that the Br concentration has a major influence on the NaF crystallisation and hence on the refractive index change. At a certain Br concentration, the crystallisation peaks occur in the DSC thermograms at lower temperatures for the UV exposed samples compared to unexposed samples. The heterogeneous crystallisation is triggered. Moreover, the difference in refractive indices between unexposed and UV exposed samples reaches a maximum at a certain Br concentration [145, 146]. Additionaly, a drop in the T_g vs. time plot for short heat treatment times (see section 4.1 and Fig. 2, **article 3.4**) was also observed in the Br free NaF PTR glass and disappears with increasing Br concentration [139]. Br^- ions have a larger radius than O^{2-} and F^- ions. Br^- might be incorporated in the coordination spheres of the network modifiers and F^- ions are released, which then can take part in the crystallisation process [145]. The results of the XRF analysis of the Br concentration (Fig. 4 right, **article 3.5**) in the as casted CaF_2 PTR glasses confirmed the high volatility of bromide during the melting process. Hence, the remaining Br concentration is too low to cause a considerable effect in terms of increasing the concentration of "free" F^- ions. An increase of the Br concentration in the initial batch composition would lead to a reduction of Ag^+ ions to Ag^0 in the glass upon melting and form colloids without irradiation [145].

4.5.4 Microstructure

The existence of CaF_2 crystals was confirmed by different electron microscopy techniques and is presented in **articles 3.3** and **3.4**. The SEM micrographs of the fractured and etched surface (HF, 5%) (Fig. 5 a, **article 3.3**) of an irradiated and heat-treated sample show bright spherical particles with diameters up to ca. 300 nm. These particles are not homogeneous (Fig. 5 b, **article 3.3** and Fig. 6, **article 3.4**) and possess a substructure smaller than 50 nm in size. SEM-EDXS analysis showed the enrichment of Ca and F in these particles. The performed EBSD analyses (Fig. 6, **article 3.3**) provides reliable indexing as cubic CaF_2 (pattern 1-3) from elongated crystals rarely observed in the microstructure which could be due to the occurrence of homogeneous crystallisation. From the XRD pattern in Fig. 3, **article 3.1** it can be concluded that homogeneous CaF_2 crystallisation cannot be completely ruled out. The information depth of the inhomogeneous spherical particles is too low to allow reliable indexing and making EBSD scans of these particles useless. The TEM micrographs of this sample (Fig. 7, **article 3.3**) features the cross section through the spherical particles which are clearly inhomogeneous, i.e. polycrystalline which easily explains the low EBSD pattern quality. The crystalline nature was confirmed with dark-field TEM imaging by using only selected, diffracted electrons with the help of an aperture placed in the back-focal plane of the TEM enable to qualitatively image crystalline areas, which then appear bright due to the diffraction. The cross section clearly shows that the particles are not single crystals. Instead, the bright-field image show a microstructure suggesting outward growth from a central point. This is in agreement with the assumption that that the clusters act as heterogeneous nucleation sites. However, the existence of Ag could not be proved in the TEM. The growth mechanism could hence be related to dendritic [140, 201, 202] or spherulitic growth [203]. The mechanism similar to viscous fingering has also been proposed to occur in glasses [204]. The crystalline nature was investigated from a further cross section through a nanoparticle and the selected area diffraction (SAD) patterns obtained in the TEM by restricting the information volume to the circled areas with an appropriate aperture (Fig. 8, **article 3.3**). The SAED pattern from the zone of the particle exhibits circular positioned elongated spots which arise from similarly oriented crystals and could indicate a spherulitic microstructure. By comparison, the SAD pattern of the zone around the particle shows the characteristic halo around the primary central beam confirming the amorphous matrix. The STEM-EDXS element distributions (Figs. 10 and 11, **article 3.3**) are in agreement with the expectations of CaF_2 crystals growing in a glass matrix. The particles are enriched in Ca and F, while the glass matrix mainly contains Si and O as well as Na, K, Al and Zn. However, especially Si, Na, Al and O are also detected in small but not negligible concentrations inside the spheres. Hence, the intercrystalline spaces in the particles probably contain residual glass which would be in agreement with all three growth mechanisms mentioned above. The signals of the dopant elements (Ag, Ce) are either too small or are superimposed by the signals of the glass, or both. The element-dependent detection limit of EDXS usually ranges from 0.5 to 1.0 at%.

4.6. Refractive index change

The production of the CaF_2 PTR glass with the required optical quality was very challenging due to the high volatility of the fluoride (fluoride evaporation 50%, EDXS- and XRF analyses). For the measurement of refractive index changes in the order of magnitude of $\Delta n = 10^{-5}$-10^{-4} a shearing interferometer setup was admitted. In **article 3.2** (Tab. 2) measured refractive index changes are presented. The CaF_2 PTR glass sample was exposed through a mask to UV light (308 nm, excimer laser) with a constant pulse intensity and different dosages. As the values show, permanent refractive index changes in this glass composition can be generated by the precipitation of the CaF_2 nanocrystals.

To achieve a negative refractive index change in the irradiated region of the glass matrix, a number of parameters have to be controlled and must perfectly match: (i) The optical homogeneity of the glass samples is of significant importance [136], (ii) the glass composition has a great influence [142, 143, 145, 146], (iii) the parameter of the irradiation and heat treatment [138, 174, 177, 186]. Thus, the phase separation, which might even occur in the as casted glass, could hinder controlled heterogeneous crystallization and influence refractive index changes. Since the homogeneous crystallization could not be completely ruled out which occurs in all parts of the glass, i.e. the non-irradiated regions, a noticeable difference in refractive indices might be prevented.

5. Summary

This thesis reports on the development of a new type of a photo-thermo-refractive (PTR) glass. A photo-thermo-refractive glass is a homogeneous oxyfluoride glass which is doped with CeO_2, Ag_2O, SnO_2 and Sb_2O_3. A permanent refractive index change is generated by UV irradiation and a subsequent two step thermal treatment due to the formation of nanocrystals in the glass matrix. This enables the production of Volume Bragg Gratings (VBGs) with a periodic arrangement of alternating layers of high and low refractive indices by the usage of a hologram writing technique, e.g. irradiation with two beams of light which show interference [148].

The glass system $Na_2O/K_2O/CaO/CaF_2/Al_2O_3/ZnO/SiO_2$ was chosen, which meets the requirements for a successful adaption of the photo-thermal process. Thus, glasses within this system showed in previous studies the ability to form nanocrystals in the glass matrix during thermal treatment with a narrow crystal size distribution [26, 73]. This leads to glass ceramics with high transparency which makes them attractive for photonic applications. Since the refractive index differences of CaF_2 (1.43) and the glass matrix (1.52) are lower than those in a glass from which NaF (1.32) was crystallized, less undesirable scattering effects are expected and higher differences in refractive index should be possible since a higher amount of CaF_2 is soluble in the glass. Besides, these glass ceramics combine the advantages of an aluminosilicate matrix and the optical features of low phonon fluoride crystals that can be activated by the incorporation of rare-earth ions [45], which might be interesting for further studies, especially with respect to their luminescence behaviour.

Different base glass compositions with varying Al_2O_3 concentrations were under investigation since it was reported that this affects the tendency to crystallisation and hence, the refractive index change [145]. Glass compositions with lower Al_2O_3 concentration proved to be more appropriate due to less turbidity of the as casted glasses and higher transparency. Hence, optical quality of the as casted glasses is increasing with decreasing Al_2O_3 concentration. The loss of transparency is due to an amorphous phase separation by the enrichment of Ca and F in the droplet phase and drives the CaF_2 crystallisation to lower temperatures. This was confirmed by XRD analyses, thermal analyses and different electron microscopy techniques. The higher Al_2O_3 concentration leads to a higher tendency of phase separation which might be explained by increased amount of F bonded to Al [191]. Thermal analyses (DSC) of thermally treated samples confirmed the nanocrystallisation mechanism in this glasses by an interface-controlled crystallisation mechanism [59] which is accompanied by a liquid/liquid phase separation in the initial stage, followed by the nanocrystallisation in the Ca and F enriched droplet phase and limitation of the crystal size by the formation of a diffusion barrier around the droplets.

For the adaption of the photo-thermal process, a glass composition with less Al_2O_3 concentration was chosen since phase separation should be avoided due to the scattering effects and less controllable crystallisation. The parameters of the thermal treatment were chosen due to the results of thermal analyses and XRD studies. After irradiation with UV light, the first thermal treatment is carried out near T_g at 530 °C for 1 h and the second heat treatment at a higher temperature, e.g. 560 °C for 20 h. To control the heterogeneous crystallisation due to light exposure and subsequent thermal development, the details of the proposed mechanism were under investigation.

The photoionization of the cerium ($Ce^{3+} + h\nu \rightarrow Ce^{4+} + e^{-}$) by irradiation with UV light is the initial reaction. The absorption band at 310 nm related to the 4f-5d transitions of the Ce^{3+} sensitises the glass to UV light. To understand the effect and the behaviour of the cerium during the photo process, the optical absorption bands caused by spectral components of the cerium were investigated by a detailed UV-vis spectroscopic study based on a physical model. The absorption spectra were deconvoluted by using Gaussian functions. In contrast to Refs. [131, 132], the result is an envelope of five bands related to the 4f-5d transitions of the Ce^{3+} and two bands related to the charge transfer (CT) transitions of the Ce^{4+}. The results confirm the role of the cerium as important photosensitizer due to its electron donation ability by electronic excitation from the 4f to the 5d shell. Furthermore, even the low optical basicity of the glass and reducing melting conditions did not totally shift the Ce^{3+}/Ce^{4+} redox equilibrium to the reduced state which would provide a higher number of electrons for the Ag^{+} reduction. The reduction of Ag^{+} to Ag^{0} by the released electrons is the next step in the process ($Ag^{+} + e^{-} \rightarrow Ag^{0}$). Moreover, the presented UV-vis spectroscopic studies confirm the proposed mechanism [145] in which the released electrons are first trapped by Sb^{5+} ions and subsequently trapped by the Ag^{+} ions in the initial thermal treatment at 530 °C/1 h when additionally the Ag^{0} agglomerates ($nAg^{0} \rightarrow Ag_n^{0}$). This is observed by the occurrence of the characteristic yellow colouration due to the silver plasmon resonance in the absorption spectra, which only occurs in previously irradiated samples. In agreement with the literature [177], plasmon resonance absorption bands indicate a linear increase of the Ag particle formation with UV dosage. Ag particles grow with increasing heat treatment temperature but in contrast to traditional PTR glass, Ag particle formation vs. heat treatment temperature is not linear. Computational simulations of the Ag plasmon resonance peak positions were performed based on Mie theory and give evidence of the formation of a whole Ag-AgBr core/shell structure in the CaF_2 PTR glass matrix. These particles act as nucleation centers for the CaF_2 nanocrystallisation in the second heat treatment at 560 °C. The evidence of the photoinduced crystallisation is given by

XRD results. The necessity of a two-step thermal treatment process was proved. In the absence of the first heat treatment step, nucleation centres cannot be generated and heterogeneous CaF_2 crystallisation is hindered. The increase of CaF_2 volume density with irradiation time indicates the formation of a higher number of nucleation centres which is in agreement with UV-vis spectroscopic studies of Ag particle formation. The addition of bromide to the initial batch composition is essential for the photosensitivity which is also reported for the NaF PTR glass [139, 146]. The addition of bromide drives the heterogeneous crystallisation in the CaF_2 PTR glass but homogeneous crystallisation cannot be completely ruled out. The investigation of the microstructure during heat treatment by different electron microscopy techniques gives evidence of CaF_2 crystallisation. Noticeably is the inhomogeneous microstructure, e.g. polycrystallinity, of the spherical particles observed in the SEM and TEM which does not enable to reliable index cubic CaF_2 by EBSD analysis. The crystalline nature was confirmed with dark-field TEM imaging. The cross-section of a particle in the bright-field TEM micrograph also clearly shows an inhomogeneous microstructure and suggests outward growth from a central point which is in agreement with the concept that the cluster act as nucleation centres. Additionally, the SAED pattern of a particle cross-section exhibit circular positioned elongated spots which arise from similarly oriented crystals and could indicate a spherulitic microstructure. This is supported by STEM-EDXS results which show the enrichment of Ca and F in the particles and Si, Na, Al and O in the intercrystalline spaces.

Refractive index changes were generated in the glass in the order of magnitude of $\Delta n = 10^{-5}$ to 10^{-4}. A reliable generation of refractive index changes which makes this material suitable for standard hologram recording could be obtained by more detailed thermal characterisation of the crystallisation process in terms of the glass composition and an optimisation of the irradiation process.

6. Zusammenfassung

Diese Dissertation handelt von der Entwicklung eines neuen Typs eines „photo-thermo-refractive“ (PTR) Glases. Ein PTR Glas ist ein homogenes Oxyfluoridglas, das mit CeO_2, Ag_2O, SnO_2 und Sb_2O_3 dotiert ist. Durch UV-Bestrahlung und anschließender zweistufiger thermischer Behandlung wird eine permanente Brechzahländerung durch die Ausscheidung von Nanokristallen aus der Glasmatrix erzeugt. Dies ermöglicht die Herstellung von Volumen-Bragg-Gittern (VBGs), die aus einer periodischen Anordnung höherer und niedrigerer Brechzahlen aufgebaut sind. Die Strukturierung der Brechzahlen wird erreicht durch die Verwendung einer Hologramm-Schreibtechnik, d.h. durch die Bestrahlung mit zwei kohärenten Lichtstrahlen einer Wellenlänge, die Interferenz zeigen [148].

Es wurde das Glassystem $Na_2O/K_2O/CaO/CaF_2/Al_2O_3/ZnO/SiO_2$ gewählt, das die Voraussetzungen für eine erfolgreiche Anpassung des photothermischen Prozesses erfüllt. So zeigten Gläser in diesem System in früheren Studien die Fähigkeit, während der thermischen Behandlung, Nanokristalle aus der Glasmatrix mit einer engen Kristallgrößenverteilung auszuscheiden [26, 73]. Dies führt zu Glaskeramiken mit hoher Transparenz, welche daher für photonische Anwendungen sehr attraktiv sind. Da die Brechzahlunterschiede von CaF_2 (1.43) und der Glasmatrix (1.52) niedriger sind als diejenigen in einem Glas, aus dem NaF (1,32) kristallisiert wurde, sind weniger unerwünschte Streueffekte zu erwarten. Zudem sollten höhere Brechzahlunterschiede möglich sein, da eine höhere Menge an CaF_2 im Glas gelöst sein sollte. Des Weiteren kombinieren diese Glaskeramiken die Vorteile einer Aluminosilikatglasmatrix und die optischen Eigenschaften von Fluoridkristallen, die durch den Einbau von Seltenerdionen [45] aktiviert werden können, was für weitere Studien, insbesondere in Bezug auf ihre Lumineszenzeigenschaften, interessant sein könnte.

Es wurden verschiedene Grundglaszusammensetzungen mit variierender Al_2O_3 Konzentration untersucht, da aus der Literatur bekannt ist, dass dies die Kristallisationsneigung und damit die Brechungzahländerung beeinflusst [145]. Glaszusammensetzungen mit niedrigerer Al_2O_3 Konzentration erwiesen sich aufgrund der höheren Transparenz der Gläser als geeignet. Daher nimmt die optische Qualität der gegossenen Gläser mit abnehmender Al_2O_3-Konzentration zu. Die Zunahme der Trübung beruht auf einer amorphen Phasentrennung durch die Anreicherung von Calcium und Fluorid in einer Tröpfchenphase und dies verschiebt die CaF_2-Kristallisation zu niedrigeren Temperaturen. Dies wurde durch XRD-Analysen, thermische Analysen und verschiedene Elektronenmikroskopie-Techniken bestätigt. Die höhere Al_2O_3 Konzentration führt möglicherweise zu einer höheren Tendenz zur Phasentrennung, was durch eine erhöhte Menge an F, welches an Al gebunden ist [191], erklärt werden könnte. Thermische Analysen

(DSC) von thermisch behandelten Proben bestätigten die Nanokristallisation nach einem grenzflächengesteuerten Kristallisationsmechanismus in diesen Gläsern [59], der im Anfangsstadium mit einer Flüssig/Flüssig-Phasentrennung einhergeht, gefolgt von der Nanokristallisation in der mit Calcium und Fluorid angereicherten Tröpfchenphase und Begrenzung der Kristallgröße durch die Bildung einer Diffusionsbarriere um die Tröpfchen an der Grenzfläche zur Restglasmatrix.

Zur Anpassung des photo-thermischen Prozesses wurde eine Glaszusammensetzung mit geringerer Al_2O_3 Konzentration gewählt, da die Phasentrennung aufgrund der Streueffekte und der weniger kontrollierbaren Kristallisation vermieden werden sollte. Die Parameter der thermischen Behandlung wurden aufgrund der Ergebnisse von thermischen Analysen und XRD-Studien ausgewählt. Nach der Bestrahlung mit UV-Licht wird die erste thermische Behandlung in der Nähe von T_g bei 530 °C für 1 h durchgeführt und die zweite folgende Wärmebehandlung bei einer höheren Temperatur, z.B. 560 °C für 20 h. Um die heterogene Kristallisation durch Belichtung mit UV Licht und anschließender thermische Entwicklung zu kontrollieren, wurde der gesamte Prozess im Detail untersucht.

Die Photoionisierung des Cers ($Ce^{3+} + h\nu \rightarrow Ce^{4+} + e^{-}$) durch Bestrahlung mit UV-Licht ist die Ausgangsreaktion. Die Absorptionsbande bei 310 nm, die aus den 4f-5d-Übergängen des Ce^{3+} resultiert, sensibilisiert das Glas für UV-Licht. Um die Wirkung und das Verhalten des Cers während des Photoprozesses zu verstehen, wurden die spektralen Komponenten der Absorptionsbanden des Cers durch eine detaillierte UV-vis-spektroskopische Untersuchung auf der Basis eines physikalischen Modells untersucht. Die Absorptionsspektren wurden unter Verwendung von Gauß-Funktionen entfaltet. Im Gegensatz zu den Ref. [131, 132] ist das Ergebnis die Entfaltung in fünf Banden, die aus den 4f-5d-Übergänge der Ce^{3+} resultieren und zwei breiten Banden, die sich auf die Ladungstransferübergänge (CT-charge transfer) des Ce^{4+} beziehen. Die Ergebnisse bestätigen die Rolle des Cers als wichtiger Photosensibilisator aufgrund seiner Elektronendonorfähigkeit durch elektronische Anregung von der 4f zur 5d-Schale. Darüber hinaus verschob auch die geringe optische Basizität des Glases und die reduzierenden Schmelzbedingungen das Ce^{3+}/Ce^{4+} Redox-Gleichgewicht nicht vollständig zum reduzierten Zustand, was eine höhere Anzahl von Elektronen für die Ag^{+} Reduktion bedeuten würde. Die Reduktion von Ag^{+} zu Ag^{0} durch die freigesetzten Elektronen ist der auf die Photoionisation folgende Schritt des Prozesses ($Ag^{+} + e^{-} \rightarrow Ag^{0}$). Darüber hinaus bestätigen die resultierenden UV-vis-spektroskopischen Untersuchungen den vorgeschlagenen Mechanismus [145], bei dem die freigesetzten Elektronen zuerst von Sb^{5+} Ionen aufgenommen werden und anschließend auf die Ag^{+} Ionen bei der anfänglichen thermischen Behandlung bei

530 °C/ 1 h übertragen werden, wenn folglich das Ag^0 agglomeriert ($nAg^0 \rightarrow Ag_n^0$). Dies wird charakterisiert durch das Auftreten einer Gelbfärbung, die auf der Plasmonenresonanz des Silbers beruht, die nur in zuvor belichteten Proben in den UV-vis Spektren auftritt. In Übereinstimmung mit der Literatur [177] zeigen Plasmonresonanzabsorptionsbanden eine lineare Erhöhung der Ag-Partikelbildung mit der UV-Dosis der Belichtung. Ag-Partikel wachsen mit zunehmender Wärmebehandlungstemperatur, aber im Gegensatz zu herkömmlichem PTR-Glas ist der Verlauf der Ag-Partikelbildung zur Wärmebehandlungstemperatur nicht linear. Computersimulationen der Ag-Plasmonresonanz-peakpositionen wurden auf der Grundlage der Mie-Theorie durchgeführt und belegen die Bildung einer vollständigen Ag-AgBr-Kern/ Hülle Struktur in der CaF_2 PTR Glasmatrix. Diese Partikel wirken als Keimbildungszentren für die CaF_2 Nanokristallisation im zweiten Wärmebehandlungsschritt bei 560 °C. Der Nachweis der photoinduzierten Kristallisation wird mittels XRD-Ergebnisse geliefert. Ebenso wurde die Notwendigkeit eines zweistufigen thermischen Behandlungsprozesses bewiesen. In Abwesenheit des ersten Wärmebehandlungs-schrittes können keine Nukleationszentren erzeugt und eine heterogene CaF_2 Kristallisation wird verhindert. Die Erhöhung der CaF_2 Kristallvolumendichte mit der Bestrahlungszeit ist konform mit der Bildung einer höheren Anzahl von Nukleationszentren, was mit UV-vis-spektroskopischen Untersuchungen der Ag-Partikelbildung übereinstimmt. Die Zugabe von Bromid zu der Ausgangsglaszusammensetzung ist für die Photosensibilität wesentlich, wie es auch für das NaF PTR-Glas publiziert ist [139, 146]. Die Zugabe von Bromid erhöht die heterogene Kristallisation im CaF_2 PTR Glas, aber die homogene Kristallisation kann nicht vollständig ausgeschlossen werden. Die Untersuchung der Mikrostruktur während der Wärmebehandlung durch verschiedene Elektronenmikroskopietechniken belegt die Kristallisation von CaF_2. Bemerkenswert ist die inhomogene Mikrostruktur, d.h. die Polykristallinität, der im SEM und TEM beobachteten sphärischen Partikel. An diesen ist wiederum keine zuverlässige Indizierung von kubischem CaF_2 durch EBSD-Analyse nicht möglich. Die Kristallinität wurde Dunkelfeld-TEM Bildgebung bestätigt. Der Querschnitt eines Teilchens in den Hellfeld-TEM Aufnahmen zeigt auch deutlich eine inhomogene Mikrostruktur und lässt auf ein nach aussen gerichtetes Wachstum ausgehend von einem zentralen Punkt schliesssen, der mit dem Konzept übereinstimmt, dass die Ag Cluster als Keimbildungszentren fungieren. Zusätzlich weist das SAED-Muster eines Teilchenquerschnitts kreisförmig positionierte längliche Flecken auf, die aus ähnlich orientierten Kristallen entstehen und eine spherulitische Mikrostruktur anzeigen könnten. Dies wird durch STEM-EDXS-Ergebnisse

unterstützt, die die Anreicherung von Ca und F in den Partikeln und Si, Na, Al und O in den zwischenkristallinen Räumen zeigen.

Brechzahländerungen wurden im Glas in der Größenordnung von $\Delta n = 10^{-5}$ bis 10^{-4} erzeugt. Eine zuverlässige Erzeugung von Brechzahländerungen, die dieses Material für eine standardisierte holografische Strukturierung geeignet macht, könnte durch eine detailliertere thermische Charakterisierung des Kristallisationsverfahrens hinsichtlich der Glaszusammensetzung und einer Optimierung des Bestrahlungsprozesses erhalten werden.

7. Abstract

Glasses in the system $Na_2O/K_2O/CaO/CaF_2/Al_2O_3/ZnO/SiO_2$ show the ability to precipitate nanocrystalline CaF_2 in the glass matrix via a surface-controlled crystallisation accompanied by a phase separation. The Al_2O_3 concentration affects the phase separation in the glass and with decreasing Al_2O_3 concentration the opacity of the glass decreases and the optical quality is increased. For the development of a new type of photo-thermo-refractive (PTR) glass, the adaptation of the photo-thermo-refractive process was adapted to this glass system by doping with CeO_2, Ag_2O, SnO_2, Sb_2O_3, KBr and the perfomance of UV exposure and two-stage temperature treatment. The cerium sensitises the glass to UV light due to its electron donor capability. The decomposition of the absorption bands of the core on the basis of a physical model using Gaussian functions results in an envelope of 5 + 2 bands. The low optical basicity of the base glass and additionally strongly reducing melting conditions could not completely shift the Ce^{3+}/Ce^{4+} redox equilibrium to Ce^{3+}. Antimony has a crucial role as an electron transfer agent in the reduction of the Ag^+ to Ag^0 in the first heat treatment step. The formation of elemental Ag is photosensitive only in the presence of Sb^{5+} ions in the glass. In the first heat treatment step, the Ag^0 agglomerates in the previously exposed areas. A characteristic yellow coloration occurs due to the silver plasmon resonance. Computer simulations of the Ag-plasmon resonance peak positions based on the Mie theory prove the formation of a complete Ag-AgBr core/shell structure of the particles. The Ag/AgBr particle formation depends on the exposure time and the temperature and act as nucleating centers for the heterogeneous CaF_2 crystallisation, which is photosensitive only in the presence of bromide. The volume density of the CaF_2 crystalls increases with the exposure time. The CaF_2 nanocrystals, which are up to a size of 300 nm in diameter, have an inhomogeneous polycrystalline microstructure which suggests an outward growth from a center. Refractive index changes were generated in the glass on the order of $\Delta n = 10^{-5}$ to 10^{-4}.

8. References

1. G. Bonati (2010) *Prospects for the Diode Laser Market* Laser Technik Journal **7**(2):37-42

2. H. Fritsche, R. Koch, B. Krusche et al. (2013) *Generating a high brightness multi-kilowatt laser by dense spectral combination of VBG stabilized single emitter laser diodes* Report, DirectPhotonics Industries Berlin

3. V.A. Borgman, L.B. Glebov, N.V. Nikonorov et al. (1989) *Photothermorefractive Effect in Silicate-Glasses* Dokl. Akad. Nauk. Sssr+ 309(2):336-339

4. L.B. Glebov, N.V. Nikonorov, Y.I. Panysheva et al. (1990) *Multichromatic Glasses - a New Material for Recording of Volumetric Phase Holograms* Dokl. Akad. Nauk. Sssr+ 314(4):849-853

5. O.M. Efimov, L.B. Glebov, V.I. Smirnov (2000) *High-frequency Bragg gratings in a photothermorefractive glass* Opt. Lett. 25(23):1693-1695.

6. N.F. Borrelli (1985) *Integral photosensitive optical device and method* US Patent No. 541,053

7. L.B. Glebov, N.V Nikonorov, G.T. Petrovskii et al. (1990) *A New Method of Hologram Recording in Planar Wave-Guides on Glasses* Dokl. Akad. Nauk. Sssr+ 312(4):852-854

8. S. Hengesbach (2014) *Spektrale Stabilisierung und inkohärente Überlagerung von Diodenlaserstrahlung mit Volumenbeugungsgittern* PhD Thesis, Faculty of Mechanical Engineering, RWTH Aachen University

9. D.S. Starodubov, V. Grubsky, J. Feinberg et al. (1997) *Bragg grating fabrication in germanosilicate fibers by use of near-UV light: A new pathway for refractive-index changes.* Opt. Lett. 22(14):1086-1088

10. M. Zeller, T. Lasser, H.G. Limberger et al. (2005) *Uv-induced index changes in undoped fluoride glass* J. Lightwave Technol. 23(2):624-627

11. D. Grobnic, S.J. Mihailov, C.W. Smelser et al. (2006) *Femtosecond laser fabrication of Bragg gratings in borosilicate ion-exchange waveguides* Ieee Photonic. Tech. L. 18(13-16):1403-1405

12. C. Voigtlander, D. Richter, J. Thomas et al. (2011) *Inscription of high contrast volume Bragg gratings in fused silica with femtosecond laser pulses* Appl. Phys. A-Mater. 102(1):35-38.

13. V.I. Smirnov, J. Lumeau, S. Mokhov et al. (2010) *Ultranarrow bandwidth moire reflecting Bragg gratings recorded in photo-thermo-refractive glass* Opt. Lett. 35(4):592-594

14. I.V. Ciapurin, D.R. Drachenberg, V.I. Smirnov et al. (2012) *Modeling of phase volume diffractive gratings, part 2: reflecting sinusoidal uniform gratings, Bragg mirrors* Opt. Eng. 51(5)

15. I.V. Ciapurin, L.B. Glebov, V.I. Smirnov (2006) *Modeling of phase volume diffractive gratings, part 1: transmitting sinusoidal uniform gratings* Opt. Eng. 45(1)

16. L.A. Siiman, J. Lumeau, L. Canioni et al. (2009) *Ultrashort laser pulse diffraction by transmitting volume Bragg gratings in photo-thermo-refractive glass* Opt. Lett. 34(17):2572-2574

17. O. Andrusyak, L. Canioni, I. Cohanoschi et al. (2009) *Cross-correlation technique for dispersion characterization of chirped volume Bragg gratings* Appl. Optics 48(30):5786-5792

18. M. SeGall, V. Rotar, J. Lumeau et al. (2012) *Binary volume phase masks in photo-thermo-refractive glass* Opt. Lett. 37(7):1190-1192

19. D.R. Drachenberg, O. Andrusyak, G. Venus et al. (2013) *Ultimate efficiency of spectral beam combining by volume Bragg gratings* Appl. Optics 52(30):7233-7242

20. O. Andrusyak, V. Smirnov, G. Venus et al. (2009) *Beam combining of lasers with high spectral density using volume Bragg gratings.* Opt. Commun. 282(13):2560-2563

21. N. Vorobiev, L. Glebov, V. Smirnov (2008) *Single-frequency-mode Q-switched Nd : YAG and Er : glass lasers controlled by volume Bragg gratings* Opt. Express 16(12):9199-9204

22. D. Paboeuf, D. Vijayakumar, O.B. Jensen et al. (2011) *Volume Bragg grating external cavities for the passive phase locking of high-brightness diode laser arrays: theoretical and experimental study.* J. Opt. Soc. Am. B 28(5):1289-1299

23. L.B. Glebov, V.I. Smirnov, E. Rotari et al. (2014) *Volume-chirped Bragg gratings: monolithic components for stretching and compression of ultrashort laser pulses* Opt. Eng. 53(5)

24. A. de Pablos-Martin, A. Duran, M.J. Pascual (2012) *Nanocrystallisation in oxyfluoride systems: mechanisms of crystallisation and photonic properties* Int. Mater. Rev. 57(3):165-186.

25. H. Scholze *Glas- Natur, Struktur und Eigenschaften* 1988 3rd ed., Berlin Heidelberg New York London Paris Tokyo, Springer Verlag

26. C. Rüssel (2005) *Nanocrystallization of* CaF_2 *from* $Na_2O/K_2O/CaO/CaF_2/Al_2O_3/SiO_2$ *glasses* Chem. Mater. 17(23):5843-5847

27. W. Ostwald (1897) *Studien über die Bildung und Umwandlung fester Körper.* Z. Phys. Chem. 22:289-330

28. G. Tammann *Der Glaszustand* 1933, Leipzig, L. Voss

29. J.W.P. Schmelzer, V.M. Fokin, A.S. Abyzov et al. (2010) *How Do Crystals Form and Grow in Glass-Forming Liquids: Ostwald's Rule of Stages and Beyond.* Int. J. Appl. Glass Sci. 1(1):16-26

30. D. Turnbull, M.A. Cohen *Crystallisation kinetics and glass formation*, In: *Modern aspects of the vitreous state*, 1960, Butterworth Inc., Washington DC.

31. J.J. Hammel (1971) *Nucleation in Glass* Am. Ceram. Soc. Bull. 50(4):412

32. I. Gutzow (1980) *Kinetics of Crystallization Processes in Glass Forming Melts* J. Cryst. Growth 48(4):589-599

33. I. Gutzow (1977) *Mechanism of Crystal-Growth in Glass Forming Systems* J. Cryst. Growth 42(Dec):15-23

34. S.D. Stookey (1958) *History of the Development of Pyroceram* Res. Manage. 1(3):155-163

35. G.H. Beall, D.A. Duke (1969) *Transparent Glass-Ceramics* J. Mater. Sci. 4(4):340

36. G.H. Beall (2000) *Glass-ceramics for photonic applications.* Glass Sci. Technol. 73:3-11

37. E.D. Zanotto (2013) *Glass Crystallization Research A 36-Year Retrospective. Part I, Fundamental Studies* Int. J. Appl. Glass Sci. 4(2):105-116

38. A.J. Stevenson, H. Serier-Brault, P. Gredin et al. (2011) *Fluoride materials for optical applications: Single crystals, ceramics, glasses, and glass-ceramics* J. Fluorine Chem. 132(12):1165-1173

39. I. Gugov, M. Müller, C. Rüssel (2011) *Transparent oxyfluoride glass ceramics co-doped with* Er^{3+} *and* Yb^{3+} *- Crystallization and upconversion spectroscopy* J. Solid State Chem. 184(5):1001-1007

40. S. Tanabe, H. Hayashi, T. Hanada et al. (2002) *Fluorescence properties of* Er^{3+} *ions in glass ceramics containing* LaF_3 *nanocrystals* Opt. Mater. 19(3):343-349

41. P.P. Fedorov, A.A. Luginina, S.V. Kuznetsov et al. (2011) *Nanofluorides* J. Fluorine Chem. 132(12):1012-1039

42. C.S. Ma, Q. Jiao, L.J. Li et al. (2014) *Up-conversion luminescence properties and energy transfer of* Er^{3+}/Yb^{3+} *co-doped oxyfluoride glass ceramic containing* CaF_2 *nano-crystals* Chinese Phys. B 23(5)

43. W. Seeber, E.A. Downing, L. Hesselink et al. (1995) Pr^{3+}*-Doped Fluoride Glasses* J. Non-Cryst. Solids 189(3):218-226

44. G.H. Beall (2000) *Glass-ceramics for photonic applications* Glass Sci. Technol. 73:3-11

45. P.P. Fedorov, A.A. Luginina, A.I. Popov (2015) *Transparent oxyfluoride glass ceramics* J. Fluorine Chem. 172:22-50

46. R. Bagga, V.G. Achanta, A. Goel et al. (2013) Dy^{3+}*-doped nano-glass ceramics comprising* $NaAlSiO_4$ *and* $NaY_9Si_6O_{26}$ *nanocrystals for white light generation* Mater. Sci. Eng. B-Adv. 178(3):218-224

47. L.F. Vendramim, K. Zorn, C. Bocker et al. (2010) *Effect of the alkali concentration on the crystallization of* BaF_2 *from* $Na_2O/K_2O/BaF_2/Al_2O_3/SiO_2$ *glasses* J. Non-Cryst. Solids 356(52-54):2999-3003

48. A.A. Cabral, V.M. Fokin, E.D Zanotto (2010) *On the Determination of Nucleation Rates in Glasses by Nonisothermal Methods* J. Am. Ceram. Soc. 93(9):2438-2440

49. V.M. Fokin, A.A. Cabral, R.M.C.V. Reis et al. (2010) *Critical assessment of DTA-DSC methods for the study of nucleation kinetics in glasses* J. Non-Cryst. Solids 356(6-8):358-367

50. S.D. Stookey (1949) *Coloration of Glass by Gold, Silver, and Copper* J. Am. Ceram. Soc. 32(8):246-249

51. E. Kleebusch, C. Patzig, T. Höche et al. (2016) *Effect of the concentrations of nucleating agents ZrO_2 and TiO_2 on the crystallization of Li_2O-Al_2O_3-SiO_2 glass: an X-ray diffraction and TEM investigation* J. Mater. Sci. 51(22):10127-10138

52. K. Thieme, C. Rüssel (2016) *CeO_2 and Y_2O_3 as nucleation inhibitors in lithium disilicate glasses* J. Mater. Sci. 51(2):989-999

53. K. Thieme, C. Rüssel (2015) *The effect of niobium- and tantalum oxide on nucleation and growth kinetics in lithium disilicate glasses* Mater. Chem. Phys. 162:354-363

54. K. Thieme, C. Rüssel (2014) *Nucleation inhibitors-The effect of small concentrations of Al_2O_3, La_2O_3 or TiO_2 on nucleation and crystallization of lithium disilicate* J. Eur. Ceram. Soc. 34(15):3969-3979

55. A. Paul (1990) *Glass Formation by the Sol-gel Process*, In: *Chemistry of Glasses* London New York, Chapman and Hall,

56. S. Cai, W.J. Zhang, G.H. Xu et al. (2009) *Microstructural characteristics and crystallization of CaO-P_2O_5-Na_2O-ZnO glass ceramics prepared by sol-gel method* J. Non-Cryst. Solids 355(4-5):273-279

57. J. Del-Castillo, A.C. Yanes, J. Mendez-Ramos et al. (2010) *Sol-gel preparation and white up-conversion luminescence in rare-earth doped PbF_2 nanocrystals dissolved in silica glass* J Sol-Gel Sci. Techn. 53(3):509-514

58. A. Santana-Alonso, A. C . Yanes, J. Mendez-Ramoset al. (2010) *Sol-gel transparent nano-glass-ceramics containing Eu^{3+}-doped $NaYF^4$ nanocrystals* J. Non-Cryst. Solids 356(18-19):933-936

59. C. Bocker, C. Rüssel, I. Avramov (2013) *Transparent Nano Crystalline Glass-Ceramics by Interface Controlled Crystallization* Int. J. Appl. Glass Sci. 4(3):174-181

60. P.P Fedorov (1997) *Glass formation criteria for fluoride systems* Inorg. Mater. + 33(12):1197-1205

61. H. Rawson (1967) *Inorganic Glass-forming Systems.*, London New York: Academic Press.

62. P.P. Fedorov (1997) *Crystallochemical Aspects of Fluoride-Glass Formation.* Crystallogr. Rep+ 42(6):1064-1075

63. R.W. Hopper, D.R. Uhlmann (1975) *Dependence of Interfacial-Tension on Separation for 2 Regular Solution Interfaces* J. Non-Cryst. Solids 19(Dec):149-165

64. S. Woltz, C. Rüssel (2004) *Self organized nano crystallinity of magnetite precipitated from a 4.9 Na_2O•33.3 CaO•17.1 Fe_2O_3•44.7 B_2O_3 glass* J. Non-Cryst. Solids 337(3):226-231

65. R. Harizanova, I. Gugov, C. Rüssel (2011) *Crystallization of (Fe, Mn)-based nanoparticles in sodium-silicate glasses* J. Mater. Sci. 46(22):7169-7176

66. R. Harizanova, G. Völksch, C. Rüssel (2011) *Crystallization and microstructure of glasses in the system Na_2O/MnO/SiO_2/Fe_2O_3* Mater. Res. Bull. 46(1):81-86

67. T. Höche, M. Mader, S. Bhattacharyya et al. (2011) *$ZrTiO_4$ crystallisation in nanosized liquid-liquid phase-separation droplets in glass-a quantitative XANES study* Crystengcomm 13(7):2550-2556

68. A. Hunger, G. Carl, A. Gebhardt et al. (2008) *Ultra-high thermal expansion glass-ceramics in the system* $MgO/Al_2O_3/TiO_2/ZrO_2/SiO_2$ *by volume crystallization of cristobalite* J. Non-Cryst. Solids 354(52-54):5402-5407

69. A. Hunger, G. Carl, A. Gebhardt et al. (2010) *Young's moduli and microhardness of glass-ceramics in the system* $MgO/Al_2O_3/TiO_2/ZrO_2/SiO_2$ *containing quartz nanocrystals* Mater. Chem. Phys. 122(2-3):502-506

70. A. Hunger, G. Carl, C. Rüssel (2010) *Formation of nano-crystalline quartz crystals from* $ZnO/MgO/Al_2O_3/TiO_2/ZrO_2/SiO_2$ *glasses* Solid State Sci. 12(9):1570-1574

71. T. Höche, C. Patzig, T. Gemming et al. (2012) *Temporal Evolution of Diffusion Barriers Surrounding* $ZrTiO_4$ *Nuclei in Lithia Aluminosilicate Glass-Ceramics* Crystal Growth Des. 12(3):1556-1563

72. C. Patzig, T. Höche, M. Dittmer et al. (2012) *Temporal Evolution of Crystallization in* MgO-Al_2O_3-SiO_2-ZrO_2 *Glass Ceramics* Crystal Growth Des. 12(4):2059-2067

73. R.P.F. de Almeida, C. Bocker, C. Rüssel (2008) *Size of* CaF_2 *crystals precipitated from glasses in the* $Na_2O/K_2O/CaO/CaF_2/Al_2O_3/SiO_2$ *system and percolation theory.* Chem. Mater. 20(18):5916-5921

74. A. Hoell, Z. Varga, V. S. Raghuwanshi et al. (2014) *ASAXS study of* CaF_2 *nanoparticles embedded in a silicate glass matrix* J. Appl. Crystallogr. 47:60-66

75. C. Bocker, I. Avramov, C. Rüssel (2010) *Viscosity and diffusion of barium and fluoride in* $Na_2O/K_2O/Al_2O_3/SiO_2/BaF_2$ *glasses* Chem. Phys. 369(2-3):96-100

76. C. Bocker, C. Rüssel (2009) *Self-organized nano-crystallisation of* BaF_2 *from* $Na_2O/K_2O/BaF_2/Al_2O_3/SiO_2$ *glasses* J. Eur. Ceram. Soc. 29(7):1221-1225

77. S. Bhattacharyya, C. Bocker, T. Heil et al. (2009) *Experimental Evidence of Self-Limited Growth of Nanocrystals in Glass* Nano Lett. 9(6):2493-2496

78. C. Bocker, S. Bhattacharyya, T, Höche et al. (2009) *Size distribution of* BaF_2 *nanocrystallites in transparent glass ceramics* Acta Mater. 57(20):5956-5963

79. C. Bocker, J. Wiemert, C. Rüssel (2014) *The effect of viscosity on nanocrystallization of strontium fluoride from a silicate glass* Solid State Sci. 30:55-60

80. C. Bocker, J. Wiemert, C. Rüssel (2013) *The formation of strontium fluoride nano crystals from a phase separated silicate glass* J. Eur. Ceram. Soc. 33(10):1737-1745

81. S. Bhattacharyya, T. Höche, N. Hemono et al. (2009) *Nano-crystallization in* LaF_3-Na_2O-Al_2O_3-SiO_2 *glass* J. Cryst. Growth 311(18):4350-4355

82. N. Hemono, G. Pierre, F. Munoz et al. (2009) *Processing of transparent glass-ceramics by nanocrystallisation of* LaF_3 J. Eur. Ceram. Soc. 29(14):2915-2920

83. A. de Pablos-Martin, N. Hemono, G.C. Mather et al. (2011) *Crystallization Kinetics of* LaF_3 *Nanocrystals in an Oxyfluoride Glass* J. Am. Ceram. Soc. 94(8):2420-2428

84. A. de Pablos-Martin, G.C. Mather, F. Munoz et al. (2010) *Design of oxy-fluoride glass-ceramics containing* $NaLaF_4$ *nano-crystals* J. Non-Cryst. Solids 356(52-54):3071-3079

85. A. Herrmann, M. Tylkowski, C. Bocker et al. (2013) *Cubic and Hexagonal* $NaGdF_4$ *Crystals Precipitated from an Aluminosilicate Glass: Preparation and Luminescence Properties* Chem. Mater. 25(14):2878-2884

86. A. Herrmann, M. Tylkowski, C. Bocker et al. (2013) *Preparation and luminescence properties of glass-ceramics containing* Sm^{3+}*-doped hexagonal* $NaGdF_4$ *crystals.* J Mater. Sci. 48(18):6262-6268

87. V.S. Raghuwanshi, A. Hoell, C. Bocker et al. (2012) *Experimental evidence of a diffusion barrier around* BaF_2 *nanocrystals in a silicate glass system by ASAXS* Crystengcomm 14(16):5215-5223

88. C.G. Lin, C. Bocker, C. Rüssel (2015) *Nanocrystallization in Oxyfluoride Glasses Controlled by Amorphous Phase Separation.* Nano Lett. 15(10):6764-6769

89. R. Wurth, F. Munoz, M. Müller et al. (2009) *Crystal growth in a multicomponent lithia aluminosilicate glass* Mater. Chem. Phys. 116(2-3):433-437

90. R. Harizanova, G. Völksch, C. Rüssel (2010) *Microstructures formed during devitrification of* $Na_2O•Al_2O_3•B_2O_3•SiO_2•Fe_2O_3$ *glasses* J. Mater. Sci. 45(5):1350-1353

91. V.S. Raghuwanshi, D. Tatchev, S. Haas et al. (2012) *Structural analysis of magnetic nanocrystals embedded in silicate glasses by anomalous small-angle X-ray scattering* J. Appl. Crystallogr. 45:644-651

92. S. Bhattacharyya, T. Höche, K. Hahn et al., *Various transmission electron microscopic techniques to characterize phase separation - illustrated using a* LaF_3 *containing aluminosilicate glass* J. Non-Cryst. Solids 355(6):393-396

93. A. Mallik, A.K. Barik, B. Pal (2017) *Self-limited growth of* Pr^{3+}*- doped* LaF_3 *nanocrystals in oxyfluoride glass and glassceramics* RSC. Adv. **7**(24):14824-14831

94. J.C. Phillips, M.F. Thorpe (1985) *Constraint Theory, Vector Percolation and Glass-Formation* Solid State Commun. 53(8):699-702

95. M.F. Thorpe (1985) *Rigidity Percolation in Glassy Structures.* J. Non-Cryst. Solids **76**(1):109-116

96. C. Bocker, C. Rüssel, I. Avramov (2012) *Crystal growth in non-isochemical, highly viscous liquids and percolation theory* Chem. Phys. 406:50-54

97. I. Avramov, C. Rüssel, N. Kolkovska et al. (2008) *Crystallization kinetics and network rigidity* J Phys.-Condens. Mat. 20(33):147-153

98. R.J. Collier, C.B. Burckhardt, L.H. Lin (1971) *Hologram recording materials*, In: *Optical Holography*, Academy Press, New York

99. P. Hariharan, *Optical Holography, principles, techniques and applications*. 2nd edition ed. 1996: Cambridge University Press, Cambridge, UK

100. J. W. Mitchell (1999) *Evolution of the concepts of photographic sensitivity* J. Imaging Sci. Techn. 43(1):38-48

101. B.A. Kowalski, R.R. McLeod (2016) *Design concepts for diffusive holographic photopolymers* J. Polym. Sci. Pol. Phys. 54(11):1021-1035

102. W.H. Armistead, S.D. Stookey (1964) *Photochromic Silicate Glasses Sensitized by Silver Halides - Their Characteristic of Changing Color Reversibly in Combination with Other Properties Suggests Many Uses* Science 144(361):150-154

103. J.J. Zhang, Q. Zou, H. Tian (2013) *Photochromic Materials: More Than Meets The Eye* Adv. Mater. 25(3):378-399

104. R.J. Araujo (1980) *Photochromism in Glasses Containing Silver-Halides* Contemp. Phys. 21(1):77-84

105. S. Kober, M. Salvador, K. Meerholz (2011) *Organic Photorefractive Materials and Applications* Adv. Mater. 23(41), 4725-4763

106. G. Montemezzani, C. Medrano, M. Zgonik et al. (2000) *Nonlinear Optical Effects and Materials*. Springer series in optical Science, Springer, Berlin, Heidelberg, New York

107. K.M. Johnson, L. Hesselink, J. W. Goodman (1984) *Holographic Reciprocity Law Failure* Appl. Optics 23(2):218-227

108. T. Tani 1995 *The Present Status and Future-Prospects of Silver-Halide Photography* J. Imaging Sci. Techn. 39(1):31-40

109. N.N. Alyatina, V.A. Zhukova, V.V. Ivakhnik et al. (1989) *Real-Time Recording of Holograms on Photochromic-Glasses* Sov. J. Opt. Technol+ 56(12):756-757

110. N. Korneev, H. Veehuis, K. Buse et al. (2001) *Thermal fixing of holograms and their electrically assisted development in barium calcium titanate crystals* J. Opt. Soc. Am. B 18(11):1570-1577

111. S.C. Fu, S.Y. Sun, X.T. Zhang et al. (2014) *Polarization-dependent and rewritable holographic gratings in Ag/TiO_2 nanocomposite films* Opt. Commun. 318:1-6

112. T.H. James, C.E.K. Mees (1977) *The Theory of the photographic process*. 4th ed. New York: Macmillan.

113. M. Ortuno, E. Fernandez, R. Fuentes et al. (2013) *Improving the performance of PVA/AA photopolymers for holographic recording* Opt. Mater. 35(3):668-673

114. A. Ashkin, G.D. Boyd, J.M. Dziedzic et al. (1966) *Optically-Induced Refractive Index Inhomogeneities in Linbo3 and Litao3 - (Ferroelectric Materials - Nonlinear Optics - E).* Appl. Phys. Lett. 9(1):72-74

115. K. Buse, J. Imbrock, E. Krätzig et al. (2006) *Photorefractive Materials and their Applications II: Materials*. Springer Series in Optical Science Berlin: Springer.

116. H. Hatano, Y. Liu, K. Kitamura (2006) *Photorefractive Materials and their Applications II: Materials*. Springer Series in Optical Science Berlin: Springer.

117. V.M.N. Passaro, F. Magno (2007) *Holographic gratings in photorefractive materials: A review* Laser Phys. 17(3):231-243

118. E. Kratzig (1978) *Photorefractive Effects and Photoconductivity in Linbo3-Fe* Ferroelectrics 21(1-4), 635-636

119. K. Buse, F. Jermann, E. Kratzig (1994) *Infrared Holographic Recording in Linbo3 - Cu* Appl- Phys. a-Mater. 58(3):191-195

120. G.H. Beall (2016) *Dr. S. Donald (Don) Stookey (1915-2014): Pioneering Researcher and Adventurer* Front. Mater. 3:1-8

121. S.D. Stookey (1949) *Photosensitive Glass - a New Photographic Medium* Ind. Eng. Chem. 41(4).856-861

122. S.D. Stookey (1950) *Photosensitive Glass* J. Opt. Soc. Am. 40(4):265-266

123. S.D. Stookey, G.H. Beall, J.E. Pierson (1978) *Full Color Photosensitive Glass* J. Appl. Phys. 49(10):5114-5123

124. P. Hofmann, R. Amezcua-Correa, E. Antonio-Lopez et al. (2013) *Strong Bragg Gratings in Highly Photosensitive Photo-Thermo-Refractive-Glass Optical Fiber* Ieee Photonic. Tech. L. 25(1):25-28

125. J. Lumeau, L.B. Glebov (2013) *Effect of the refractive index change kinetics of photosensitive materials on the diffraction efficiency of reflecting Bragg gratings* Appl. Opt. 52(17):3993-3997

126. M.L. Klimov, L.B. Glebov, L. Glebova (2016) *Differentiation of crystalline and amorphous phases in photothermorefractive glass by secondary ion mass spectrometry* J. Vac. Sci. Technol. 34(3)

127. M. L. Klimov, L. Glebova, L. Glebov (2007) *Determination of composition of photo-thermorefractive glass by SIMS* Phys. Chem. Glasses-B 48(5):313-316

128. L. Glebova, D. Ehrt, L.B. Glebov (2007) *Luminescence of dopants in PTR glass* Phys. Chem. B 48(5):328-331

129. V.D. Dubrovin, A.I. Ignatiev, N.V. Nikonorov et al. (2014) *Luminescence of silver molecular clusters in photo-thermo-refractive glasses* Opt. Mater. 36(4):753-759

130. D.A. Klyukin, A.I. Sidorov, A.I. Ignatiev et al. (2014) *Luminescence quenching and recovering in photo-thermo-refractive silver-ion doped glasses* Opt. Mater. 38:233-237

131. A.M. Efimov, A.I. Ignatiev, N.V. Nikonorov et al. (2013) *Quantitative UV-VIS spectroscopic studies of photo-thermo-refractive glasses. II. Manifestations of* Ce^{3+} *and Ce(IV) valence states in the UV absorption spectrum of cerium-doped photo-thermo-refractive matrix glasses* J. Non-Cryst. Solids 361:26-37

132. M.L. Brandily-Anne, J. Lumeau, L. Glebova et al. (2010) *Specific absorption spectra of cerium in multicomponent silicate glasses* J. Non-Cryst. Solids 356(44-49):2337-2343

133. A.M. Efimov, A.I. Ignatiev, N.V. Nikonorov et al. (2011) *Spectral components that form UV absorption spectrum of* Ce^{3+} *and Ce(IV) valence states in matrix of photothermorefractive glasses* Opt. Spectrosc. 111(3):426-433

134. C.J. Magon, J.P.D. Gonzalez, J.F. Lima et al. (2016) *Electron Paramagnetic Resonance (EPR) studies on the photo-thermo ionization process of photo-thermo-refractive glasses* J. Non-Cryst. Solids 452:320-324

135. A.M. Efimov, A.I. Ignatiev, N.V. Nikonorov et al. (2011) *Quantitative UV-VIS spectroscopic studies of photo-thermo-refractive glasses. I. Intrinsic, bromine-related, and impurity-related UV absorption in photo-thermo-refractive glass matrices* J. Non-Cryst. Solids 357(19-20):3500-3512

136. J. Lumeau, A. Sinitskii, L. Glebova et al. (2009) *Method to assess the homogeneity of partially crystallized glasses: Application to a photo-thermo-refractive glass* J. Non-Cryst. Solids 355(34-36):1760-1768

137. V.M. Fokin, G.P. Souza, E.D. Zanotto et al. (2010) *Sodium Fluoride Solubility and Crystallization in Photo-Thermo-Refractive Glass* J. Am. Ceram. Soc. 93(3):716-721

138. J. Lumeau, A. Sinitskii, L. Glebova et al. (2007) *Spontaneous and photo-induced crystallisation of photo-thermo-refractive glass* Phys. Chem. Glass-B 48(4):281-284

139. G.P. Souza, V.M. Fokin, C.A. Baptista et al. (2011) *Effect of Bromine on NaF Crystallization in Photo-Thermo-Refractive Glass* J. Am. Ceram. Soc. 94(9):2906-2911

140. G.P. Souza, V.M. Fokin, E.D. Zanotto et al. (2009) *Micro and nanostructures in partially crystallised photothermorefractive glass* Phys. Chem. Glass-B 50(5):311-320

141. J. Lumeau, V. Smirnov, A. Glebov et al. (2010) *Ultra-narrow bandpass filters based on volume Bragg grating technologies,* In: Photonics in the Transportation Industry: Auto to Aerospace III., Orlando, Florida.

142. E.I. Panysheva, I.V. Tunimanova, V.A. Tsekhomskii (1990) *The role of tin and antimony in the coloring of polychromatic glass.* Fiz Khim Stekla 16(3):7

143. E.I. Panysheva, I.V. Tunimanova (1996) *The role of fluorine ions in the polychromatic process* Glass Phys. Chem. 22(2):125-131

144. H.G. Francois-Saint-Cyr (2001) *Photo-Thermo-Refractive Glasses: Crystallization Mechanism for Optical Applications*, PhD Thesis, University of Central Florida: Orlando

145. N.V. Nikonorov, E.I. Panysheva, I.V. Tunimanova et al. (2001) *Influence of glass composition on the refractive index change upon photothermoinduced crystallization* Glass Phys. Chem. 27(3):241-249

146. L. Glebova, J. Lumeau, M. Klimov et al. (2008) *Role of bromine on the thermal and optical properties of photo-thermo-refractive glass* J. Non-Cryst. Solids 354(2-9):456-461

147. A.M. Efimov, A.I. Ignatiev, N.V. Nikonorov et al. (2015) *Photo-Thermo-Refractive Glasses: Effects of Dopants on Their Ultraviolet Absorption Spectra* Int. J. Appl. Glass Sci. 6(2):109-127

148. J. Lumeau, E.D. Zanotto (2017) *A review of the photo-thermal mechanism and crystallization of photo-thermo-refractive (PTR) glass* Int. Mater. Rev. 62(6):348-366

149. J. S. Stroud (1962) *Color Centers in a Cerium-Containing Silicate Glass* J. Chem. Phys. 37(4), 836-841

150. A. Herrmann, H.A. Othmann, A.A. Assadi et al. (2015) *Spectroscopic properties of cerium-doped aluminosilicate glasses* Opt. Mater. Express 5(4):720-732

151. H.D. Schreiber, H.V. Lauer, T. Thanyasiri (1980) *Oxidation-Reduction Equilibria of Iron and Cerium in Silicate-Glasses - Individual Redox Potentials and Mutual Interactions* J. Non-Cryst. Solids 38-39:785-790

152. C. Rüssel, E. Freude (1989) *Voltammetric Studies of the Redox Behavior of Various Multivalent Ions in Soda-Lime-Silica Glass Melts* Phys. Chem. Glasses, 30(2):62-68

153. A. Paul, R.W. Douglas (1965) *Cerous-Ceric Equilibrium in Binary Alkali Borate and Alkali Silicate Glasses* Phys. Chem. Glasses 6(6), 212-215

154. A. Paul, M. Mulholland, M.S. Zaman (1976) *Ultraviolet-Absorption of Cerium(III) and Cerium(IV) in Some Simple Glasses* J. Mater. Sci. 11(11):2082-2086

155. J.A. Duffy, G.O. Kyd (1966) *Ultraviolet absorption and fluorescence spectra of cerium and the effect of glass composition* Phys. Chem. Glasses 37(2):45-48

156. H. Ebendorff-Heidepriem, D. Ehrt (2000) *Formation and UV absorption of cerium, europium and terbium ions in different valencies in glasses* Opt. Mater. 15(1):7-25

157. M. Stephan, M. Zachau, M. Groting et al. (2005) *A theoretical investigation of 4f -> 5d transition of trivalent rare earth ions in fluorides and complex oxides* J. Lum. 114(3-4):255-266

158. J.L. Rygel, C.G. Pantano, *Synthesis and properties of cerium aluminosilicophosphate glasses* J. Non-Cryst. Solids 355(52-54):2622-2629

159. J.C. Krupa, M. Queffelec (1997) *UV and VUV optical excitations in wide band gap materials doped with rare earth ions: 4f-5d transitions* J. Alloys & Compd. 250(1-2):287-292

160. E. Loh (1967) *Ultraviolet Absorption Spectra of Ce^{3+} in Alkaline-Earth Fluorides* Phys. Rev. 154(2):270-276

161. J.A. Duffy (1993) *A Review of Optical Basicity and Its Applications to Oxidic Systems* Geochim. Cosmochim. Ac. 57(16):3961-3970

162. J.A. Duffy (2011) *Optical basicity of fluorides and mixed oxide-fluoride glasses and melts* Phys. Chem. Glasses-B 52(3):107-114

163. J.A. Duffy (1986) *The Refractivity and Optical Basicity of Glass* J. Non-Cryst. Solids 86(1-2):149-160

164. R. Reisfeld, J. Hormodal, B. Barnett (1972) *Ce^{3+} as a Probe of Crystal-Field and Nature of Impurity-Ligand Bond in Borate and Phosphate Glasses* Chem. Phys. L. 17(2):248-251

165. J.S. Stroud (1961) *Photoionization of Ce^{3+} in Glass* J. Chem. Phys. 35(3), 844-850

166. N.V. Nikonorov, A.I. Sidorov, V.A. Tekhomskii (2010) *Silver nanoparticles in oxide glasses: technologies and properties*, In: Nanotechnology and Nanomaterials,

167. L.A. Siiman, J. Lumeau, L.B. Glebov (2008) *Nonlinear photosensitivity of photo-thermo-refractive glass by high intensity laser irradiation* J. Non-Cryst. Solids 354(34):4070-4074

168. L.A. Siiman, J. Lumeau, L.B. Glebov (2009) *Nonlinear photoionization and laser-induced damage in silicate glasses by infrared ultrashort laser pulses* Appl. Phys. B-Lasers O. 96(1):127-134

169. F. Kompan, G. Venus, L. Glebova et al. (2016) *Photo-thermo-refractive glass with sensitivity to visible and near IR radiation* Opt. Mater. Express 6(12):3881-3891

170. U. Kreibig (1976) *Small Silver Particles in Photosensitive Glass - Their Nucleation and Growth* Appl. Phys. 10(3):255-264

171. W.A. Weyl, *Coloured Glasses*. 1951, Sheffield: The Society of Glass Technology.

172. C.F. Bohren, D.R.Huffman 1983 *Absorption and scattering of light by small particles* Wiley: New York.

173. U. Kreibig *Optical Properties of Metal Clusters*. 1995, Berlin, Heidelberg: Springer

174. J. Lumeau, L. Glebova, L.B. Glebov (2014) *Absorption and scattering in photo-thermo-refractive glass induced by UV-exposure and thermal development* Opt. Mater. 36(3):621-627

175. A.I. Ignatiev, A.V. Nashchekin, V.M. Nevedomskii et al. (2011) *Formation of Silver Nanoparticles in Photothermorefractive Glasses during Electron Irradiation* Tech. Phys+ 56(5):662-667

176. A.I. Ignatiev, N.V. Nikonorov, A.I. Sidorov et al. (2013) *Influence of UV irradiation and heat treatment on the luminescence of molecular silver clusters in photo-thermo-refractive glasses* Opt. Spectrosc+ 114(5):769-774

177. J. Lumeau, L. Glebova, L.B. Glebov (2008) *Influence of UV-exposure on the crystallization and optical properties of photo-thermo-refractive glass* J. Non-Cryst. Solids, 354(2-9):425-430

178. A.P. Nacharov, N.V. Nikonorov, A.I. Sidorov et al. (2008) *Influence of ultraviolet irradiation and heat treatment on the morphology of silver nanoparticles in photothermorefractive glasses* Glass Phys. Chem. 34(6):693-699

179. U. Kreibig, C. Vonfrags (1969) *Limitation of Electron Mean Free Path in Small Silver Particles* Z. Phys. 224(4), 307-323

180. N.V. Nikonorov, A.I. Sidorov, V.A. Tsekhomskii et al. (2009) *Effect of a dielectric shell of a silver nanoparticle on the spectral position of the plasmon resonance of the nanoparticle in photochromic glass* Opt. Spectrosc. 107(5):705-707

181. V.A. Aseev, P.A. Burdaev, E.V. Kolobkova et al. (2012) *Fluorophosphate glasses activated by rare-earth ions and AgBr* Glass Phys. Chem. 38(4):366-372

182. J. Lumeau, L. Glebova, L.B. Glebov (2008) *Evolution of Absorption Spectra in the process of Nucleation in Phot-Thermo-Refractive Glass* Adv. Mater. Res. 39-40:395-398

183. I. Dyamant, A.S. Abyzov, V.M. Fokin et al. (2013) *Crystal nucleation and growth kinetics of NaF in photo-thermo-refractive glass* J. Non-Cryst. Solids 378:115-120

184. G.P. Souza, V.M. Fokin, C.F. Rodrigues et al. (2011) *Liquid-Liquid Phase Separation in Photo-Thermo-Refractive Glass* J. Am. Ceram. Soc. 94(1):86-91

185. J. Lumeau, K. Chamma, L. Glebova et al. (2014) *X-ray diffraction study of NaF nano-crystals in photo-thermo-refractive glass* J. Non-Cryst. Solids 405:188-195

186. J. Lumeau, L. Glebova, G.P. Souza et al. (2008) *Effect of cooling on the optical properties and crystallization of UV-exposed photo-thermo-refractive glass* J Non-Cryst. Solids 354(42-44):4730-4736

187. J. Lumeau, L. Glebova, V. Golubkov et al. (2009) *Origin of crystallization-induced refractive index changes in photo-thermo-refractive glass* Opt. Mater. 32(1):139-146

188. O.M. Efimov, L.B. Glebov, H.P. Andre (2002) *Measurement of the induced refractive index in a photothermorefractive glass by a liquid-cell shearing interferometer* Appl. Opt. 41(10):1864-1871

189. R.G. Hill, A. Stamboulis, R.V. Law (2006) *Characterisation of fluorine containing glasses by F-19, Al-27, Si-29 and P-31 MAS-NMR spectroscopy* J. Dent. 34(8):525-532

190. C. Bocker, A. herrmann, P. Loch et al. (2015) *The nano-crystallization and fluorescence of terbium doped* $Na_2O/K_2O/CaO/CaF_2/Al_2O_3/SiO_2$ *glasses* J. Mater. Chem. C 3(10):2274-2281

191. A. Stamboulis, R.G. Hill, R.V. Law (2004) *Characterization of the structure of calcium alumino-silicate and calcium fluoro-alumino-silicate glasses by magic angle spinning nuclear magnetic resonance (MAS-NMR)* J. Non-Cryst. Solids 333(1):101-107

192. J.E. Shelby 2005 *Introduction to Glass Science and Technology* Cambridge, UK: The Royal Society of Chemistry

193. T. Munhoz, N. Karpukhina, R.G. Hill et al. (2010) *Setting of commercial glass ionomer cement Fuji IX by Al-27 and F-19 MAS-NMR* J. Dent. 38(4):325-330

194. R.G. Hill, C. Goat, D. Wood (1992) *Thermal-Analysis of a* SiO_2-Al_2O_3-*CaO*-CaF_2 *Glass* J. Am. Ceram. Soc. 75(4):778-785

195. E.M. Sgibnev, A.I. Ignatiev, N.V. Nikonorov et al. 82013) *Effects of silver ion exchange and subsequent treatments on the UV-VIS spectra of silicate glasses. I. Undoped,* CeO_2-*doped, and* (CeO_2 + Sb_2O_3)-*codoped photo-thermo-refractive matrix glasses* J. Non-Cryst. Solids 378:213-226

196. V. Dimitrov, T. Komatsu (2002) *Classification of simple oxides: A polarizability approach* J. Solid State Chem. 163(1):100-112

197. Y.M. Sgibnev, N.V. Nikonorov, A.I. Ignatiev (2017) *High efficient luminescence of silver clusters in ion-exchanged antimony-doped photo-thermo-refractive glasses: Influence of antimony content and heat treatment parameters* J. Lumin. 188:172-179

198. U. Kreibig, P. Zacharia. (1970) *Surface Plasma Resonances in Small Spherical Silver and Gold Particles* Z. Phys. 231(2):128-143

199. K.L. Kelly, E. Coronado, L.L. Zhao et al. (2003) *The optical properties of metal nanoparticles: The influence of size, shape, and dielectric environment.* J. Phys. Chem. B 107(3):668-677

200. S.H. Wemple (1973) *Refractive-Index Behavior of Amorphous Semiconductors and Glasses* Phys. Rev. B **7**(8):3767-3777

201. L. Granasy, T. Pusztai, J.A. Warren et al. (2003) *Growth of 'dizzy dendrites' in a random field of foreign particles* Nat. Mater. 2(2):92-96

202. L. Granasy, T. Pusztai, T. Borzsonyi et al. (2004) *A general mechanism of polycrystalline growth* Nat. Mater. 3(9):645-650

203. A.G. Shtukenberg, Y.O. Punin, E. Gunnet al. (2012) *Spherulites* Chem. Rev. 112(3):1805-1838

204. W. Wisniewski, M. Patschger, C. Rüssel (2013) *Viscous Fingering and Dendritic Growth of Surface Crystallized* $Sr_2TiSi_2O_8$ *Fresnoite* Sci. Rep. UK 3: 3558

9. Poster

M. Stoica, C. Patzig, C. Bocker, M. Kracker, W. Wisniewski, A. Herrmann, J. Hein, Thomas Höche, Christian Rüssel **2017** *„Structural Evolution of CaF_2 Nano Particles During the Photoinduced Crystallization of a $Na_2O/K_2O/CaO/CaF_2/Al_2O_3/ZnO/SiO_2$ Glass“* 91. Glastechnische Tagung der DGG, Weimar

M. Stoica, C. Rüssel **2016** *„Einfluss von UV-Belichtung und Temperaturbehandlung in einem CaF_2 PTR Glas“* Thüringer Werkstofftag, Technische Universität Ilmenau

M. Stoica, C. Rüssel, **2015** *„Nanostruktur und Brechzahländerung in einem CaF_2 PTR Glas“* Glashüttentag der JDGG, TU Bergakademie Freiberg

M. Stoica, G. N. B. M. de Macedo, C. Rüssel **2015** *„Photo-Thermo-Refractive Glass from a CaF_2 Oxyfluoride System“* Advanced School on Glasses and Glass-Ceramics, Center for Research, Technology and Education in Vitreous Materials (CerTEV), Federal University of São Carlos, São Carlos (Brasilien)

M. Stoica, C. Rüssel, **2015** *„Nanostruktur und Brechzahländerung in einem CaF_2 PTR Glas“* Thüringer Werkstofftag, Bauhaus Universität Weimar.

M. Stoica, G. N. B. M. de Macedo, C. Rüssel **2014** *„Photo-induced-crystallization of CaF_2 from a $Na_2O/K_2O/CaO/CaF_2/Al_2O_3/SiO_2$ glass“* Brazilian Symposium on Glass and Related Materials, Center for Research, Technology and Education in Vitreous Materials (CeRTEV), São Carlos (Brasilien).

M. Stoica, C. Rüssel **2014** *„Photo-Thermo-Refractive Glass basierend auf einem CaF_2 Glassystem“* Thüringer Werkstofftag, Otto-Schott-Institut für Materialforschung, Friedrich-Schiller-Universität Jena

10. Presentations

M. Stoica, C. Patzig, C. Bocker, M. Kracker, W. Wisniewski, A. Herrmann, J. Hein, Thomas Höche, Christian Rüssel **2017** *„Photoinduced Crystallization of CaF_2 from a $Na_2O/K_2O/CaO/CaF_2/Al_2O_3/ZnO/SiO_2$ Glass"* 91. Glastechnische Tagung der DGG, Weimar

M. Stoica, C. Patzig, C. Bocker, M. Kracker, W. Wisniewski, A. Herrmann, J. Hein, Thomas Höche, Christian Rüssel **2017** *„Microstructure in a CaF_2* PTR glass*"* Otto-Schott-Institut für Materialforschung, LS Glaschemie I, Friedrich-Schiller-Universität Universität Jena

M. Stoica, A. Herrmann, J. Hein, C. Rüssel **2016** *„Effect of UV-exposure and heat treatment on the optical properties in a CaF_2 photo-thermal-refractive glass"* Centenary Conference of the SGT & ESG, Sheffield (UK)

M. Stoica, C. Rüssel **2016** *„Photoinduzierte Kristallisation in einem Oxyfluoridglassystem zur Herstellung von Volumen-Bragg-Gittern"* Otto-Schott-Institut für Materialforschung, LS Glaschemie I, Friedrich-Schiller-Universität Jena

M. Stoica, C. Rüssel **2015** *„Photo-induced-crystallization of CaF_2 from a $Na_2O/K_2O/CaO/$ $CaF_2/Al_2O_3/SiO_2$ glass- Photo-thermo-refractive glass"* Conference of the Society of Glass Technology, "Glass Reflections- Glass in the Year of Light", Cambridge (UK)

M. Stoica, C. Rüssel **2015** *„Effekt von Belichtung und Temperatur in einem CaF_2 PTR Glas"* Otto-Schott-Institut für Materialforschung, LS Glaschemie I, Friedrich-Schiller-Universität Universität Jena

M. Stoica, G.N.B.M. de Macedo, C Rüssel **2015** *„Photo-Thermo-Refractive Glass from a CaF_2 Oxyfluoride System"* Advanced School on Glasses and Glass-Ceramics, Center for Research, Technology and Education in Vitreous Materials (CerTEV), Federal University of São Carlos, São Carlos (Brasilien)

M. Stoica, C. Rüssel **2014** *„Ein neues PTR Glas durch Kristallisation von CaF_2"* Fachausschuss I (Physik und Chemie des Glases) der HVG-DGG, Mainz

M. Stoica, C. Rüssel **2014** *„Photoinduzierte Kristallisation von CaF_2 aus einem $Na_2O/$ $K_2O/$ $CaO/$ $CaF_2/$ $Al_2O_3/$ SiO_2 Glassystem"* Otto-Schott-Institut für Materialforschung, LS Glaschemie I, Freidrich-Schiller-Universität Jena

M. Stoica, C. Rüssel **2013** *„PTR Gläser basierend auf NaF und CaF_2 Glassystemen-Photoinduzierte Kristallisation"* Otto-Schott-Institut für Materialforschung, LS Glaschemie I, Friedrich-Schiller-Universität Jena

M. Stoica, C. Rüssel **2012** *„Herstellung und Strukturierung von NaF und CaF_2 PTR Gläsern"* Otto-Schott-Institut für Materialforschung, LS Glaschemie I, Friedrich-Schiller-Universität Jena

11. Danksagung

Nach vielen Jahren intensiver Arbeit an dieser Dissertation ist es nun auch an der Zeit, mich bei denjenigen gebührend zu bedanken, die mich auf diesem herausfordernden, aber auch ungemein lohnenden Weg zu dieser Arbeit begleitet haben.

An erster Stelle möchte ich mich ganz besonders bei meinem Doktorvater Prof. Dr. Christian Rüssel bedanken. Nennenswert sind sein wertvoller akademischer Rat, die stetige Betreuung und die Unterstützung dabei, meine Arbeit auf zahlreichen nationalen und internationalen Workshops und Konferenzen zu präsentieren. Zudem bin ich Frau Prof. Dr. Dörte Stachel zu großem Dank verpflichtet für den wissenschaftlichen Austausch und die Übernahme des Zweitgutachtens.

Ich bedanke mich bei meinen Co-autoren für die Hilfe in allen technischen Belangen und die vielen hilfreichen Diskussionen, u.a. bei Dr. Christian Bocker für die zahlreichen elektronenmikroskopischen Analysen, Dr. Andreas Herrmann für die Lumineszenz-spektroskopie, Dr. Michael Kracker für die Computersimulationen, Dr. Wolfgang Wisniewski für die EBSD Analysen, Dr. Christian Patzig und Prof. Dr. Thomas Höche für die aufwendigen elektronenmikroskopischen Untersuchungen am Fraunhofer IMWS in Halle, Dr. Joachim Hein und Diethard Klöpfel vom IOQ Jena für die Hilfe bei der Realisierung der Laserexperimente, Guilherme Nunes Braga Mauricio de Macedo und Martin Brehl für die hervorragende praktische Laborarbeit..

Aufrichtiger Dank gebührt Gabriele Möller für die sehr aufwendigen Probenpräparationen. Ich danke Thomas Kittel für die Diskussionen und gegebenen Denkanstöße, die Hilfestellung in Ofen, Steuer- und Temperaturmesstechnik, sowie für die zahlreichen Messungen. Corinna Seelheim danke ich für die andauernde Unterstüzung bei der Projektverwaltung. Dank geht auch an Angelika Hacker, Steffi Ebbinghaus, Dietmar Güttler, Lutz Preißer, Rainer Weiß und Christian Zeidler für die technische Unterstützung.

Ich danke dem Bundesministerium für Bildung und Forschung (BMBF) für die finanzielle Unterstützung in den letzten Jahren im Rahmen des Wachstumskerns BrightLas (03WKCF3E). In diesem Zusammenhang gilt auch Dank Ingolf Baumann und Torsten Thiel der AOS fiber GmbH Dresden für die Strukturierungsexperimente und anregenden Diskussionen.

Ich danke herzlich allen Freunden, Kollegen und Kolleginen des Otto-Schott-Instituts für die angenehme Zusammenarbeit, besonders Dr. Antje Gawronski, Dr. Mirko Tiegel und Ulrike Veit für die Unterstützung, die erquickenden Mittagspausen, die wunderbare Zeit im Labor und die Freundschaft.

Ich danke meiner Schwester für die moralische Unterstützung. Danke von Herzen an meine Eltern für die Unterstüzung in jeglicher Hinsicht, sowie für die Zuversicht, die sie mir auf meinen Lebensweg mitgegeben haben.

Den liebevollsten Dank verdienen die zwei wichtigsten Menschen in meinem Leben, meine Kinder Louis und Nina. Ich bin mit euch gewachsen.

12. Curriculum Vitae

Persönliche Angaben

geboren am 21.12.1983 in Naumburg/ Saale

ledig, 2 Kinder- (11 Jahre und 4 Jahre)

Beruflicher Werdegang

seit 11/2017	**Universitätsklinikum Jena, Lehrstuhl für Orthopädie, AG Experimentelle Rheumatologie**, Waldkliniken Eisenberg GmbH, 07607 Eisenberg *wissenschaftliche Angestellte*
01/2012- 06/2017	**Friedrich-Schiller-Universität Jena, Otto-Schott-Institut für Materialforschung**, Lehrstuhl Glaschemie I *wissenschaftliche Angestellte und Doktorandin*

Studium- und Schulbildung

01/2012-11/2017	**Friedrich-Schiller-Universität Jena, Otto-Schott-Institut für Materialforschung**, Lehrstuhl Glaschemie I *Promotion* **Thema:** „Photoinduced Crystallisation of CaF_2 from a $Na_2O/K_2O/CaO/CaF_2/Al_2O_3/SiO_2$ Glass”
8/2015	**Federal University of São Carlos** Center for Research, Technology and Education in Vitreous Materials CerTEV, São Carlos (Brasilien); Weiterbildung: “Advanced School on Glasses and Glass-Ceramics”
08/2013-02/2014	*in Elternzeit*
10/2003-6/2011	**Friedrich-Schiller-Universität Jena** Diplom Studiengang Chemie **Vertiefungsfächer:** Makromolekulare Chemie und Metallorganische Chemie/ Katalyse **Abschluss:** Diplom- Chemikerin (Dipl.- Chem.) **Diploma Thesis:** “Cobalt-mediated radical polymerization of alkyl acrylates“
02/2006-01/2007	*in Elternzeit*

8/1998-6/2003	**Landesschule Pforta,** Internatsgymnasium, Schulpforte/ Sachsen-Anhalt Spezialausrichtung Naturwissenschaften **Abschluss:** Abitur

Selbständigkeitserklärung

Ich erkläre, dass ich die vorliegende Arbeit selbständig und unter Verwendung der angegebenen Hilfsmittel, persönlichen Mitteilungen und Quellen angefertigt habe.

Ort, Datum

Unterschrift des Verfassers/der Verfasserin